

MASTER

Investigation of the Navier–Stokes–Cahn–Hilliard diffuse interface model for numerical simulations of unstable liquid filaments

van Sluijs, T.B.

Award date:
2021

[Link to publication](#)

Disclaimer

This document contains a student thesis (bachelor's or master's), as authored by a student at Eindhoven University of Technology. Student theses are made available in the TU/e repository upon obtaining the required degree. The grade received is not published on the document as presented in the repository. The required complexity or quality of research of student theses may vary by program, and the required minimum study period may vary in duration.

General rights

Copyright and moral rights for the publications made accessible in the public portal are retained by the authors and/or other copyright owners and it is a condition of accessing publications that users recognise and abide by the legal requirements associated with these rights.

- Users may download and print one copy of any publication from the public portal for the purpose of private study or research.
- You may not further distribute the material or use it for any profit-making activity or commercial gain

DEPARTMENT OF MECHANICAL ENGINEERING



Graduation Project

Investigation of the Navier–Stokes–Cahn–Hilliard diffuse interface model for numerical simulations of unstable liquid filaments

T.B. van Sluijs BSc.

Project coordinators:
prof.dr.ir. E.H. van Brummelen
T.H.B. Demont MSc.

Eindhoven, April 7, 2021

Contents

Page

List of symbols

Abbreviations

1	Introduction	1
2	Filament Breakup	3
2.1	Viscous filaments	3
2.2	Intermediate viscosity regime	4
2.3	Inviscid filaments	6
3	Diffuse-interface binary-fluid model	8
3.1	Governing equations	8
3.2	Boundary conditions and initial conditions	9
4	Numerical implementation	12
4.1	Axisymmetric model	12
4.2	Finite element method	12
4.3	Refinement procedure	12
4.4	ϵ -continuation	13
4.5	Temporal discretization	13
4.6	Solution procedure	13
4.7	Time step repetition	14
5	Filament contraction	15
5.1	The effect of mobility	15
5.1.1	High mobility	15
5.1.2	Phase mixing	17
5.1.3	General differences	19
5.2	Velocity field disturbance	21
5.2.1	Interface expansion	22
5.2.2	Mesh dependence	23
5.2.3	Medium dependence	24
5.2.4	ρ - η -continuation	27
5.2.5	Cahn–Hilliard time scale	29
5.3	Conclusion	31
6	Rayleigh–Plateau instability and rupturing	32
6.1	Rayleigh–Plateau instabilities	32
6.2	Numerical experiment	34
6.3	Conclusion	39
7	Conclusion and Recommendation	40
7.1	Conclusion	40
7.2	Recommendation	41
	References	43
A	Model derivation	45
A.1	Mass balance	45
A.2	Momentum balance	45

A.3	Solution space	47
A.4	Weak formulation	48
A.4.1	Mass balance weak formulation	48
A.4.2	Momentum balance weak formulation	48
A.4.3	Chemical potential weak formulation	49
A.4.4	Phase field weak formulation	50
A.5	Temporal discretization and model implementation	51
A.5.1	Temporal discretization mass balance	51
A.5.2	Temporal discretization momentum balance	51
A.5.3	Temporal discretization chemical potential	53
A.5.4	Temporal discretization phase field	53
B	Interface expansion simulations	54
B.1	Simulation domain	54
B.2	Curved interface	55
B.3	Coarse mesh interface	56

List of Symbols

Symbol	Definition	Unit	Abbreviation
δ	Initial perturbation amplitude	Meter	[m]
ϵ	Interface thickness	Meter	[m]
ϵ_0	Initial interface thickness	Meter	[m]
ϵ_{eq}	Equilibrium interface thickness	Meter	[m]
ϵ_L	Interface thickness for refinement level L	Meter	[m]
ζ	Capillary stress	Kilogram per meter second squared	[kg/ms ²]
η	Mixture viscosity	Kilogram per meter second	[kg/ms]
η_a	Ambient viscosity	Kilogram per meter second	[kg/ms]
η_l	Filament viscosity	Kilogram per meter second	[kg/ms]
θ	Azimuthal coordinate	Radian	[-]
κ	Dimensionless wave number	Dimensionless	[-]
κ_{max}	Dimensionless wave number for maximum perturbation growth	Dimensionless	[-]
Λ	Intrinsic liquid-ambient volume ratio	Dimensionless	[-]
λ	Wavelength	Meter	[m]
λ_{max}	Wavelength for maximum perturbation growth	Meter	[m]
μ	Chemical potential	Kilogram per squared meter second squared	[kg/m ² s ²]
ρ	Mixture density	Kilogram per cubic meter	[kg/m ³]
ρ_a	Ambient density	Kilogram per cubic meter	[kg/m ³]
ρ_l	Filament density	Kilogram per cubic meter	[kg/m ³]
σ	Surface tension	Kilogram per second squared	[kg/s ²]
τ_{CH}	Cahn–Hilliard timescale	Second	[s]
ϕ	Order parameter	Dimensionless	[-]
ϕ_a	Volume fraction ambient fluid	Dimensionless	[-]
ϕ_l	Volume fraction filament fluid	Dimensionless	[-]
τ	Viscous stress	Kilogram per meter second squared	[kg/ms ²]
τ_{cap}	Capillary timescale	Second	[s]
Ψ	Double well potential	Dimensionless	[-]
Ω	Domain		
ω	Perturbation growth rate	Per second	[s ⁻¹]
ω_{max}	Maximum perturbation growth rate	Per second	[s ⁻¹]

Symbol	Definition	Unit	Abbreviation
d	Distance	Meter	[m]
e_{red}	Percentual error reduction	Dimensionless	[-]
\mathbf{J}	Mass flux	Kilogram per squared meter second	[kg/m ² s]
K	Number of ϵ -continuation steps	Dimensionless	[-]
L	Refinement level	Dimensionless	[-]
L_0^*	Initial aspect ratio	Dimensionless	[-]
L_0	Initial filament length	Meter	[m]
L_c	Critical length	Meter	[m]
L_{max}	Maximum amount of refinements	Dimensionless	[-]
m	Mobility	Cubic meter second per kilogram	[m ³ s/kg]
m_a	Ambient molar density	Mole per cubic meter	[mol/m ³]
m_L	Mobility in refinement level L	Cubic meter second per kilogram	[m ³ s/kg]
m_1	Filament molar density	Mole per cubic meter	[mol/m ³]
Oh	Ohnesorge number	Dimensionless	[-]
p	Pressure	Kilogram per meter second squared	[kg/ms ²]
\tilde{R}	Perturbation amplitude	Meter	[m]
r	Radial coordinate	Meter	[m]
r_0	Initial filament radius	Meter	[m]
r_p	Radius of filament with perturbation	Meter	[m]
\mathbf{T}	Stress tensor	Kilogram per meter second squared	[kg/ms ²]
t	Time	Second	[s]
t_0	Initial time perturbation	Second	[s]
t_b	Breakup time	Second	[s]
t_{fin}	Finite time interval	Second	[s]
Δt_{max}	Time step size	Second	[s]
\mathbf{u}	Velocity	Meter per second	[m/s]
u_{cap}	Capillary contraction velocity	Meter per second	[m/s]
u_{jet}	Jet velocity	Meter per second	[m/s]
u_{peak}	Peak velocity	Meter per second	[m/s]
\mathbf{x}	Coordinate vector		
x	Cartesian coordinate	Meter	[m]
x_0	Initial interface position	Meter	[m]
z	Height coordinate	Meter	[m]

Abbreviations

Abbreviation	Explanation
a	Ambient
DOFs	Degrees of freedom
l	Filament
NSCH	Navier–Stokes–Cahn–Hilliard
Oh	Ohnesorge number

1 Introduction

Fluid filaments are important in various industrial applications, for example additive manufacturing, catalyst production or inkjet printing. Fluid filaments show different dynamic behavior depending on the circumstances and fluid properties. Filaments contract, break, and form droplets within a size distribution. For example, (Notz, Chen, & Basaran, 2001) observed sub-droplet formation, splitting, and re-coalescence at water dripping from a tube. Important parameters concerning these phenomena are fluid viscosity, surface tension between the filament and ambient fluid, and dimensions of the filament, specifically, the length to radius ratio (Driessen, Jeurissen, Wijshoff, Toschi, & Lohse, 2013; Notz & Basaran, 2004; Schulkes, 1996). The number of droplets and their size distribution influence the accuracy and quality of jetting and production processes. Therefore, it is important to be able to predict filament behavior during these processes (Driessen et al., 2013; Wijshoff, 2010).

Filaments can be classified into two categories. On the one hand, stable filaments contract under the influence of surface tension to a single droplet. This droplet will oscillate and viscous dissipation damps this vibration. On the other hand, unstable filaments break up into multiple droplets (Driessen et al., 2013; Notz et al., 2001). These droplets can have various sizes. It is possible that there are orders of magnitude difference between their radii. Small droplets can for example form a mist of small droplets or decrease print quality (Wijshoff, 2010).

The physical model of the filament dynamics contains a wide range of length and time scales. The largest length scale is the length of the original filament. The larger droplets have a radius in the same order as the filament length. Smaller droplets develop at breakup of the filament. These so called satellite droplets can be multiple orders of magnitude smaller than the large droplets (Notz & Basaran, 2004). Theoretically, the smallest length scale is the interface thickness between the filament and ambient fluid, however, in practice, this is not always true. One of the largest timescales corresponds to the contraction of the filament, while, the timescale of breakup is infinitely short. The droplets will oscillate after breakup or full contraction. The timescale of the oscillation depends on the size of the droplets. This results in a multi-scale fluid dynamics problem.

Droplet formation from liquid filaments has been studied experimentally for decades (Notz & Basaran, 2004). These experiments use expensive equipment, e.g. ultra-high-speed imaging systems, and are not able to capture the fluid dynamic details. The fluid dynamic problem represents a multi-scale problem, which makes it more difficult to observe all characteristics in an experiment. Modeling and simulations provide alternative means of scientific investigation for multi-scale phenomena complementary to experiments. Models enable easy prediction for different fluids, filament geometry, and initial circumstances.

Recently (Anthony, Kamat, Harris, & Basaran, 2019) used a sharp interface model to describe the filament contraction process. The model uses the slender jet approach and the filament breaks up if the minimum radius is smaller than a certain threshold. Using this approach, it was possible to determine the breakup dynamics over a wide range of initial geometries and Ohnesorge numbers, viz. the viscous force to inertia and capillary force ratio. In general, sharp interface models experience problems with topological changes such as breakup of fluid filaments. Proposed solutions are thresholds for breakup (Notz & Basaran, 2004; Anthony et al., 2019) and a tracking method for the interface (Teigen & Munkejord, 2009). The tracking operation determines where topological changes are needed and uses smoothing operations of physical quantities to ensure the accuracy of the solution. This is a complex procedure.

Diffuse interface models, as opposed to sharp interface models, are inherently capable of dealing with topological changes (Sun & Beckermann, 2007). (Van der Waals, 1893) already presented the idea of a continuous density in a transition layer between fluids. A diffuse interface model uses fluid concentrations in a so-called phase field. As a result, the physical quantities such as density and viscosity become a continuous field function defined by mixture theory and depend on the phase composition. The use of a diffuse Navier–Stokes–Cahn–Hilliard (NSCH) model results in the introduction of two model parameters. One of these

parameters, ϵ , represents the interface thickness, while the other, m , governs the rate of diffusive processes. The practical influence of these model parameters on dynamic processes is unknown. A systematic study of the effects of these model parameters is needed.

In this research, the diffuse interface NSCH model is applied to filaments to perform a systematic study and answer the following research question: what is the influence of the model parameters, namely the interface thickness parameter ϵ and the mobility parameter m , on the filament dynamics? For the interface thickness it is expected that the results for a small enough interface thickness will converge to a sharp interface limit. It is interesting to compare these results to a sharp interface model: do the results for decreasing interface thickness converge to a sharp interface limit? Do these results correspond to those of a sharp interface model? The interface in a diffuse interface model is a steep phase gradient, having a small length scale. The interface can interfere with small length scale phenomena, such as satellite droplets or the necking of the filament before breakup. In practice, the interface thickness is limited by the computational expense of the simulation. To determine the interference on these phenomena the following question must be answered: what is the influence of the diffuse interface on small length scale phenomena? The NSCH model is implemented numerically. The wide range of length and time scales is challenging for the spatial and temporal discretizations. We investigate whether the numerical implementation can simulate the filament dynamics in a robust manner. These research questions lie at the basis of this thesis.

In this work, the first step is the analysis of a simplified problem. The geometry of the simplified filament under consideration is assumed to be a perfect cylinder with hemispherical ends. This approximation is called the slender jet approach (Notz & Basaran, 2004; Driessen et al., 2013). The filaments are situated in a quiescent ambient fluid. Their contraction is driven by the minimization of free energy by the reduction of surface area. This simplified process is called free filament contraction.

The fluid dynamics problem is modeled by a NSCH model (Van Brummelen, Demont, & van Zwieten, 2020; Abels, Garcke, & Grün, 2012). The model is based on a volume averaged velocity field. The mass conservation applies to both the individual fluids as well as the mixture. The momentum conservation is valid for the mixture of fluids. The interaction between different fluids is modeled by a Cahn–Hilliard model. This model includes a chemical potential which drives the separation of immiscible fluids and a phase field to show the mixture composition. The Navier–Stokes flow model and Cahn–Hilliard fluid interaction model are coupled through the capillary stress. The combination of these models results in a multi-phase fluid dynamics model which includes interaction between the different phases. This NSCH model has been applied to the slender jet approximation to model filament contraction.

This report first elaborates on contracting filaments and the expected breakup modes in Section 2. This is needed to select a specific case for the numerical tests and offers data for comparison. The different modes and aspects of filament breakup are explained. Afterward, the diffuse interface NSCH model is explained in Section 3. The model explanation contains the governing equations, and the initial and boundary conditions. This model is applied to the filament contraction case and the results are analyzed to determine the influence of the model parameters. The numerical implementation of this model is elaborated in Section 4. This information is needed to be able to differ between numerical or model related effects. In Section 5 and Section 6, the results of the numerical experiments are presented. Finally, a conclusion is drawn with respect to the research questions and recommendations are given.

2 Filament Breakup

This section elaborates on different modes of breakup and their filament parameter regime. This information is used to select the filament characteristics for the numerical experiments and can also be used as a mean of comparison.

(Anthony et al., 2019) performed simulations on a wide range of filament characteristics and presents information on the mode of breakup, breakup time, and shape of the filament at breakup. This section summarizes results from (Anthony et al., 2019) as data for comparison and to select cases for the numerical experiments.

Liquid filaments contract under the influence of surface tension. The surface tension is a cohesive force which tends to minimize the surface area (Eggers & Villermaux, 2008). A minimal surface area is a low energy state and therefore energetically favored. However, it is this same force and energy minimization which drives the instability in these filaments.

Recently (Anthony et al., 2019) used a sharp interface model to describe the filament contraction process. The model describes a free filament, which contracts freely without influence of an ambient medium. In this model the filament domain splits when the fluid filament is sufficiently thin. This threshold is a reduction of the radius below a thousandth of the initial radius. This value represents the interface thickness and limits the resolution for details captured by this model. Using this approach it was possible to determine the breakup dynamics over a wide range of initial geometries and Ohnesorge number, viz. the viscous force to inertia and capillary force ratio. At high Oh, the major influence comes from viscous stress and forces. For a decreasing Oh the capillary forces become more and more influential.

(Anthony et al., 2019) determined that 3 different breakup regimes exist, indicated by different values of Oh. Within a certain regime, there can be different kind of breakup modes depending on the initial length of the filament. This study uses the initial aspect ratio as defined as:

$$L_0^* = \frac{L_0}{r_0}, \quad (2.1)$$

and Ohnesorge number:

$$\text{Oh} = \frac{\eta_l}{\sqrt{\rho_l r_0 \sigma}}, \quad (2.2)$$

where L_0 is half of the initial length, r_0 is the initial radius, η_l is the filament viscosity, ρ_l is the filament fluid density, and σ is the surface tension. Note that in the figures in this section the initial aspect ratio is L_0 instead of L_0^* due to naming convention.

2.1 Viscous filaments

For viscous filaments, $\text{Oh} > 0.1$, there is only one breakup mode. A contracting viscous filament can break up due to Rayleigh–Plateau-type instabilities (Anthony et al., 2019; Driessen et al., 2013). Rayleigh–Plateau instability is a periodic perturbation with an increasing amplitude which breaks the filament if the perturbation amplitude is around the same size as the filament radius (Driessen et al., 2013). The original perturbation in a theoretically perfect liquid jet can originate from contraction, can be applied artificially or can be caused by numerical errors (Schulkes, 1996).

This breakup only happens if the initial length is larger than the critical length. This critical length depends on Oh, as shown in Figure 2.1b. Higher Oh signifies higher viscous force in comparison to the capillary force. This reduces the growth rate of the Rayleigh–Plateau instabilities and increases the breakup time. An increased breakup time increases the critical length because the breakup time must be smaller than the contraction time.

The initial length of the filament also influences the breakup shape, see Figure 2.1a. Thereby, the initial length also determines the number of satellite drops resulting from the breakup, as shown in Figure 2.1c.

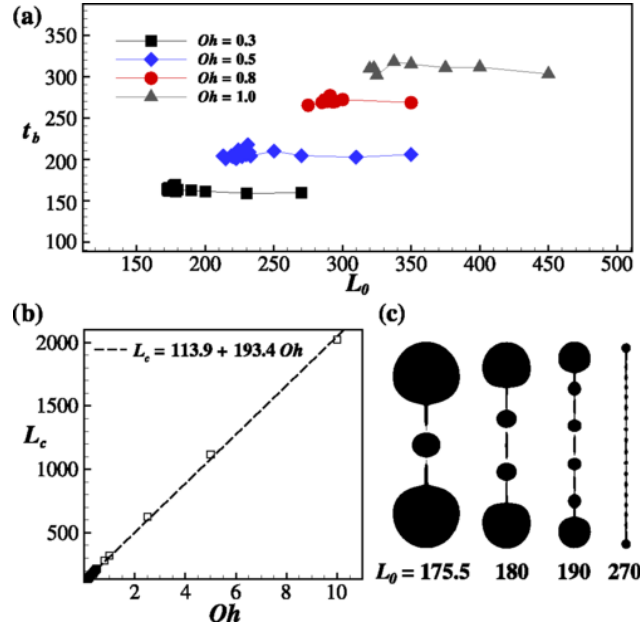


Figure 2.1: Breakup time, critical initial aspect ratio, and breakup shapes in the viscous regime. (a) Breakup time t_b as a function of the initial aspect ratio L_0 for several Oh . (b) Variation of the critical initial aspect ratio L_c [from (a)] with Ohnesorge number Oh . The data points are fit well by the indicated straight line, which shows the linear dependence of L_c on Oh . (c) Variation of breakup shapes at various values of L_0 that are well in excess of L_c when $Oh=0.3$. Reproduced from (Anthony et al., 2019).

2.2 Intermediate viscosity regime

Filaments in the intermediate viscosity regime, $0.002 < Oh < 0.1$, have multiple breakup modes. There is first and secondary capillary wave breakup and end pinching (Anthony et al., 2019). For short filaments there are several length intervals in which the breakup mode is first capillary wave breakup. Longer filaments also show secondary capillary wave breakup. However, this is just on a small interval. From a certain length, end pinching is the only breakup mode.

Figure 2.2b shows the breakup modes in these intervals. Capillary wave breakup only occurs on certain length intervals because it relies on a minimum of the filament radius due to the capillary wave in combination with the completed contraction of the filament (Anthony et al., 2019). The contraction time of the filament depends on the initial length. Only for certain length intervals the contraction time corresponds to a minimum in the radius due to the first or secondary capillary wave. Figure 2.3 shows the time evolution of the filament radii and indicates for which Oh break up occurs. The occurrence of higher order capillary wave minima is rare (Anthony et al., 2019). From a certain initial length end pinching occurs before the filament contraction is complete, hence, this is the only breakup mode for filaments longer than this length. Breakup for different modes occurs at different geometries, which influences the droplet size. This is shown in Figure 2.2a, which shows the geometry at breakup and spheres for filaments that contract to a sphere after oscillations.

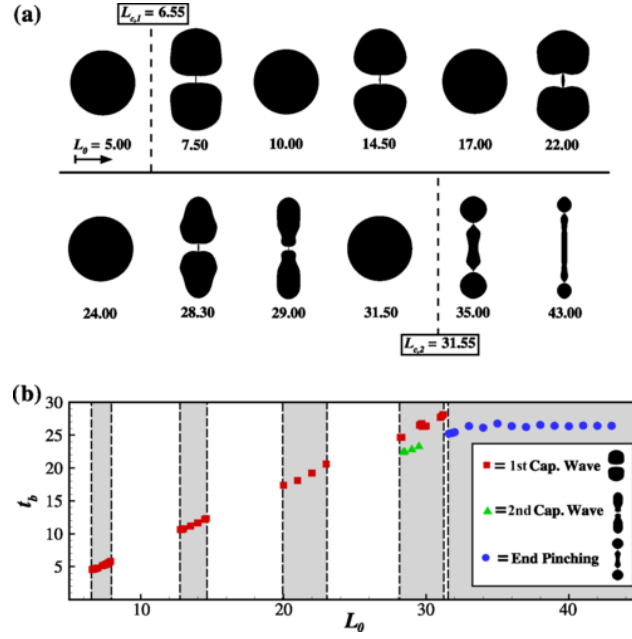


Figure 2.2: Breakup shapes and breakup times of filaments that undergo pinch-off or final shapes of filaments that do not break up when $Oh=0.03$. (a) Variation of shapes at breakup (not to scale) with L_0 showing a pattern of breakup and non-breakup. If there is no breakup for a particular value of L_0 , the spherical shape that corresponds to that value of L_0 indicates that the filament tends to a quiescent fluid sphere at large times. All filaments of initial aspect ratios $L_0 \geq L_{c,2}$ break up by end pinching. (b) Variation of breakup time t_b with L_0 . Filaments whose initial aspect ratios L_0 lie in ranges shaded in gray are those that undergo breakup at time t_b as indicated in the figure. Filaments whose initial aspect ratios L_0 lie in ranges shaded in white, however, do not break and tend to spheres at large times. When filament contraction leads to breakup, the type of breakup that results is identified by using different symbols and a typical shape is shown for each breakup mode in the legend. Squares and triangles are used to denote cases of first and second capillary wave breakup (where “Cap.” is the abbreviation for capillary), respectively, whereas circles are used to identify cases where breakup occurs by end pinching. Reproduced from (Anthony et al., 2019).

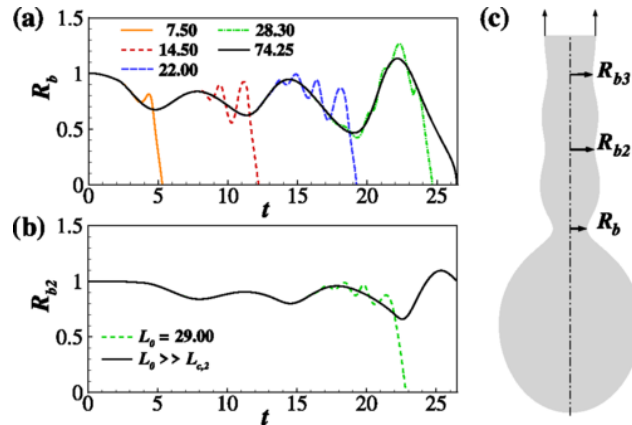


Figure 2.3: Time evolution of minima in the filament radius when $Oh=0.03$ and definition sketch showing different minima. (a) Evolution in time t of the radius R_b at the first minimum for filaments of $L_0=7.5, 14.5, 22,$ and 28.3 that undergo first capillary wave breakup. Also shown is the response of a long filament of $L_0=74.25$ that breaks by end pinching. (b) Time evolution of $R_{b,2}$, filament radius at the second minimum, for the single case of $L_0=29$ that undergoes second capillary wave breakup. Also shown is the response of a long filament of initial aspect ratio that is much larger than $L_{c,2}$. (c) Sketch that shows the first, second, and third minima $R_b, R_{b,2},$ and $R_{b,3}$, respectively. Reproduced from (Anthony et al., 2019).

2.3 Inviscid filaments

Inviscid filaments, $Oh < 0.002$, show the same dynamic behavior as the intermediate viscosity regime. The only difference is, that breakup also occurs after complex oscillation (Anthony et al., 2019), indicated by the white intervals in Figure 2.4b. This breakup mode occurs for filaments smaller than the minimum length for capillary wave breakup and also for longer filaments on the intervals where capillary wave breakup does not occur. Again the longer filaments only display end pinching due to shorter breakup time for this mode. The shape of the filaments at breakup is shown in Figure 2.4a.

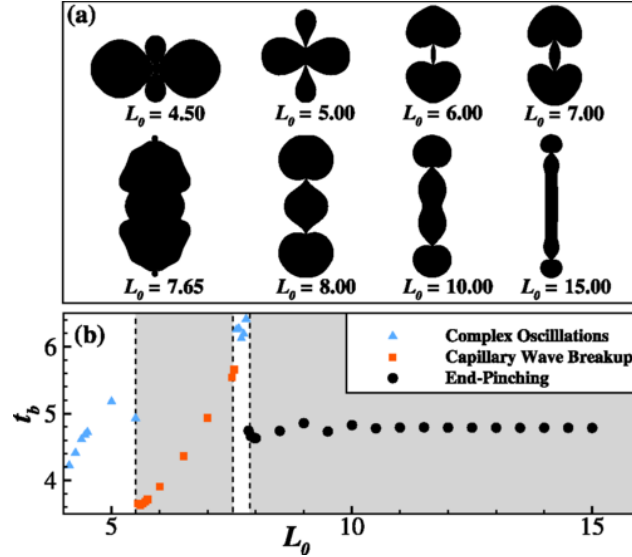


Figure 2.4: Breakup shapes and breakup times of filaments of $Oh=0.001$. (a) Variation of shapes at breakup (not to scale) with L_0 showing breakup by complex oscillations, capillary wave breakup, and end pinching. (b) Variation of breakup time t_b with L_0 . The different types of dynamics that fall into the various categories are identified by triangles, squares, and circles. The regions in gray indicate ones where breakup will occur before full contraction, whereas white regions indicate those where breakup will occur after full contraction and while the filaments are undergoing complex oscillations. Reproduced from (Anthony et al., 2019).

The breakup modes depend on the Ohnesorge number and the initial length. The results from (Anthony et al., 2019) are shown in Figure 2.5. This includes the different breakup modes and the different viscosity regimes. This figure shows a complete phase diagram with the different breakup modes depending on the Oh and the initial aspect ratio.

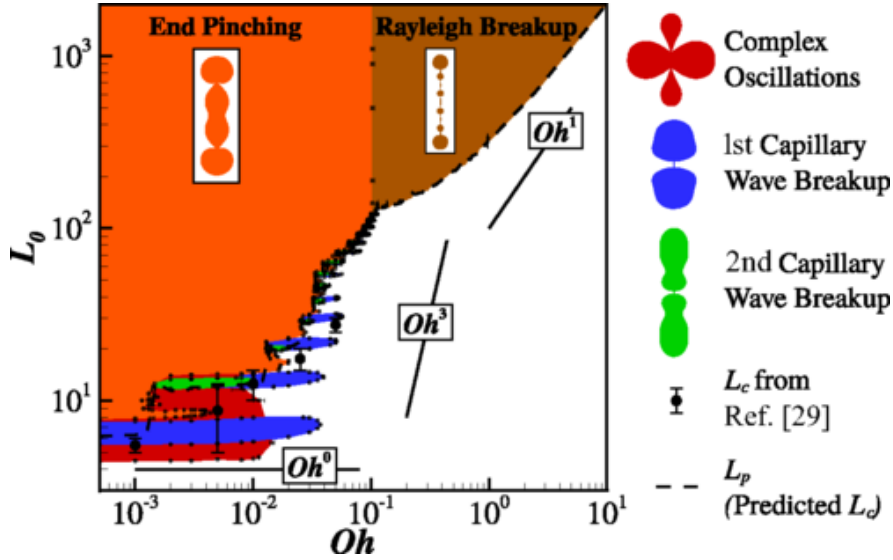


Figure 2.5: Phase diagram in the space of L_0 and Oh summarizing the fate of contracting Newtonian filaments that has been obtained after performing over 3000 simulations. Error bars, or uncertainties, on the boundaries between different breakup modes are shown in the figure but are typically too small to be visible. In the phase diagram, estimates of the critical initial aspect ratio obtained in the study of Notz and Basaran (Notz & Basaran, 2004) (Reference 29 from figure) are also shown as well as the simple scaling predictions obtained by comparing the contraction time to the relevant timescale of breakup in the three regimes (inviscid, intermediate, and viscous). Reproduced from (Anthony et al., 2019)

The sharp interface model with splitting mesh predicts the breakup modes for different Oh regimes. The transport phenomena within the filament are determined as well. However, the interfacial phenomena on the ambient fluid side are unknown due to the free surface sharp interface approach (Notz & Basaran, 2004). This is different using a diffuse interface model (Yang, Feng, Liu, & Shen, 2006). Diffuse interface models solve pressure, velocity, chemical potential, and phase fields inside and around the filament. Consequently, diffuse interface models capture the details of the interface dynamics, provided that the interface thickness is sufficiently small and the mobility is correct. Both of these models have the potential to simulate jetting processes, but first of all the simplified problem needs to be addressed. It starts by a slender jet approach, for which the model will be described in the test case description in Section 3.2.

3 Diffuse-interface binary-fluid model

This section presents the diffuse interface model which is used to model the filaments. The model definition introduces the model parameters which are investigated. This model corresponds to the diffuse-interface binary fluid model presented in (Van Brummelen et al., 2020) which is based on (Abels et al., 2012).

The contracting filament is described by a slender jet approach. These filaments are modeled by a diffuse interface NSCH model. The governing equations are described first, after which the boundary and initial conditions conforming the two filaments follow.

3.1 Governing equations

The binary fluid model describes an ambient fluid (a) and filament fluid (l) described by the volume fraction ϕ_a and ϕ_l respectively. These volume fractions form a partition of unity. The composition of the mixture is determined by an order parameter ϕ . This parameter uses the volume fractions to create the phase field, which is defined as:

$$\phi := \phi_l - \phi_a : (0, t_{fin}) \times \Omega \rightarrow [-1, 1]. \quad (3.1)$$

The phase field maps a combination of a time within the time interval $(0, t_{fin})$ and a point on the domain Ω on a range from -1 to 1. Using the partition of unity, the volume fractions can be expressed in the order parameter ϕ :

$$\phi_a = \frac{1 - \phi}{2}, \quad \phi_l = \frac{1 + \phi}{2}. \quad (3.2)$$

These volume fractions are used to express the mixture density as a function of the composition:

$$\rho = \rho(\phi) := \phi_l \rho_l + \phi_a \rho_a = \frac{1 + \phi}{2} \rho_l + \frac{1 - \phi}{2} \rho_a. \quad (3.3)$$

Here, $\mathbf{u} : (0, t_{fin}) \times \Omega \rightarrow \mathbb{R}^d$ is the volume averaged velocity. Using this mixture density and velocity field, the incompressible NSCH model of (Abels et al., 2012) writes:

$$\left. \begin{aligned} \partial_t(\rho \mathbf{u}) + \operatorname{div}(\rho \mathbf{u} \otimes \mathbf{u}) + \operatorname{div}(\mathbf{u} \otimes \mathbf{J}) + \operatorname{grad} p - \operatorname{div} \boldsymbol{\tau} - \operatorname{div} \boldsymbol{\zeta} &= 0, \\ \operatorname{div} \mathbf{u} &= 0, \\ \partial_t \phi + \operatorname{div}(\phi \mathbf{u} - m \operatorname{grad} \mu) &= 0, \\ \mu + \epsilon \sigma \Delta \phi - \frac{\sigma}{\epsilon} \Psi' &= 0. \end{aligned} \right\} \text{in } \Omega_t \quad (3.4)$$

The first two equations represent the momentum balance and mass balance, respectively. These follow from mixture theory, and its derivations are shown in Appendix A.2 and A.1, respectively.

In this model, \mathbf{J} is a relative mass flux defined as (Abels et al., 2012):

$$\mathbf{J} = m \frac{\rho_a - \rho_l}{2} \operatorname{grad} \mu. \quad (3.5)$$

This mass flux results from the volume averaged velocity field. The mixture energy density is defined as a standard double well potential:

$$\Psi(\phi) = \frac{1}{4} (\phi^2 - 1)^2. \quad (3.6)$$

The pure phases, $\phi = \pm 1$, are energetically most favorable.

In Equation (3.4), $\boldsymbol{\tau}$ represents the viscous stress, defined as

$$\boldsymbol{\tau} = \eta(\phi) (\operatorname{grad} \mathbf{u} + (\operatorname{grad} \mathbf{u})^T). \quad (3.7)$$

The viscosity, η , depends on the composition and is defined via the Arrhenius mixture-viscosity model (Van Brummelen et al., 2020):

$$\log \eta(\phi) = \frac{(1 + \phi)\Lambda \log \eta_l + (1 - \phi) \log \eta_a}{(1 + \phi)\Lambda + (1 - \phi)}, \quad (3.8)$$

where $\Lambda = \rho_l m_a / \rho_a m_l$ is the intrinsic liquid-ambient volume ratio, that is, the ratio of the molar volume of the liquid to the molar volume of the ambient fluid, and m_a and m_l the molar densities. ζ is the capillary component of the stress:

$$\zeta = -\epsilon \sigma \text{grad } \phi \otimes \text{grad } \phi + \mathbf{I} \left(\frac{\epsilon \sigma}{2} |\text{grad } \phi|^2 + \frac{\sigma}{\epsilon} \Psi - \mu \phi \right). \quad (3.9)$$

Solutions to the NSCH system, as shown in Equation (3.4), often include a value for the order parameter out of bounds of the range $[-1, 1]$ (Van Brummelen et al., 2020). Therefore the density interpolation is extended as follows:

$$\rho(\phi) = \begin{cases} \frac{1}{4}\rho_a, & \text{if } \phi \in (-\infty, -1 - 2\epsilon], \\ \frac{1}{4}\rho_a + \frac{1}{4}\rho_a \epsilon^{-2} (1 + 2\epsilon + \phi)^2, & \text{if } \phi \in (-1 - 2\epsilon, -1 - \epsilon), \\ \frac{1+\phi}{2}\rho_l + \frac{1-\phi}{2}\rho_a, & \text{if } \phi \in [-1 - \epsilon, 1 + \epsilon], \\ \rho_l + \frac{3}{4}\rho_a - \frac{1}{4}\rho_a \epsilon^{-2} (1 + 2\epsilon - \phi)^2, & \text{if } \phi \in (1 + \epsilon, 1 + 2\epsilon), \\ \rho_l + \frac{3}{4}\rho_a, & \text{if } \phi \in [1 + 2\epsilon, \infty). \end{cases} \quad (3.10)$$

This interpolation ensures positivity of the mixture density.

3.2 Boundary conditions and initial conditions

This section describes the auxiliary conditions for the considered test cases.

The slender jet fluid filament is represented by a cylinder with hemispherical caps. The filament is assumed to be axisymmetric and to contain a plane of symmetry orthogonal to the longitudinal axis at $z = 0$. Therefore, a single quadrant can represent the complete geometry.

The boundary conditions are shown in Figure 3.1. The ambient boundary is defined as a free-slip boundary without outflow. The free-slip boundary is defined as:

$$\mathbf{n} \times \mathbf{T}_n \times \mathbf{n} = \mathbf{0}, \quad (3.11)$$

where $\mathbf{T} = p\mathbf{I} - \boldsymbol{\tau} - \zeta$ is the stress tensor. The ambient boundary is assumed to be at a sufficiently large distance from the filament. Therefore, it is assumed that the phase field and chemical potential are fully developed, which means that the normal derivatives are zero. The symmetry plane is a symmetry boundary. Therefore, the normal velocity is zero and the normal derivatives of the phase field and chemical potential are zero too. The tangential flow must be unimpeded, which results in a free-slip boundary. Hence, the two boundaries have identical boundary conditions.

The governing equations, as shown in Equation (3.4), only depend on the pressure gradient. Neither the ambient boundary nor symmetry plane impose a Dirichlet condition on the pressure. Therefore, the pressure field is defined completely, except the complete field can be increased or decreased by a constant value. For the numerical experiments, a Lagrange multiplier for the pressure is implemented to ensure an average pressure equal to zero.

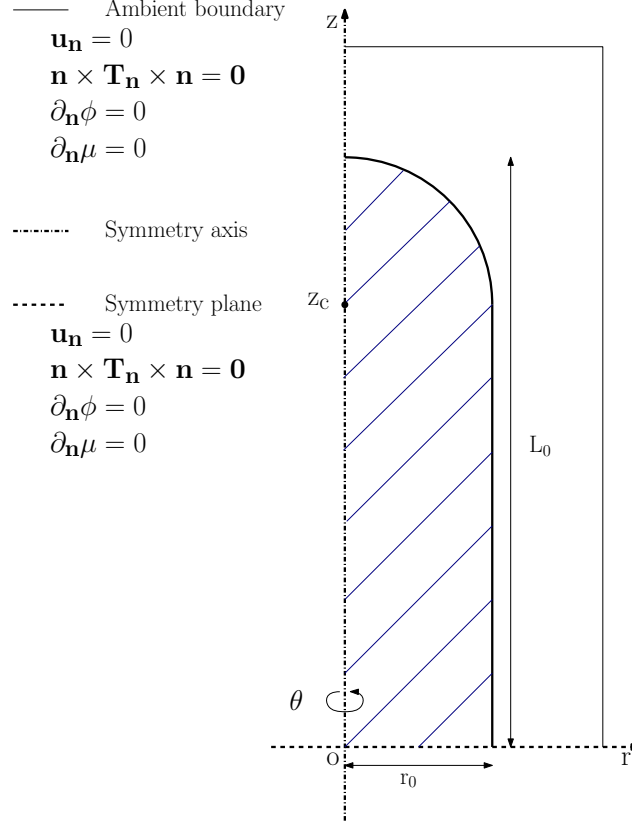


Figure 3.1: Single quadrant representation of fluid filament in the initial situation. The blue marked region is filament fluid and the interface position is indicated by the $\phi = 0$ contour line.

The filament is initially at rest in a quiescent ambient fluid. Therefore, the initial velocity is zero everywhere. The initial conditions are given by:

$$\begin{aligned}
 \mathbf{u}(\mathbf{x}, 0) &= \mathbf{0}, \\
 \phi(\mathbf{x}, 0) &= \tanh\left(\frac{r_0 - d(\mathbf{x})}{\sqrt{2}\epsilon}\right), \text{ and} \\
 \text{if } z < z_c: \quad d(\mathbf{x}) &= r; \quad \text{else: } d(\mathbf{x}) = \sqrt{r^2 + (z - z_c)^2},
 \end{aligned} \tag{3.12}$$

where $\mathbf{x} = (r, \theta, z)$ is the coordinate vector, containing the radial coordinate, azimuthal coordinate, and height coordinate.

The system of equations does not contain a time derivative for either the pressure or the chemical potential. Therefore, no initial conditions are needed for these quantities. The initial composition, determined by the order parameter, is more complicated. To create a cylinder with hemispherical caps, the distance to a line segment must be constant. The line segment is defined by the origin and $(0, z_c)$. This distance, d , is defined in Equation (3.12) with the geometry parameters r_0 and z_c as shown in Figure 3.1. The hyperbolic tangent creates a change from $\phi = 1$ near the line segment to $\phi = -1$ far in the ambient fluid. The drawn interface in Figure 3.1 is the $\phi = 0$ contour line corresponding to $d = r_0$. In both the initial condition and the solutions, the interface thickness is determined by ϵ . The interface thickness is governed by a trade-off between the interface energy and the mixture energy in the total free energy (Abels et al., 2012):

$$F = \int_{\Omega} \left(\frac{\sigma\epsilon}{2} |\nabla\phi|^2 + \frac{\sigma}{\epsilon} \Psi(\phi) \right) d\Omega. \tag{3.13}$$

The first term in the integral is the volumetric interface energy, which is a multiplication of the surface tension, the interface thickness and phase field gradient. This signifies that a steep phase gradient is energetically

unfavorable. The second term in the integral is the volumetric mixture energy. The double well potential, $\Psi(\phi)$, shows that a mixture of fluids is energetically unfavorable. For small ϵ , the phase field gradient can increase and the interface becomes smaller and steeper, which decreases the volume where there is a mixture of fluids and the mixture energy decreases. For large ϵ , a large phase gradient is more unfavorable in comparison to larger volume with phase mixing. The hyperbolic tangent, which is used as an initial condition, is an equilibrium solution in 1D.

The second case models an infinitely long axisymmetric filament with an initial perturbation as shown in Figure 3.2. The filament cannot break up due to end-pinching, capillary wave breakup, or breakup after complex oscillations because these modes of breakup require contracting filament ends. Thus, this filament can only succumb to Rayleigh–Plateau type instabilities. This filament is modeled using a symmetry plane for the upper and lower boundary, which creates the infinitely long filament. Modeling half of a wave of the initial perturbation is enough to represent the complete filament due to symmetry. The numerical experiment description in Section 6 explains which wavelength is used for the initial perturbation.

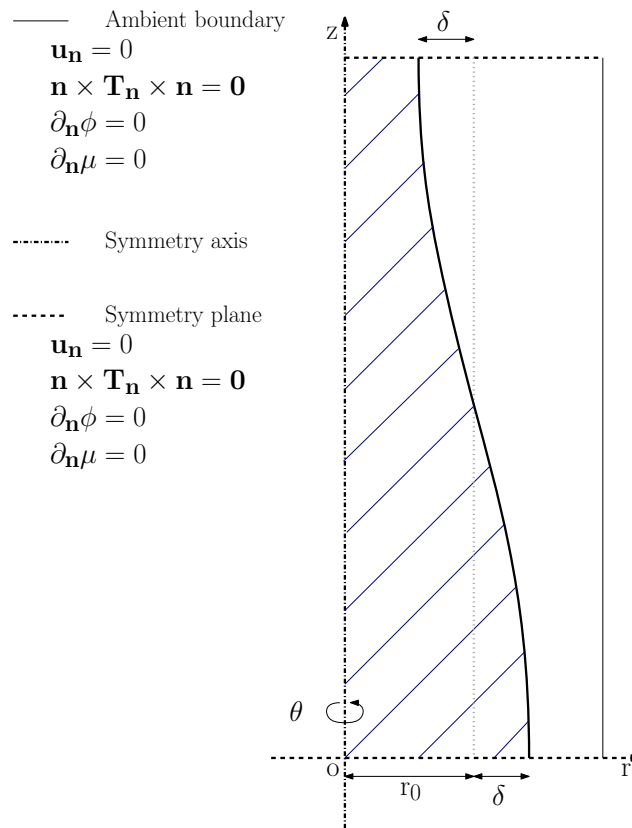


Figure 3.2: Axisymmetric representation of the infinite fluid filament with initial perturbation. The blue marked region is filament fluid and the interface position is indicated by the $\phi = 0$ contour line.

The filament is initially at rest. This results, together with the the initial perturbation, in the following initial conditions for the infinitely long filament:

$$\begin{aligned}
 \mathbf{u}(\mathbf{x}, 0) &= \mathbf{0}, \\
 \phi(\mathbf{x}, 0) &= \tanh\left(\frac{r_p(\mathbf{x}) - r}{\sqrt{2}\epsilon}\right), \text{ and} \\
 r_p(\mathbf{x}) &= r_0 + \delta \cos\left(\frac{2\pi z}{\lambda}\right).
 \end{aligned} \tag{3.14}$$

4 Numerical implementation

The NSCH model is implemented numerically using a finite element method. The numerical implementation is made in Nutils (Van Zwieten et al., 2020). This chapter gives a general description of the numerical model and implementation features. The numerical model is based on the model of (Van Brummelen et al., 2020). The differences are the axisymmetric implementation, the element types, the temporal discretization, the time step repetition feature, and the problem setting. This numerical model is used to perform numerical experiments. The numerical methods are needed to interpret the results of the numerical experiments and to assess the robustness of the numerical model.

4.1 Axisymmetric model

The axisymmetry cannot be implemented into the model directly. It starts by creating a domain in the form of a wedge using cylindrical coordinates (r, θ, z) . A cylinder is formed by taking the angle of the wedge equal to 2π . The mesh is cylindrical with only one element in the azimuthal direction. Thus, the elements are rings with a rectangular cross-section in the (r, z) -plane and the elements adjacent to the symmetry axis are disks. All basis functions are linear in the azimuthal direction. The sides of the wedge are subjected to a periodic boundary condition. This results in a single linear basis function in the rotational direction of which the beginning and end have the same value. Therefore, there is no angular dependency and the three dimensional domain is represented by a two dimensional axisymmetric domain.

4.2 Finite element method

The filament contraction problem, which is modeled by the NSCH model, is discretized using finite elements. For the simulations in Section 5.1, the basis functions in the (r, z) -plane for the velocity field, the phase field, and the chemical potential are second order and the basis function for the pressure is first order. All other simulations which were performed afterward have third order basis functions in the (r, z) -plane for the velocity field, the phase field, and the chemical potential and second order basis functions for the pressure. This is due to improvements in the model and the higher accuracy for third order elements. Therefore, the elements are rectangular Taylor–Hood elements, i.e. elements where the basis functions are of order n except for the basis functions corresponding to the pressure variable p , which are of order $n - 1$. All basis functions are linear in the azimuthal direction due to the axisymmetric implementation, as explained in the axisymmetric model description in Section 4.1.

The numerical implementation uses the theoretical model as described in Section 3. This includes the definitions of the phase field, viscosity, and density. The model uses the residual form of the weak formulation as given in Appendix A.4.1 to A.4.4. The boundary conditions are used in the residual form and also the initial condition corresponds to the theoretical model.

4.3 Refinement procedure

The numerical model uses a solve-estimate-mark-refine (SEMR) procedure for the spatial discretization to reduce the numerical error by refining elements (Van Brummelen et al., 2020). This adaptive refinement procedure is combined with the ϵ -continuation feature which is explained in Section 4.4. The refinement procedure enables simulation of filaments with thin interfaces without using small elements in the complete domain. The implemented SEMR procedure uses a solution on both a coarse and fine mesh to determine a relative error. The mesh is only refined in the (r, z) directions to preserve the axisymmetric implementation. The ϵ -continuation changes the interface thickness and mobility to assure robustness on all meshes. A combination of these procedures prevents the time step size from becoming restricted by the interface thickness in case of a thin interface.

The elements are ordered by contribution to the total error. For the total error it is possible to select error measures. The error is defined as a L^2 or H^1 norm of the error measures over the domain. The error measures for the filament contraction problem are the phase field, the velocity field, and the divergence of

the velocity field. The elements with the largest contribution to the total error are marked for refinement until a cumulative percentage of the total error is refined. The mesh for the next refinement step is generated by only refining the marked elements.

4.4 ϵ -continuation

ϵ -continuation is a numerical feature which effectively increases the interface thickness and the mobility parameter for a set number of refinement steps to increase the robustness of the solution on all meshes (Van Brummelen et al., 2020) and increase the admissible time step size. The parameter for the interface thickness, ϵ , and mobility, m , are increased on the coarser meshes.

The interface thickness is increased to reduce the error of the phase field projection to increase the time step size. The interface displacement is limited to the width of the interface. If the interface displacement is larger than the interface width, the error in phase field projection becomes large. This can result in an unstable or computationally expensive solution procedure. Thus, for a fixed velocity, either the time step size must be small or the interface must be thick. Therefore, the interface thickness is increased for the first solution in a new time step. Afterward, the interface thickness parameter is decreased to the chosen value in a given number of refinement steps. The mobility parameter is increased to enhance the interface expansion between different time steps. This process is studied in detail in the numerical study in Sections 5.2.1 through 5.2.5.

For a given refinement process with $L = 0, 1, 2, \dots, L_{\max}$ refinement levels and an initial interface thickness parameter $\epsilon_0 = 2^K \epsilon$, the interface thickness parameter is defined as $\epsilon_L = \epsilon \max(2^{K-L}, 1)$. In the initial $K - 1$ stages of the refinement procedure the interface thickness is halved in each stage. During the last $L_{\max} + 1 - K$ stages, the interface thickness is kept constant and equal to ϵ . The mobility parameter is also increased during the ϵ -continuation process. The mobility is $m_L = 10 \cdot 2^{3(K-L)} \cdot m$ during the ϵ -continuation and is equal to $m_L = m$ for the remaining refinement steps. An increased mobility enhances the interface profile equilibration for each ϵ_L .

4.5 Temporal discretization

The temporal discretization uses two different time integration schemes. A Crank-Nicolson semi-implicit time discretization scheme is used on the finest grid. This method is used for the solution on the finest mesh because this scheme yields a second order accuracy with respect to the time step size.

The coarser meshes use a less computational expensive discretization scheme. A fully implicit Backward-Euler time discretization scheme is used for solutions on the coarse meshes. This discretization scheme has a first order convergence rate for the time step size in contrast to the second order for the Crank-Nicolson scheme. The temporal discretization of the governing equations for both temporal discretization schemes are shown in Appendix A.5.

4.6 Solution procedure

We solve a FEM problem within each time step. Assuming that there are refinement steps, as explained in the refinement procedure in Section 4.3, we solve multiple problems within one time step.

The solution procedure starts with a projection of a previous solution or, for the first time step, the initial conditions. The solution procedure on the coarsest mesh uses a projection from the solution of the previous time step on the coarsest mesh. During the refinement steps the projection comes from the previous solution within the same time step.

Each solution is formed using a Newton-solver, which uses iterations to minimize the residuals from the residual formulations. Within each Newton iteration there is a linear solver which also uses iterations to reduce the residuals. The first refinement steps use a backward Euler implicit solution procedure to reduce

the computation time. A Crank–Nicolson method is used on the finest mesh, since this method has a second order accuracy for temporal discretization.

4.7 Time step repetition

The filament contraction phenomena contains multiple timescales. For example, the filament contraction time scale is larger than the time scale of breakup of the filament. The numerical model finds solutions discretized in time. The time step sizes between the solutions are limited to a maximum value, since the Newton-solver is unstable or prohibitively inefficient for large time steps and a large time step size leads to inaccurate results. The numerical model uses an adaptive time step size to adjust to the different timescales within the simulation. The time step size can be halved during the simulation if needed.

The solution can be deemed unsuccessful for multiple reasons. First of all, it is possible that the amount of iterations needed in the Newton-solver exceeds a chosen maximum. This can be the result of an inaccurate projection from a previous solution or a robustness problem. Another possibility is that the solver gets stuck in a local minimum, whereby the residual of the solver does not decrease anymore. It is important to note that this is all based on simulation robustness and not on solution accuracy.

Originally, the time step size was doubled after a successful time step with a time step size smaller than the maximum time step size. This resulted in an ongoing cycle of time step size division and doubling, resulting in an increased computation time. The time step repetition method prevents this to some degree.

The time step repetition is used when the time step size is halved. The number of time step repetitions must be a power of 2, and is regarded as an input for the model. The time step repetition ensures that all original solution time steps will be solved and it reduces computational time when the time steps need to be reduced.

The number of time step repetitions is the number of times a decreased time step size must be successfully used before the time step size is doubled. If the time step size is halved again before it is doubled, the process repeats up to the moment that the time step size, multiplied by the number of time step repetitions, is not equal to a multiple of the original time step size. The next halved time step will only be repeated 2 times and also counts as one of the larger time step. This will be explained with an example:

Consider the case where the number of time step repetitions is 4, and the original time step size is 1. Figure 4.1 shows a possible time line of solution time steps. This figure shows that the second regular solution is not found. The time step size is halved to $\frac{1}{2}$, and 3 of the 4 time step repetition solutions are found, after which the fourth solution is not deemed successful and the time step size is halved again to $\frac{1}{4}$. The first solution of this time step size is found, however, the second solution is not found and the time step size is halved to $\frac{1}{8}$. Since the time step size multiplied by the number of time step repetitions is smaller than the original time step size, $\frac{1}{8} \cdot 4 = \frac{1}{2} < 1$, the time steps of $\frac{1}{8}$ are only repeated 2 times and count as a time step of $\frac{1}{4}$. Afterward, the time step size is doubled to $\frac{1}{4}$ and the remaining 2 solutions for this time step size are found. The time step size is doubled to $\frac{1}{2}$ and the last solution for this time step size is found and the time step size is doubled to the original time step size.

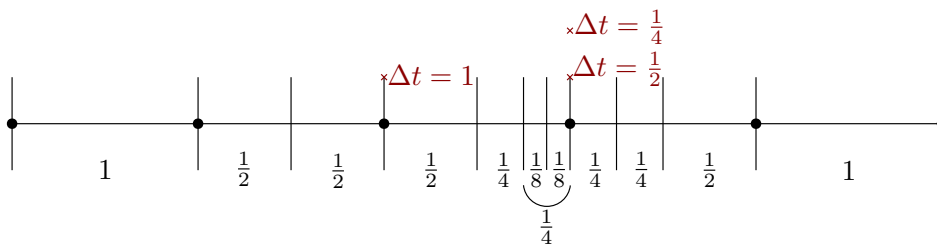


Figure 4.1: Simulation solution timestamp timeline. Black dots indicate the original timestamps and the red cross indicates a failed solution for a certain time step size.

5 Filament contraction

A specific case for the filament problem was selected using the specified unstable filaments in Section 2. The used Ohnesorge number is $Oh = \frac{\eta}{\sqrt{\rho_l r_0 \sigma}} = 7 \cdot 10^{-3}$ and the initial aspect ratio $L_0^* = \frac{L_0}{r_0} = 10$. This filament is in the intermediate viscosity regime. In this regime it is possible to test the capillary wave breakup, as well as end pinching. Although this filament is not in the inviscid regime, Figure 2.5 shows that the Oh is low enough for the filament to succumb to breakup after complex oscillation. The Oh in combination with the chosen initial aspect ratio predicts complex oscillation to be the breakup mode of this filament. This initial aspect ratio is still relatively small due to an increase in computational effort for increasing domain size. It is possible to test the other modes of breakup afterward.

At first the effect of the mobility parameter on the contraction behavior of the filament will be studied. A more detailed filament contraction case will be simulated afterward.

5.1 The effect of mobility

The mobility coefficient, m [$\text{m}^3\text{s}/\text{kg}$], is a parameter which governs the diffusive effects around the interface. For example, the mass flux relative to the velocity field, \mathbf{J} , Equation (3.5), is linearly dependent on the mobility. In the limit of a sharp interface, $\epsilon \rightarrow 0$, the mobility governs the diffusion through this interface (Abels et al., 2012). Therefore, the mobility is important for the model dynamics.

Multiple simulations are performed to investigate the effect of the mobility parameter on the filament contraction model. All simulation characteristics are constant except for the mobility. The mobility was increased by factors 10 from $m = 10^{-11} \text{ m}^3/\text{kg}$ with seven steps up to and including $m = 10^{-5} \text{ m}^3/\text{kg}$. The filament properties correspond to water and the ambient fluid approaches the characteristics of air. The viscosity of the ambient liquid is limited to $\eta_a = 10^{-4} \text{ kg/ms}$ by the robustness of this simulation. A lower viscosity can result in small time step sizes, increased amount of needed Newton-iterations to find a solution, and even non-physical flow phenomena in the solution. As described, the used Ohnesorge number is $Oh = 7 \cdot 10^{-3}$ and the initial aspect ratio is $L_0^* = 10$. The simulation characteristics are summarized in Table 5.1. No refinement steps are used, resulting in a uniform mesh for every time step. A uniform mesh only needs one solution per time step and therefore reduces the computational cost of the simulation. The relatively thick interface reduces the computation time further because the element size can be increased. As a consequence, the results must be interpreted with care since this interface thickness is artificially large.

Table 5.1: Simulation characteristics to study the effect of the mobility parameter

Mobility simulation characteristics			
General:			
$\Delta t_{\max} = 1.25 \text{ ms}$	$\epsilon = 5 \cdot 10^{-4} \text{ m}$	$\sigma = 7.28 \cdot 10^{-2} \text{ kg/s}^2$	$m = 10^{-11} - 10^{-5} \text{ m}^3/\text{kg}$
Domain:			
Radius = $9.81 \cdot 10^{-3} \text{ m}$	Radial elements: 48	Height = $2.35 \cdot 10^{-2} \text{ m}$	Axial elements: 144
Refinements = 0			
Filament:			
$\rho_l = 1000 \text{ kg/m}^3$	$\eta_l = 10^{-3} \text{ kg/ms}$	$L_0 = 1.962 \cdot 10^{-2} \text{ m}$	$r_0 = 1.962 \cdot 10^{-3} \text{ m}$
Ambient:			
$\rho_a = 1 \text{ kg/m}^3$	$\eta_a = 10^{-4} \text{ kg/ms}$		

5.1.1 High mobility

The filament contraction simulations with a relatively high mobility, i.e. $m = 10^{-6} \text{ m}^3/\text{kg}$ and $m = 10^{-5} \text{ m}^3/\text{kg}$, show particular flow phenomena. At the side of the filament a phenomenon occurs which looks similar to vortex shedding. However, taking a closer look at the side of the filament, Figures 5.1 and 5.2 show that the velocity field is more disturbed. The highest tested mobility also shows a discrepancy compared to all

other performed simulations. The ambient fluid follows the end of the contracting filament at first, however the ambient fluid deflects towards the center where it is discharged through a high velocity jet. This is shown in Figure 5.2.

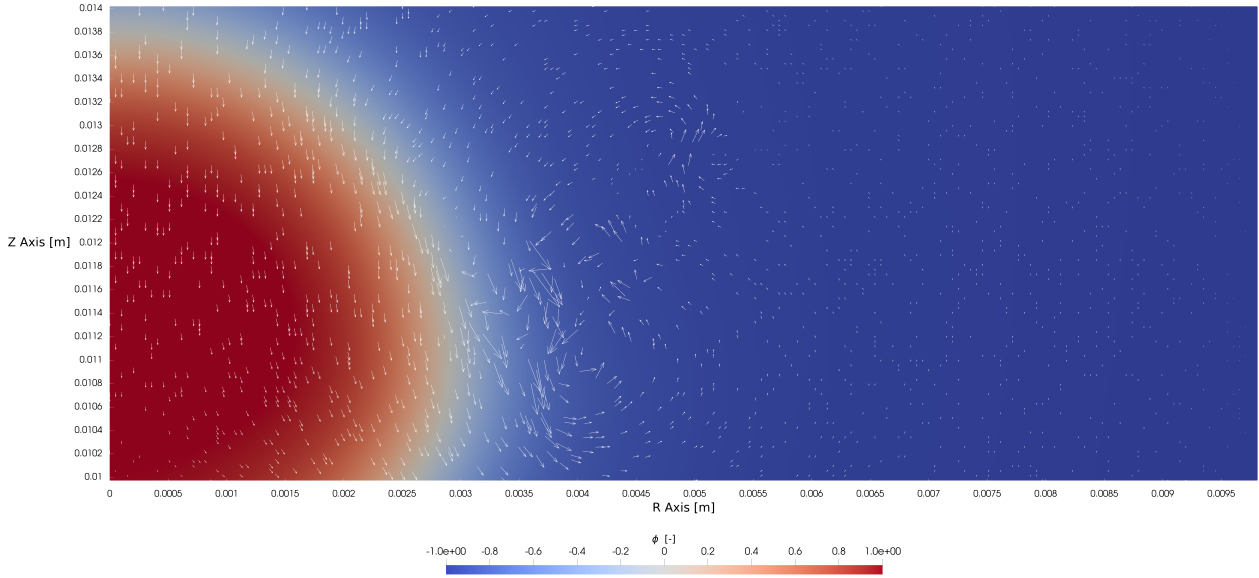


Figure 5.1: Disturbed velocity field at the side of the end bulb of the filament. The graph shows the phase field with a vector plot of the velocity field of the simulation with $m = 10^{-6} \text{ m}^3/\text{s}/\text{kg}$ at $t = 0.035 \text{ s}$.

The first high velocity phenomenon occurs at the side of the filament. A small pulse of fluid flows from the interface into the ambient fluid at high velocity. This creates a disturbed and chaotic flow field. The simulation with $m = 10^{-5} \text{ m}^3/\text{s}/\text{kg}$ shows velocity peaks at the side of the filament which are higher than for the simulation with $m = 10^{-6} \text{ m}^3/\text{s}/\text{kg}$. The velocity peaks are $u_{\text{Peak}} \approx 7 \text{ m/s}$ and $u_{\text{Peak}} \approx 2.3 \text{ m/s}$ respectively, while the filament contraction velocity is around $u_{\text{cap}} = \sqrt{\frac{\sigma}{\rho_1 r_0}} = \sqrt{\frac{7.28 \cdot 10^{-2} \text{ kg/s}^2}{10^3 \text{ kg/m}^3 \cdot 1.96 \cdot 10^{-3} \text{ m}}} = 0.19 \text{ m/s}$ (Driessen et al., 2013). Another difference is the time at which this phenomenon starts. For the highest tested mobility the phenomenon occurs around $t = 0.01 \text{ s}$, while it only starts at $t = 0.03 \text{ s}$ for $m = 10^{-6} \text{ m}^3/\text{s}/\text{kg}$.

The second high velocity phenomenon is located in the fluid trailing the filament. In general, the ambient fluid follows the tip of the contracting filament. At this point, another artifact occurs for the simulation with the highest tested mobility. The fluid that trails the filament end bulb deflects towards the center. This creates a radial inflow towards the symmetry axis and an axial outflow. It generates a high velocity jet of ambient fluid away from the filament. Figure 5.2 shows the jet which occurs at the top of the filament. The velocity in this jet reaches up to $u_{\text{jet}} \approx 25 \text{ m/s}$.

The vortex and jet artifacts are both high velocity phenomena in comparison to the filament contraction. The high velocities hinder the solution procedure. Due to the time step repetitions, the simulation with $m = 10^{-6} \text{ m}^3/\text{s}/\text{kg}$ can continue with a smaller time step size. However, the time step size for the simulation with $m = 10^{-5} \text{ m}^3/\text{s}/\text{kg}$ is decreased so far that the computational time for the complete filament contraction becomes prohibitive.

The time step size of the simulations decreased at the moment that these phenomena occurred. The simulation with $m = 10^{-6} \text{ m}^3/\text{s}/\text{kg}$ was also performed on a finer mesh. The magnitude of the high velocity phenomenon increased. Therefore, it is concluded that it is not probable that these phenomena are a discretization error. However, this was not researched thoroughly because the simulation with a lower mobility did not show these phenomena and this research would require computationally expensive simulations.

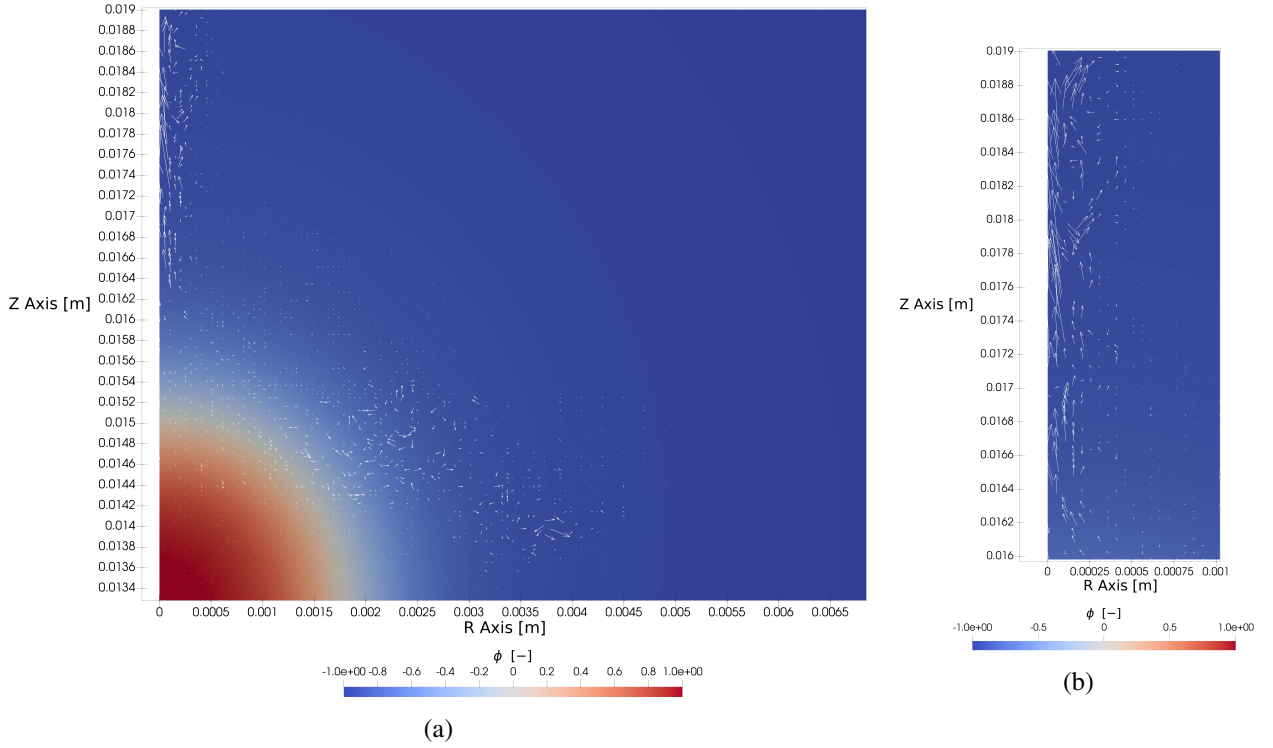


Figure 5.2: Jet and vortex phenomena at $t = 0.0104$ s for the simulation with $m = 10^{-5}$ m³/s/kg. The phase field is displayed with a vector plot of the velocity. (a) shows an overview of the phenomena on the side and top of the filament and (b) shows an enlargement of the top jet. The end bulb of the filament contracts downwards, which is nearly unobservable due to the vector scaling by the large velocity of the jet in the top left corner and the disturbed velocity field besides the filament.

The simulations show that the mobility is limited from above by this phenomena. It is concluded that these phenomena are not a result of discretization errors. High mobility values result in high velocity flow phenomena which are non-physical. This influences the macro-scale behavior of the flow field. Another consequence is a decreased robustness of the simulation, which results in drastic time step size decrease. The small time step size increases the computational time tremendously.

5.1.2 Phase mixing

Simulations with a relatively thick interface in comparison to the domain suffer from mixing. The filament and ambient fluid mix due to the inherent energy minimization of the NSCH model. The free energy is defined as (Abels et al., 2012):

$$F = \int_{\Omega} \left(\frac{\sigma\epsilon}{2} |\nabla\phi|^2 + \frac{\sigma}{\epsilon} \Psi(\phi) \right) d\Omega. \quad (5.1)$$

This free energy is an integration over the complete domain of the volumetric energy contributions. The first contribution comes from the phase field gradient, which signifies that sharp gradients in the phase field are energetically unfavorable. The second contribution to the volumetric free energy is associated with phase mixing. The double well potential, $\Psi(\phi)$, as defined in Equation (3.6), creates an energy penalty for mixing.

Large values for the interface thickness parameter ϵ correspond to a thick interface. Namely, the energy penalty belonging to phase mixing is small, while it is large for the phase gradient. From a certain interface thickness threshold, it is favorable to reduce the interface size of the filament by mixing filament fluid with ambient fluid.

This process is observed in simulations with differing mobility parameters. The interface thickness and surface tension are equal for these simulations. Therefore, the situation regarding the free energy is similar.

The observed mixing process is different between the simulations. The mixing speed increases with an increasing mobility. Figure 5.3 shows that the area in the ambient where mixing has occurred is larger for the highest tested mobility. The area where mixing has occurred is indicated by an increase in the phase field parameter shown by the light blue color, in contrast with the dark blue pure ambient phase. Another indicator is the filament size. The filament size is decreased drastically in the simulation with the largest mobility in comparison with the other simulations. Small length differences can be explained by a minor difference in contraction velocity, which increases slightly with increasing mobility. However, a difference in filament width in the middle of the filament near the symmetry plane indicates different mixing speed, as fluids in this part of the domain are stationary. Therefore, it can be concluded that the mixing speed is strongly dependent on the mobility. This is also shown by the Cahn–Hilliard timescale in Section 5.2.5.

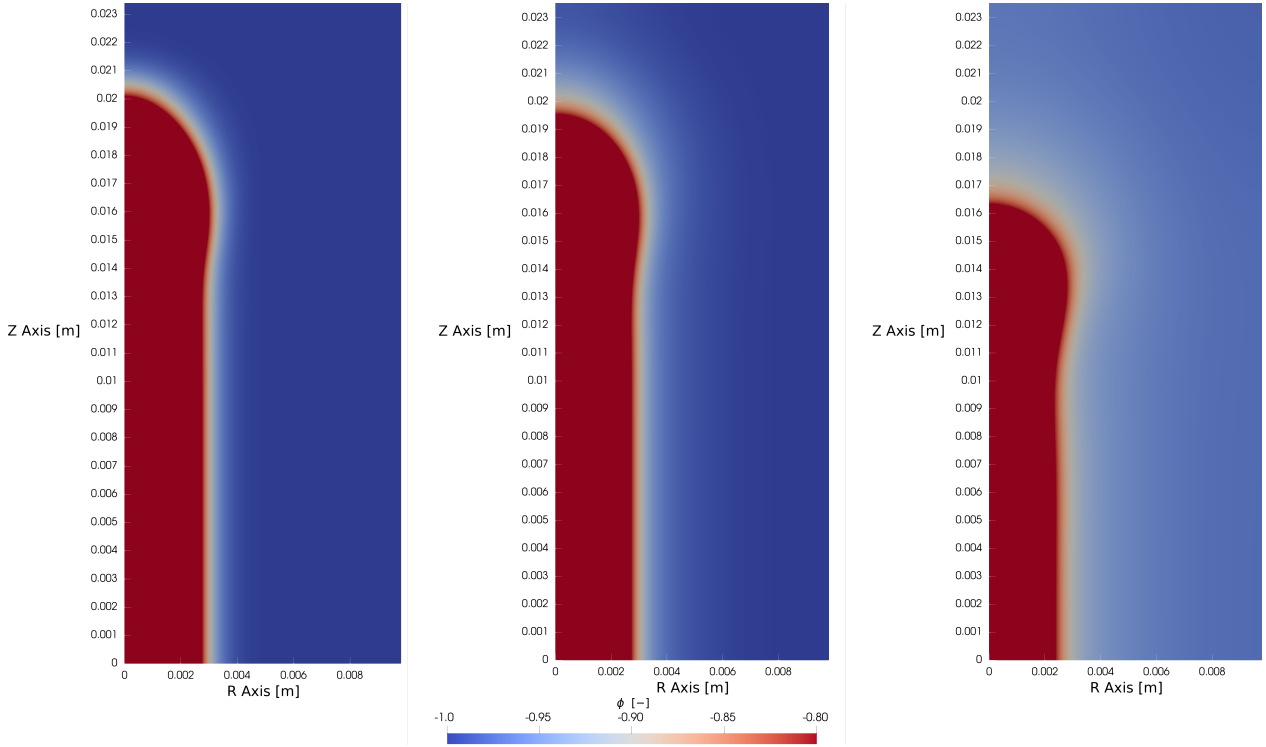


Figure 5.3: Phase mixing displayed by the phase field at $t = 0.01$ s. From left to right the mobility is $m = 10^{-7}$ m³/kg, $m = 10^{-6}$ m³/kg and $m = 10^{-5}$ m³/kg. Note that the color bar only displays phase for $-1 \leq \phi \leq -0.8$ to clarify the mixing process.

The influence of the mixing phenomena can be reduced in three ways. The first option is reducing ϵ which decreases the energy penalty on a phase gradient and increases the energy penalty of a mixed phase. However, decreasing the interface thickness increases the needed resolution of the FEM, and more elements increases computation time. The second option is reducing the size of the domain. The same amount of mixing in a smaller domain, results in a larger change in the phase field which increases the energy penalty on mixing. The third option is increasing the time scale of the mixing process. This will change the dynamic behavior of the filament, but will not influence the steady state solution. The influence of the mixing process is small if the mixing process time scale is large in comparison to the time scale of the filament contraction. However, this timescale also influences the interface expansion in case of refinements. Therefore, this so-called Cahn–Hilliard timescale cannot be increased indefinitely. This timescale is defined in Equation (5.3) in Section 5.2.5, which also presents more information on this timescale.

Phase mixing is the second phenomena which limits the mobility from above. This can be prevented by decreasing the interface thickness or decreasing the mixing speed by increasing the Cahn–Hilliard timescale. Decreasing the interface thickness is ideal theoretically: it decreases the mixing and is a better approximation of a sharp interface. However, thin interfaces need smaller elements and more refinement steps to obtain a

resolved solution. This increases the computation time and decreases robustness, which is often a limiting factor to the simulations.

5.1.3 General differences

All simulations with $m \leq 10^{-7} \text{ m}^3\text{s/kg}$ display the same qualitative behavior during the contraction phase of the filament. The contraction velocity increases slightly with increasing mobility, but this does not have a significant influence on the filament dynamics. However, there are differences between these simulations.

Figure 5.4 and 5.5 are used to show differences in the phase field and chemical potential field for different values of the mobility. The filaments with a low mobility, as shown in Figures 5.4b and 5.5b, show a small trail of phase mixing which is accompanied by high extreme values in the chemical potential. Filaments with a high mobility, as shown in Figures 5.4a and 5.5a, show a more widespread phase mixing and lower extreme values in the chemical potential.

This shows that the mobility influences the diffusion process. A low mobility limits the diffusion which results in localized phase mixing. This localized phase mixing comes with steep phase gradients and thereby high extreme values in the chemical potential.

The lower the mobility, the more localized this phase mixing becomes. In the end, this phenomena is limited by the resolution of the mesh. This also impacts the robustness of the simulations. Therefore, the mobility influences the robustness of the simulation, but more importantly also the mixing behavior and thereby the phase field. Figure 5.4 shows that the filament contours for the two different mobilities are almost identical. However, there are differences in the phase field inside of the filament. As already mentioned, the mixing phenomena localizes for a low mobility. This also results in lower values for the phase field inside the filament.

The phase mixing into the filament shows that the mobility is also limited from below. The limit, however, is dependent on the resolution of the mesh and the robustness of the simulation, where robust simulations with a fine mesh allow for lower values of the mobility parameter.

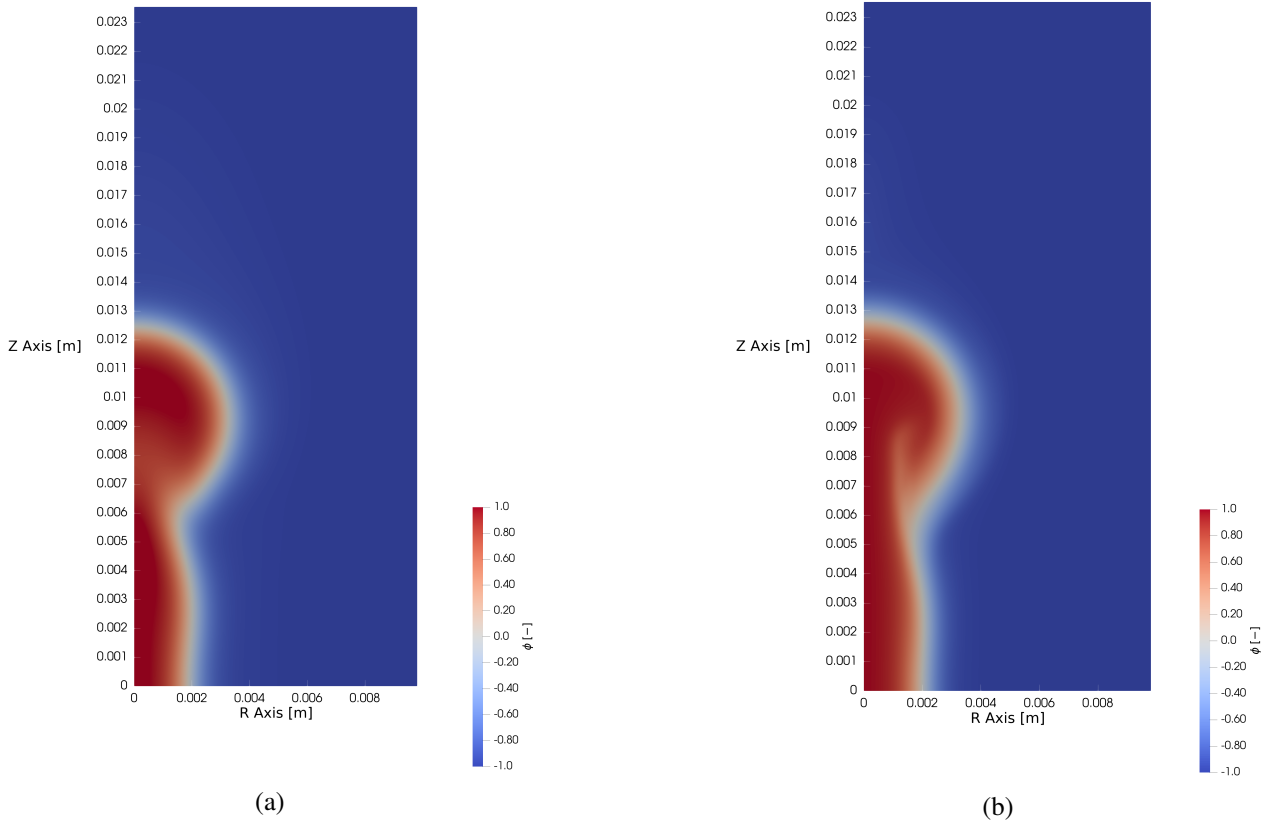


Figure 5.4: Plot of the phase field at $t = 0.05$ s for (a) $m = 10^{-7}$ m³/s/kg and (b) $m = 10^{-10}$ m³/s/kg.

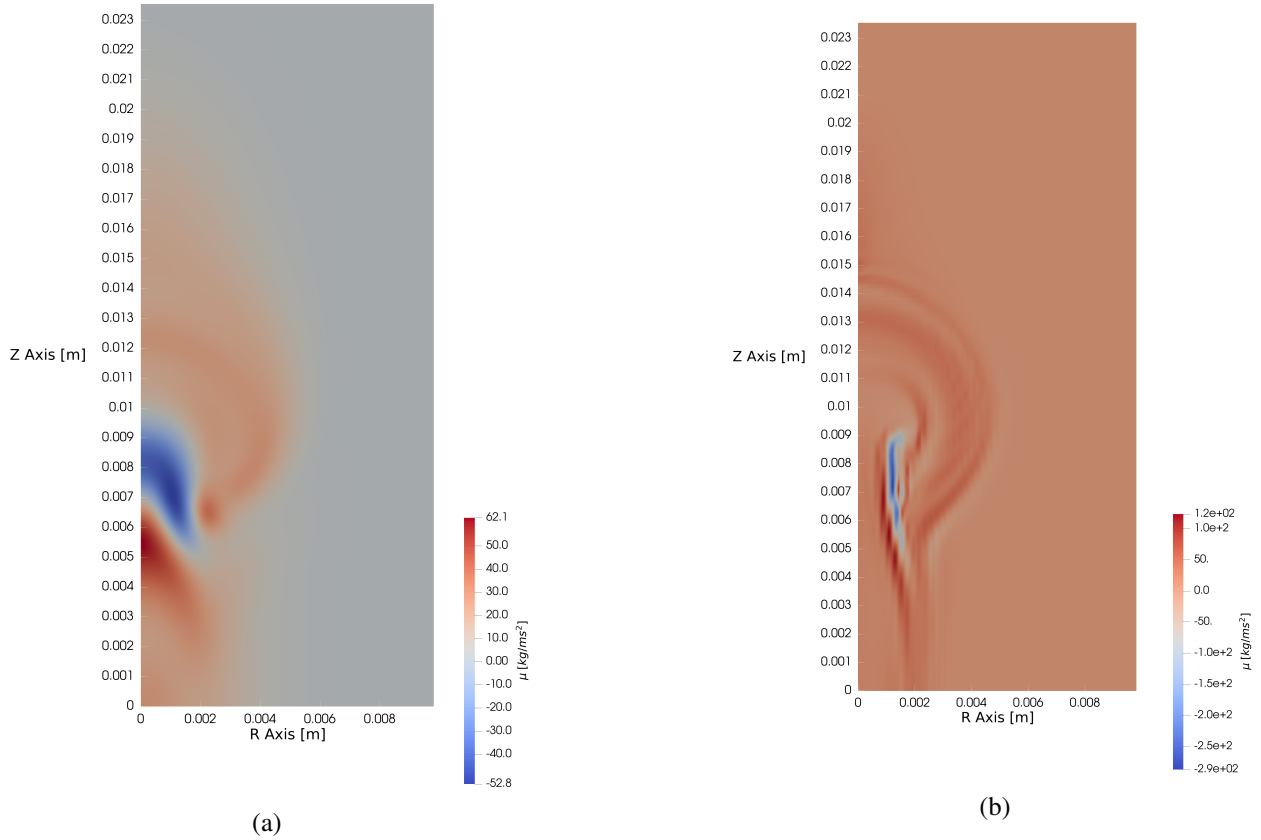


Figure 5.5: Plot of the chemical potential at $t = 0.05$ s for (a) $m = 10^{-7}$ m³/s/kg and (b) $m = 10^{-10}$ m³/s/kg.

5.2 Velocity field disturbance

The same filament is also considered in a more detailed simulation. The interface thickness is halved, and the simulation has 2 refinement steps, $L_{\max} = 2$, which are both continuation steps, $K = 2$. Therefore, the interface thickness on the coarsest is 4 times the input value and the mobility is 640 times the input value. During each refinement step, the top 95% of the largest error contribution is refined. The mobility is set to $m = 5 \cdot 10^{-9} \text{ m}^3\text{s/kg}$. This value is above the values with robustness problems and below the values with the high velocity flow phenomena. An overview of the applied parameter values is displayed in Table 5.2.

Table 5.2: Filament contraction parameters

Filament contraction simulation characteristics			
General:			
$\Delta t_{\max} = 1.25 \text{ ms}$	$\epsilon = 2.5 \cdot 10^{-4} \text{ m}$	$\sigma = 7.28 \cdot 10^{-4} \text{ kg/s}^2$	$m = 5 \cdot 10^{-9} \text{ m}^3\text{s/kg}$
Domain:			
Radius = $1.177 \cdot 10^{-2} \text{ m}$	Radial elements: 15	Height = $2.35 \cdot 10^{-2} \text{ m}$	Axial elements: 30
$L_{\max} = 2$	$K = 2$	$e_{\text{red}} = 95\%$	
Filament:			
$\rho_l = 1000 \text{ kg/m}^3$	$\eta_l = 10^{-3} \text{ kg/ms}$	$L_0 = 1.962 \cdot 10^{-2} \text{ m}$	$r_0 = 1.962 \cdot 10^{-3} \text{ m}$
Ambient:			
$\rho_a = 1 \text{ kg/m}^3$	$\eta_a = 10^{-4} \text{ kg/ms}$		

Problems occur during the simulation for the solutions on the coarsest mesh. The velocity field shows flow artifacts which disappear during refinement. Figure 5.6 shows the velocity field of the time step before the solver stagnates and the time step size is reduced drastically. Therefore, the simulation can not be completed within a reasonable time frame. This figure shows velocity disturbances in and around the interface. Around the end bulb of the filament there is an area where there is no clear flow direction. The flow direction appears to be random and the direction of the velocity vectors alternate. The velocity magnitude of these disturbances is significant with respect to the filament contraction velocity. The disturbances at low radii even show the highest velocities in the complete domain. The straight part of the filament should be stationary. However, there are velocity fluctuations in the interface which propagate into the ambient air. There is a periodic pattern with alternating flow directions for each line of high velocity. This disturbed velocity field is assumed to be the cause of the drastic time step size reduction.

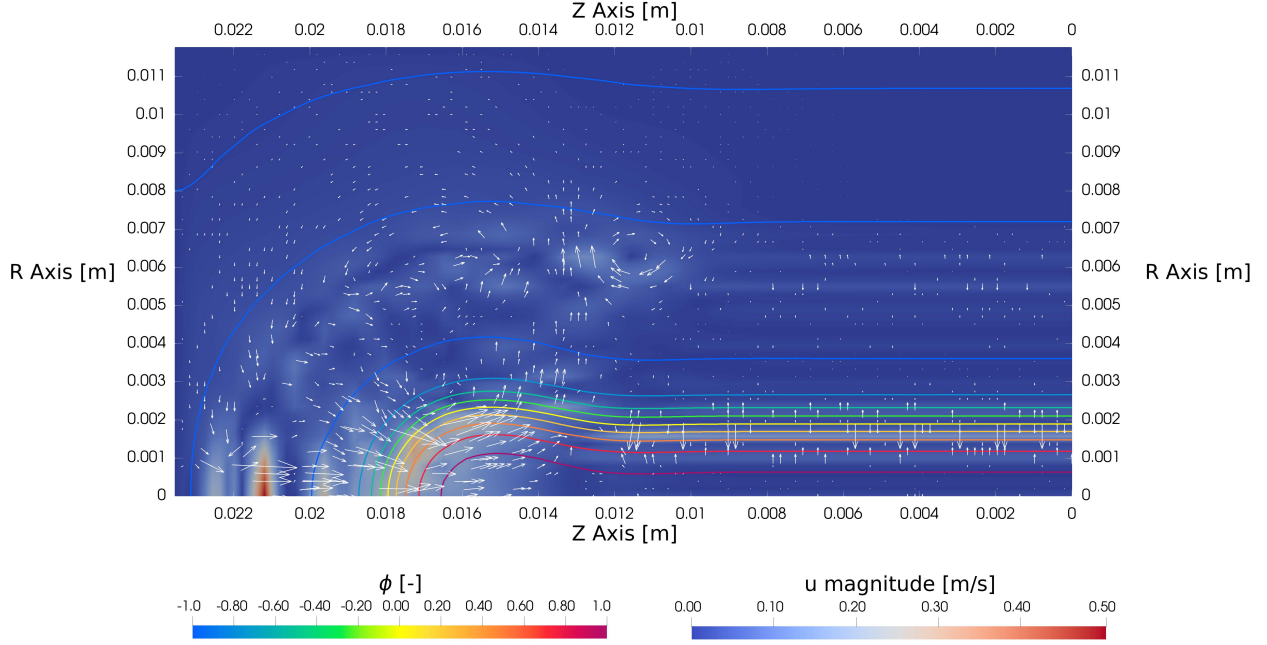


Figure 5.6: Velocity field of the filament contraction simulation with phase field contour lines at $t = 0.015$ s. The velocity field is a color map of the magnitude of the velocity with velocity vectors. This is the solution on the coarsest mesh.

During the filament contraction simulation it is observed that the velocity field is disturbed around the interface. This occurs at the first solution of a new time step, where the interface is expanded by the ϵ -continuation. The velocity field is disturbed in the ambient medium of which the viscosity and density are lower than those of the filament fluid. The disturbance which is visible on the coarsest mesh disappears during the refinement procedure. However, for some time steps the solution procedure is not completed as a result of the limited amount of iterations for the Newton-solver. This happens when the time step size is too large for the robustness of the simulation. The amount of needed Newton-solver iterations increases due to the complexity of the disturbed velocity field. This results in a drastic decrease of the time step size, which increases the computational time.

The problem of the extreme time step size reduction must be resolved before the filament contraction problem can be simulated completely. In this section possible causes will be assessed and a solution is proposed.

5.2.1 Interface expansion

A possible source of disturbance which is considered is the interface expansion. The interface expansion is part of the ϵ -continuation, as described in Section 4.4. A separate model will be made to specifically study these interface dynamics. These simulations are focused on better understanding the interface expansion process and try to find a correlation between the interface expansion and the disturbance of the velocity field. This model will be used to study this effect and the influence of density, viscosity and mobility. The model is simplified in comparison to the filament contraction model to reduce computational cost and reduce the complexity for analytical purposes.

Two types of interfaces are considered, a straight interface and a curved interface. The straight interface uses a 2D domain where there is no dependence on the height coordinate and the curved interface uses a 2D axisymmetric domain. Thus, both interfaces only depend on one spatial coordinate. The general characteristics for the simulations are described in Table 5.3. A more detailed explanation of the domain, the initial and boundary conditions is presented in Appendix B.1. These characteristics are close to the filament contraction case for comparative purposes. Sections 5.2.2 through 5.2.5 present the results of these simulations.

The initial interface is a quarter of the equilibrium width, which corresponds to interface expansion with two ϵ -continuation steps. Over time, the interface expands to an equilibrium. In the filament contraction simulations the expansion due to ϵ -continuation occurs in one time step. Therefore, the first time step is most significant with respect to the disturbed velocity field. The results for the velocity fields presented in these sections are based on the first time step. The simulation are performed for a larger time span and these results are analyzed. These results are used to determine the time scale of this problem.

Table 5.3: Simulation characteristics to study the effect of interface expansion

Mobility simulation characteristics		
General:		
$\epsilon_{eq} = 1 \cdot 10^{-3}$	$\epsilon_0 = 2.5 \cdot 10^{-4}$	$\sigma = 7.28 \cdot 10^{-2} \text{ kg/s}^2$
Low mobility:	$m = 5 \cdot 10^{-8} \text{ m}^3\text{s/kg}$	$\Delta t_{max} = 1.25 \text{ ms}$
High mobility:	$m = 5 \cdot 10^{-7} \text{ m}^3\text{s/kg}$	$\Delta t_{max} = 0.125 \text{ ms}$
Water:		
$\rho_l = 1000 \text{ kg/m}^3$	$\eta_l = 10^{-3} \text{ kg/ms}$	
Air:		
$\rho_a = 1 \text{ kg/m}^3$	$\eta_a = 10^{-5} \text{ kg/ms}$	
Straight interface:		
$x_0 = 0.5 \cdot 10^{-2} \text{ m}$	width= $1 \cdot 10^{-2} \text{ m}$	height= $1.25 \cdot 10^{-3} \text{ m}$
Curved interface:		
$r_0 = 1.962 \cdot 10^{-3} \text{ m}$	$R_{domain} = 5.886 \cdot 10^{-3} \text{ m}$	

5.2.2 Mesh dependence

The velocity disturbance after the interface expansion seems to be a discretization error. Therefore, the simulation is performed on meshes with different element sizes to study the convergence. The convergence is studied for second and third order basis functions for the velocity, because the third order elements were implemented after model improvements. The phase field and velocity field are analyzed. An example of a velocity profile on a coarse interface is shown in Appendix B.3. The combined results of all simulations are shown in Figure 5.7, which shows the maximum magnitude of the velocity disturbance for different element sizes.

Figure 5.7 shows that the maximum magnitude of the velocity disturbance decreases for decreasing element size. Results with an element size larger than the initial interface thickness parameter ϵ_0 generally display significant error due to under-resolution on interface. This is displayed in the results. The time step size was halved for the simulation with second order basis functions on the coarsest tested mesh. For this case the Newton-Algorithm did not reduce the residual sufficiently. Therefore, these solutions were not accepted and the time step size was reduced.

The magnitude of the velocity disturbance decreases with decreasing element size if the element size is adequately smaller than the initial interface thickness. This shows that the velocity disturbance is a spatial discretization error. As expected, the convergence rate of the simulations with the third order velocity basis function is also of the third order. The convergence rate of the results of the simulations with the second order velocity basis functions is even faster than second order. This can for instance be a result of the symmetry of the domain. However, this will not be considered any further.

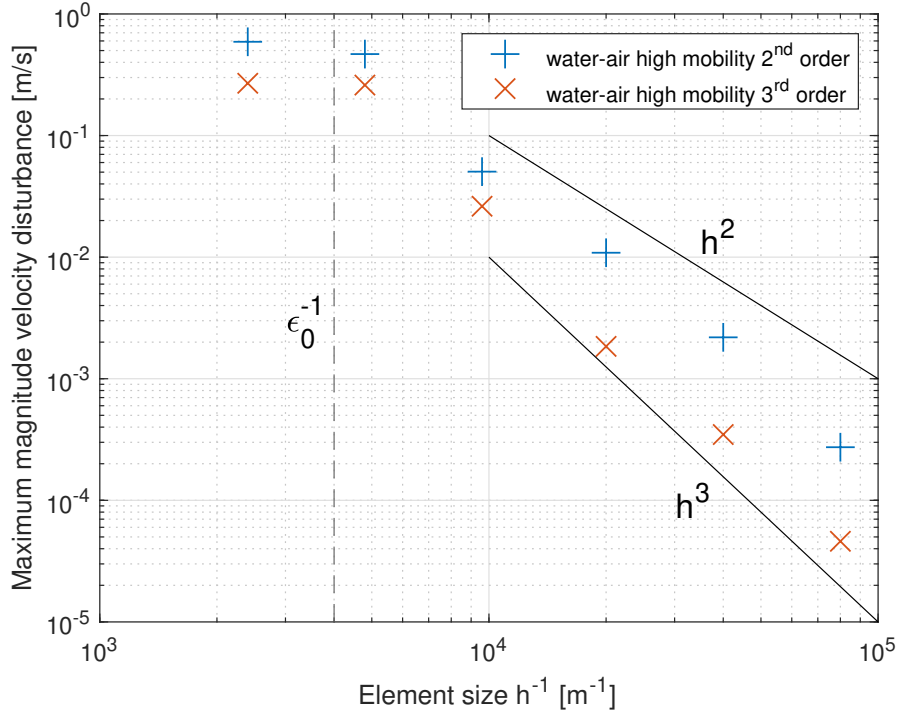


Figure 5.7: Magnitude of the velocity fluctuation for a water-air interface at high mobility after the first time step at $t = 0.125$ ms dependent on element size and order of the basis functions. Note that the simulation with second order basis functions and the largest element size needed a time step division and therefore the shown velocity is at $t = 0.0625$ ms. The vertical dashed line shows the interface thickness parameter of the initial interface and the black lines show the second and third order convergence rates.

The coarsest mesh used in the filament contraction simulations is comparable to the coarsest mesh shown in Figure 5.7. Therefore, there are only a few elements on the interface. However, the refinement procedure prevents a resolution problem. The magnitude of the velocity disturbance for this mesh size is around the same value as the filament contraction velocity, independent of the order of the basis functions. For this element size the velocity disturbance is significant with respect to filament contraction velocity.

Another simulation with a non expanding interface was performed on a coarse mesh to ensure that the velocity disturbance originates from the interface expansions. A non-expanding interface shows small velocity perturbation in the order of 10^{-5} m/s. Thus, it can be concluded that the interface expansion can cause significant velocity disturbance on coarse meshes and the magnitude of this disturbance decreases with a decreasing element size.

Reducing the element size is a possible solution. However, this increases the computation time significantly and is not necessary for the solutions on the finer meshes. A solution which does not increase the computation time is preferred. A possible solution was found in the fluid characteristics. The interface expansion case was also performed for different fluids. It was observed that there is a dependence on the density and viscosity. This is elaborated in Section 5.2.3.

5.2.3 Medium dependence

The interface expansion simulations are performed for 3 different combinations of fluids. These combinations are water-water, water-air and air-air, all used with the high mobility according to Table 5.3. This set contains differences in absolute values and ratios of viscosities and densities. Figures 5.8 and 5.9 show the velocity profiles for the straight interfaces in the first time step for the water-water and water-air interfaces and for the air-air interfaces respectively. Note that the value for the surface tension is kept constant and

equal to the surface tension of a water-air interface.

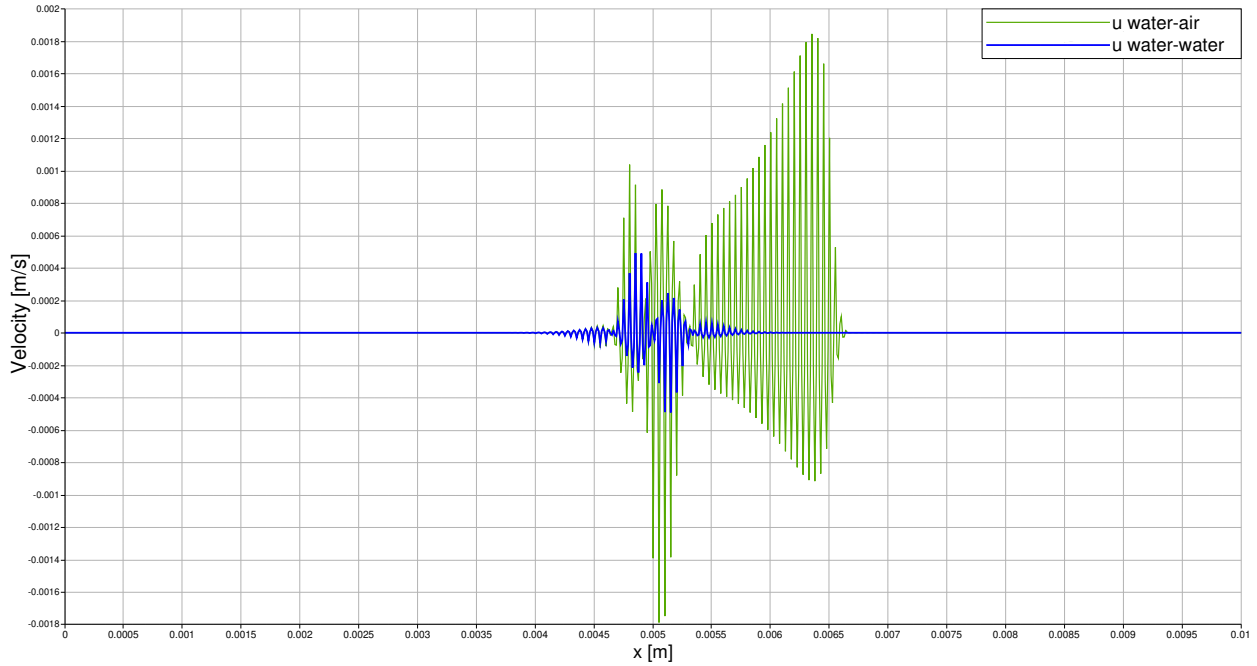


Figure 5.8: Velocity field for the straight water-water and water-air interfaces for $t = 0.125 \text{ ms}$. The interface is situated around $x = 0.005 \text{ m}$. For the water-air interface, the water phase is situated on the lower x values.

The water-water interface data in Figure 5.8 shows that the velocity profile is anti-symmetric in the interface for equal density and viscosity. Figure 5.9 shows the same behavior for the air-air interface. The water-air interface shows that in the case of unmatched fluid characteristics, the disturbance in the velocity profile is larger in the phase with lower density and viscosity. In this phase, there is also a disturbance further away from the interface. Comparing the water-water interface with the air-air interface it is clearly shown that the lower the density and viscosity are, the higher the velocity disturbance is. A similarity between all the velocity profiles is a fluctuation between positive and negative velocities; there is no clear flow direction.

The magnitude of the fluctuating velocity is different for each interface. The water-water and water-air interface have velocity fluctuations which are at least 2 orders lower than the filament contraction velocity. A theoretical approximation for the filament contraction velocity is $u_{\text{cap}} = \sqrt{\frac{\sigma}{\rho r_0}} = \sqrt{\frac{7.28 \cdot 10^{-2} \text{ kg/s}^2}{10^3 \text{ kg/m}^3 \cdot 1.96 \cdot 10^{-3} \text{ m}}} = 0.19 \text{ m/s}$ (Driessen et al., 2013). The velocity for the air-air interface is higher and significant in comparison with the filament contraction velocity. However, the theoretical contraction velocity for an air filament increases as well. Overall, it is important to point out that the velocity disturbance is influenced significantly by the density and viscosity of the media. This could be used to decrease the velocity fluctuations without decreasing the element size.

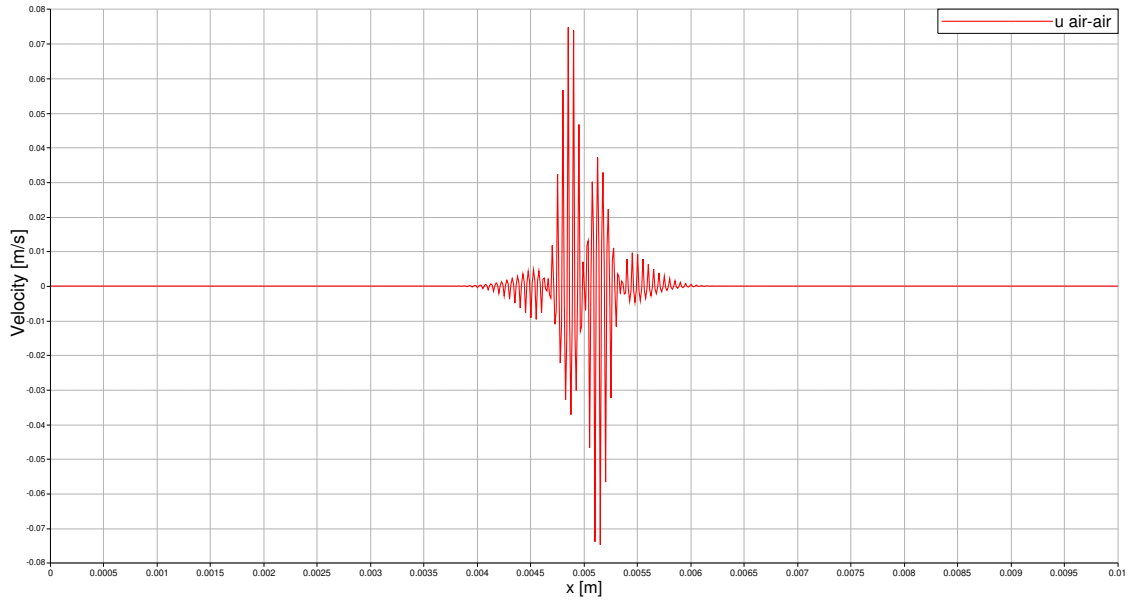


Figure 5.9: Velocity field for the straight air-air interface for $t = 0.125 \text{ ms}$. The interface is situated around $x = 0.005 \text{ m}$.

Figure 5.10 shows the velocity profiles in the first time step for a straight water-air interface for two different mobilities. The results are assessed at the same dimensionless time, $t^* = t/\tau_{\text{CH}}$. Section 5.2.5 explains that this time scale governs the interface expansion. The velocity profiles are examined at two different instances in time, such that t^* is the same for both mobilities. Therefore, the differences are a result of the different mobilities instead of different moments of assessment. The figure shows that especially around the interface the velocity of the fluctuation is significantly lower for the higher mobility. Figure B.3 in Appendix B.2 shows the same results for the curved interface. The velocity magnitudes are comparable, and the same dependence on the mobility is found. It is unexpected that the velocity magnitude decreases for an increasing velocity, because the mobility governs the interface dynamics in the way that the dynamics speed up for increasing mobility.

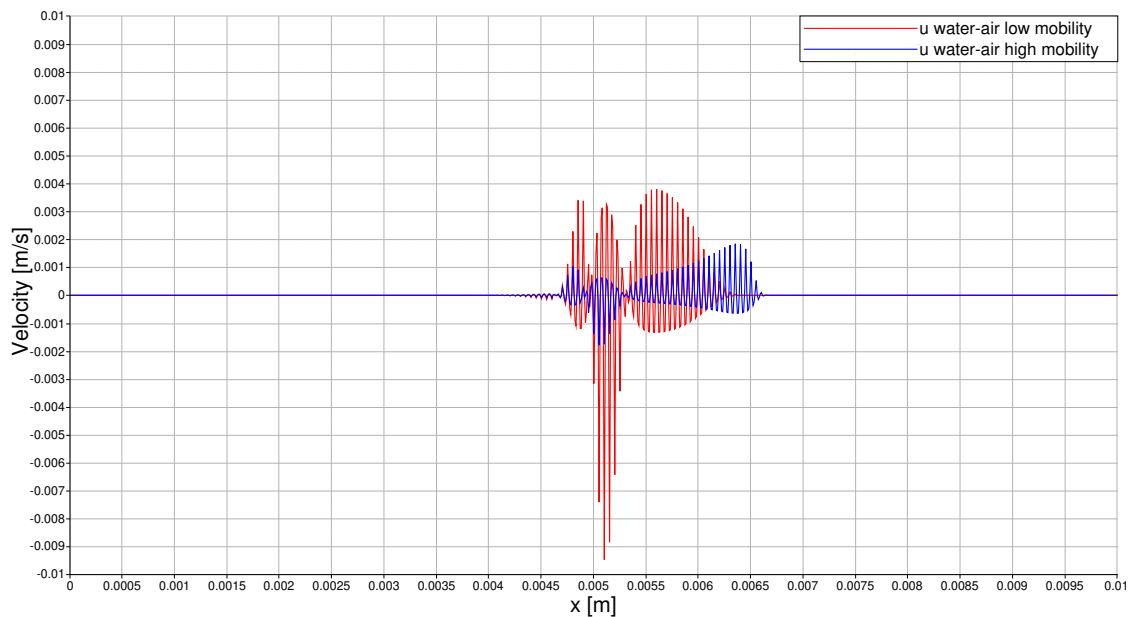


Figure 5.10: Velocity field for the straight water-air interface for 2 different mobilities: for the high mobility at $t = 0.125 \text{ ms}$ and the low mobility at $t = 1.25 \text{ ms}$. The interface is situated around $x = 0.005 \text{ m}$.

5.2.4 ρ - η -continuation

The one dimensional interface expansion simulations presented in Sections 5.2.2 and 5.2.3, convey two links to the disturbance of the velocity field. The first one pertains to the viscosity and density of the medium. The second one is the link between the element size and the magnitude of the velocity fluctuation. Increasing the viscosity and density or decreasing the element size are two options to decrease the disturbance of the velocity field. Decreasing the element size increases the computational cost of the models, which is a limiting factor for the filament contraction model. However, increasing the density and viscosity of either one or both of the media changes the problem.

A possibility is an additional continuation procedure in conjunction with the ϵ -continuation in Section 4.4. The continuation procedures rely on the fact that for the Newton-procedure the solution on coarse mesh are only used to make a projection onto the finer mesh, to serve as an initial guess. Therefore, the density and viscosity can be artificially increased on the coarser meshes and reduced back to the correct fluid characteristics during the refinement steps. This changes the solution procedure and the projection onto the finest mesh, but the final solution is essentially unaltered. Normally, the increased density and viscosity influence the SEMR method, which was explained in Section 4.3, and therefore influence the final mesh. This ρ - η -continuation reduces the magnitude of the velocity fluctuations around the interface by artificially increasing the density and viscosity.

The implementation of this procedure can be adapted to the specific problem. For example, the density and viscosity can be scaled linearly or exponentially over the refinement steps. The following aspects need to be taken into account. First of all, the velocity fluctuations are most significant on the first refinement steps because the interface expansion is the largest. The altered viscosity and density change the refinement procedure. The flow phenomena in a lighter and less viscous fluid can have a smaller length scale which need more refinements. Therefore, there must be sufficient refinement steps in which the fluid characteristics differ from each other to ensure correct refinement.

An example is given for the filament contraction case. The density and viscosity of the air phase are increased to become equal to those of water on the coarsest mesh. Afterward, these are decreased linearly over the refinement steps, such that the original values are recovered on the finest mesh. It uses multipliers which make sure that the density and viscosity are increased to the highest values of the two fluids. During the $L = 0, 1, 2, \dots, L_{\max}$ refinement levels, the density and viscosity are only decreased for the initial $K - 1$ refinement steps. For the filament contraction case the density and viscosity multipliers are defined as follows:

$$\begin{aligned}
 \rho_{\text{mult},l} &= \max \left(1, \frac{\rho_a}{\rho_l} \frac{K - 1 - L}{K - 1} \right), \\
 \rho_{\text{mult},a} &= \max \left(1, \frac{\rho_l}{\rho_a} \frac{K - 1 - L}{K - 1} \right), \\
 \eta_{\text{mult},l} &= \max \left(1, \frac{\eta_a}{\eta_l} \frac{K - 1 - L}{K - 1} \right), \\
 \eta_{\text{mult},a} &= \max \left(1, \frac{\eta_l}{\eta_a} \frac{K - 1 - L}{K - 1} \right).
 \end{aligned} \tag{5.2}$$

This method is added to the numerical methods described in Section 4. A simulation is performed using the parameters described in Table 5.2. The results on the finest grid should be similar, while the solution procedure and the results on the coarser grid will be different.

The time step size for the first 5 time steps is equal. The results in time step 5 are identical for the phase field, velocity field, pressure and chemical potential. Afterward, there are some differences between the results. The differences are insignificant in the process of the filament contraction.

The results are similar with a few exceptions. First of all, the SEMR method generates a different mesh.

The simulation with ρ - η -continuation generates a mesh which is more refined around the interface, while the simulation which is described at the beginning of this chapter generates a mesh which is refined around the interface and also in the ambient medium. The refinements are based on errors in the phase field and the velocity field. The ρ - η -continuation reduces the velocity in the ambient medium which results in smaller errors, and less refinements. This leads to a reduction of the number of the degrees of freedom (DOFs) due to the application of the ρ - η -continuation. The different refinement procedure affects the accuracy of the solution in the less dense and less viscous medium.

Another influence on the discretization method is the influence on time step repetition. The ρ - η -continuation increases the robustness of the simulation, especially on the coarse meshes. This results in fewer time step size reductions, which change the course of the simulation. The results can change because the time step size is based on robustness of the simulation instead of the accuracy. A more robust simulation experiences less time step reductions which can increase the temporal discretization errors. Overall, the ρ - η -continuation results in different spatial and temporal discretizations which influence the simulation results.

The goal of the ρ - η -continuation is to increase robustness for the Newton-solver and prevent oscillation-induced refinements. The time step size is reduced fewer times in the filament contraction case, and the solver uses less time to find the solution. This is a result of the decrease in DOFs and fewer required iterations. The number of iterations is reduced due to the reduction of disturbance in the velocity field. Figure 5.11 shows the velocity field at the same moment in time as Figure 5.6. The disturbances around the end bulb of the filament are reduced, as well as the velocity fluctuations in the ambient medium next to the straight part of the filament. The magnitude of the velocity is reduced and the highest velocity is found in the contracting part of the filament.

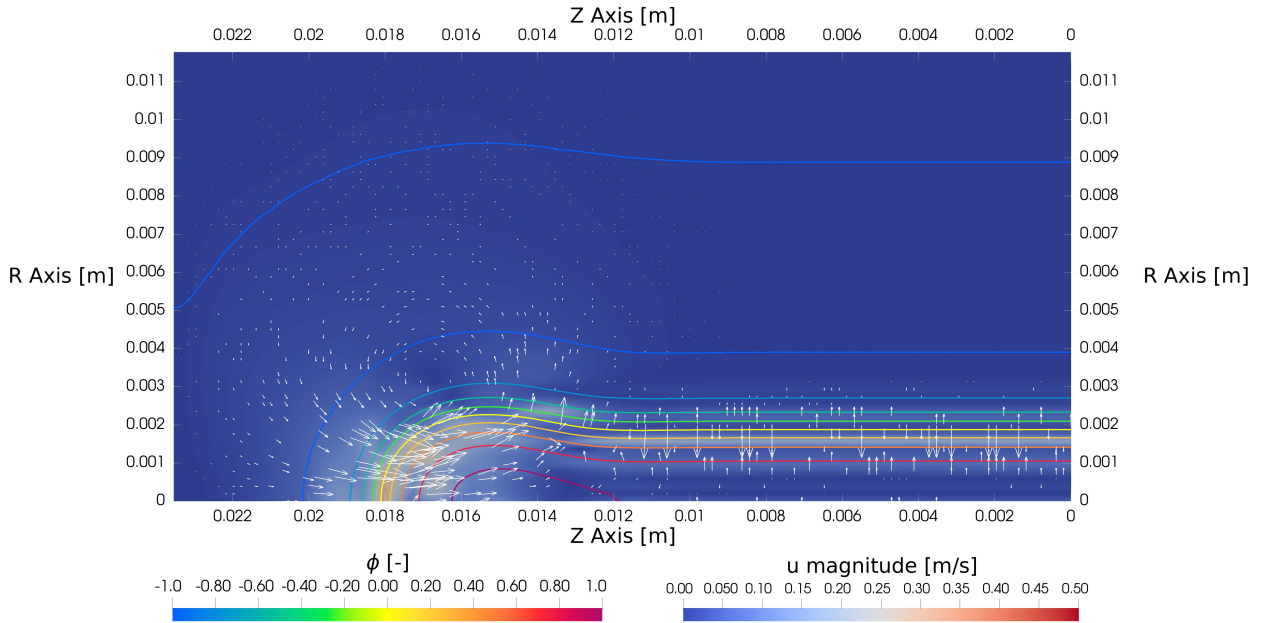


Figure 5.11: Velocity field of the filament contraction simulation including ρ - η -continuation with phase field contour lines at $t = 0.015$ s. The velocity field is a color map of the magnitude of the velocity with additional velocity vectors. The color bar range is equal to Figure 5.6 for comparative purposes.

The ρ - η -continuation changes the spatial and temporal discretization of the problem and thereby, indirectly, also the results. The robustness of the simulation is increased by reducing the velocity disturbance and fluctuations on the coarser meshes. The ρ - η -continuation procedure significantly enhances the robustness of the solution procedure, enabling the computation of the air-water filament-contraction problem.

5.2.5 Cahn–Hilliard time scale

The velocity profiles in Section 5.2.2 and 5.2.3 varied between all simulations. However, the phase fields were similar for each simulation with equal mobility. Therefore, the interface expansion must be dominated by diffusion. This process is governed by the diffusive Cahn–Hilliard time scale:

$$\tau_{\text{CH}} = \frac{\epsilon^3}{\sigma m}. \quad (5.3)$$

This time scale will be verified using the same simulations, but assessed at a later moment in time.

Figure 5.12 displays the phase field of the interface expansion simulations for a straight interface for 3 different combinations of fluids. We consider air-air, water-water, and water-air interfaces. The used surface tension corresponds to a water-air interface. Therefore, the Cahn–Hilliard timescale is equal for all of these interfaces. It can be observed that the phase field is nearly identical for these 3 different types of interfaces.

Figure 5.12 shows that the phase field is almost identical for the interfaces of different fluids. The absolute values of the density and viscosity are different and the ratio between them differs as well. However, the Cahn–Hilliard timescale is equal for all three interfaces. This shows that the interface expansion process in a simplified test case is independent of the density and viscosity of the two phases. The similarity in the phase field for equal Cahn–Hilliard timescale is the first indication for the importance of this timescale for the interface expansion.

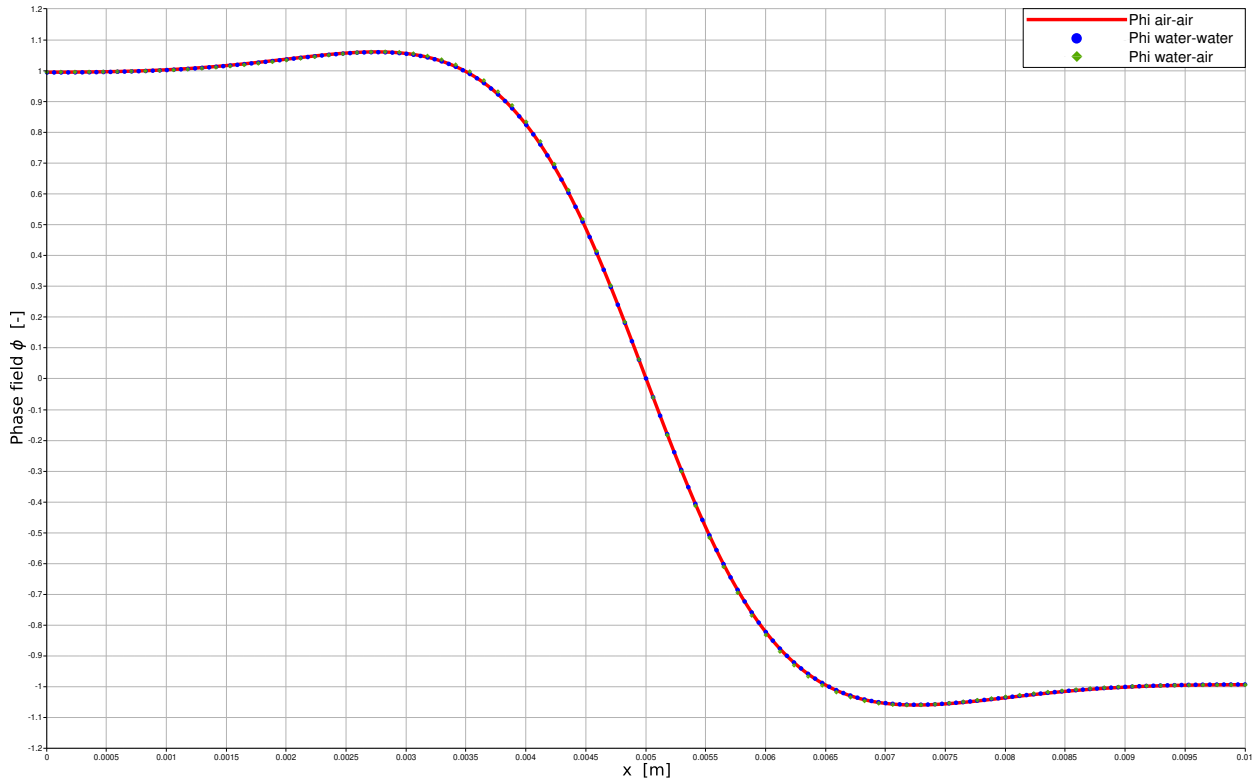


Figure 5.12: Phase field at $t = 4 \text{ ms}$ for water-water, water-air, and air-air interfaces at high mobility. Note that the water-water and water-air interface use markers for visibility purposes.

Three simulations will be performed on a water-air interface, one with the high mobility and one with the low mobility as described in Table 5.3. The third simulation uses a different interface thickness in combination with the high mobility. The surface tension is not varied, because the filament contraction problem uses a constant surface tension. The dimensionless time, $t^* = t/\tau_{\text{CH}}$, at which the phase field is analyzed, is equal for all simulations.

The simulation with the lower mobility has a higher Cahn–Hilliard time scale which is a factor 10 higher. Therefore, the time of assessment is also a factor 10 higher. The time step size for this simulation is also increased by a factor 10 to reduce the influence of the numerical method. The number of solution steps is equal at the time of assessment. As it was previously described, all other parameters are equal.

The simulation with a thicker interface has an interface thickness which is doubled with respect to the other simulations. Therefore, all dimensions are increased by the same factor, see the green axis in Figure 5.13. The mobility is increased by a factor 8. This results in a Cahn–Hilliard time scale which is equal to the one for the high mobility simulations and therefore, these two simulations are analyzed at the same moment in time.

The results of these 3 simulations are shown in Figure 5.13. The computed phase fields are almost identical at the same dimensionless time t^* . This shows that the Cahn–Hilliard time scale governs the process of interface expansion. The interface expansion is an important part of the ϵ -continuation process. The Cahn–Hilliard time scale can be used to choose parameter values in a suitable way to increase or decrease the interface expansion. This time scale can also be used for dimensional scaling of a problem.

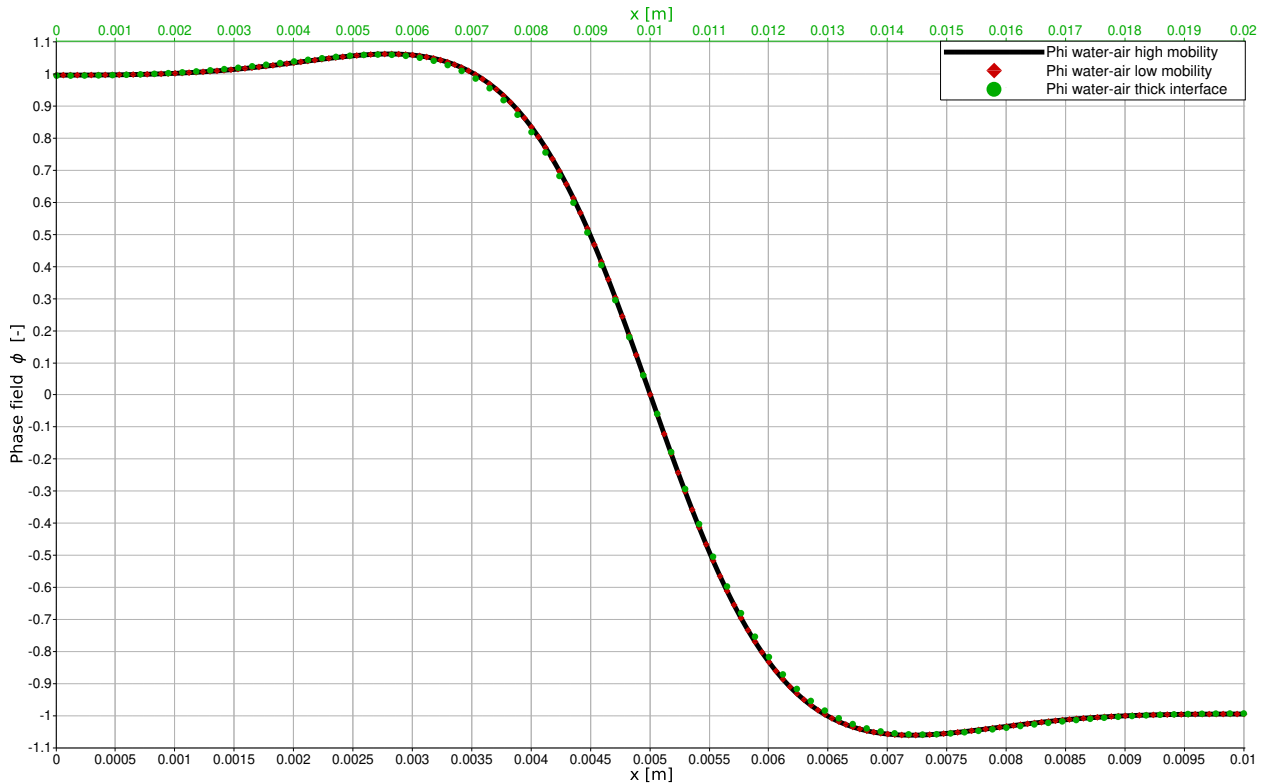


Figure 5.13: Phase field at $t = 4 \text{ ms}$ for the high mobility and the thick interface and at $t = 40 \text{ ms}$ for the low mobility. The green horizontal axis belongs to the green markers for the simulation with a thicker interface. The markers are used for visibility purposes.

The Cahn–Hilliard timescale is a good measure for the diffusion timescale of the model. This timescale can be used to study the effect of interface thickness and mobility on the filament contraction process. Comparing timescales with other processes is a helpful tool to find a suitable combination of interface thickness and mobility.

5.3 Conclusion

The performed simulations did not run long enough to simulate breakup. The first simulations were performed to investigate the contraction process and the detailed simulation encountered the velocity disturbance problem. Therefore, the breakup is not simulated and studied. However, the simulations provide information regarding the mobility parameter.

The most important finding is the large influence of the mobility parameter on the solution. On the one hand, a too high value for the mobility parameter can result in non-physical phenomena with high velocity. Phase mixing is highly dependent on the mobility. High mobility results in increased phase mixing to such extent that the filament decreases in size. On the other hand, a low mobility localizes the phase mixing which results in extreme values for the chemical potential and challenges the resolution of the mesh and robustness of the model. Although the mixing phenomena can be decreased by lowering the interface thickness, it is important to note that the computation time is strongly dependent on the interface thickness.

The mobility strongly influences the diffusion process. The corresponding Cahn–Hilliard timescale is an important indicator for the interface expansion, the phase mixing, and the occurrence of the high velocity flow phenomena. Of course, this timescale must be regarded in a comparison to other timescales.

A high mobility value results in relatively fast diffusion. The diffusion is needed for the interface expansion in the ϵ -continuation. However, in case of a relatively thick interface, this diffusion also results in phase mixing. A too high mobility results in high-velocity errors which disrupt the simulation. A low mobility results in slow equilibration of the interface. This leads to localized flow phenomena which challenge the mesh resolution and influence the robustness of the simulation.

The influence of either the mobility or interface thickness on breakup is still unknown. It requires either a larger domain or longer time intervals to test the different cases of breakup. The computational time needed for these simulation is outside the scope of this project. Therefore, the model will be applied to a different case, which is the numerical experiment described in Section 6.

Velocity disturbance encountered on a coarse mesh was caused by interface expansion. This is a discretization error and can be reduced by decreasing the element size. A solution which does not increase the computation time was found in the form of the ρ - η -continuation procedure. The ρ - η -continuation procedure significantly enhances the robustness of the solution procedure on the coarse meshes.

6 Rayleigh–Plateau instability and rupturing

The filament breakup is studied using an infinitely long filament which succumbs to Rayleigh–Plateau instabilities. An infinitely long filament is used to decrease the domain size and thereby the computation time. The filament breakup will be studied to investigate the influence of the two model parameters on topological changes and small length scale phenomena. Specifically, the breakup time and filament shape at breakup will be studied. The reduced computation time creates the opportunity to simulate thinner interfaces to approach the sharp interface limit more closely. The singularity at the point and moment of breakup will also test the robustness of the model.

In this section, theory about this type of instability is explained. Afterward, the simulation results are presented and conclusions are drawn.

6.1 Rayleigh–Plateau instabilities

Rayleigh–Plateau instabilities are capillary waves which can make a filament unstable (Anthony et al., 2019; Driessen et al., 2013; Eggers & Villermaux, 2008). This mode of breakup is called Rayleigh breakup in the breakup modes described in Section 2. The capillary waves are unstable if the wavelength is larger than the circumference of the filament (Plateau, 1873). The amplitude of the perturbation increases exponentially and the Rayleigh breakup occurs when the amplitude is around the same value as the radius of the filament.

The growth rate of the perturbations is dependent on the filament and ambient fluid properties and the wavelength of the perturbations. (Driessen et al., 2013) make a linear approximation to a fluid filament with a small perturbation, which is described by a sinusoidal perturbation:

$$R(z, t) = r_0 + \tilde{R}(t) \cos\left(\kappa \frac{z}{r_0}\right), \quad (6.1)$$

where the amplitude is defined as:

$$\tilde{R}(t) = \delta e^{\omega(t-t_0)}. \quad (6.2)$$

Here, $\kappa = 2\pi r_0/\lambda$ is the dimensionless wave number, λ is the wave length, ω is the growth rate of the perturbation, t_0 is the time at which the perturbation starts, and δ is the initial perturbation amplitude.

(Rayleigh, 1892) found that $\kappa_{\max} \approx 0.7$ is the most amplified wave number for an inviscid fluid, which is called the Rayleigh mode (Eggers & Villermaux, 2008). This follows from a dispersion relation which links the growth rate to the wave number. This dispersion relation follows from the linear approach. This relation between the wave number and the growth rate has been verified experimentally (Eggers & Villermaux, 2008).

The maximum growth rate for the perturbations in viscous filaments occurs at larger wave lengths than the Rayleigh mode (Driessen et al., 2013; Eggers & Villermaux, 2008). This follows from an altered dispersion relation which includes the filament viscosity but neglects the ambient fluid. The growth rate for a viscous filament is:

$$\omega\tau_{\text{cap}} = \sqrt{\frac{1}{2}(\kappa^2 - \kappa^4) + \frac{9}{4}\text{Oh}^2\kappa^4} - \frac{3}{2}\text{Oh}\kappa^2, \quad (6.3)$$

where:

$$\tau_{\text{cap}} = \sqrt{\frac{\rho l r_0^3}{\sigma}}, \quad (6.4)$$

is the capillary time scale for infinitely long filaments. Therefore, the wave number for the fastest growth rate is given as a function of Oh:

$$\kappa_{\max} = \frac{1}{\sqrt{2 + 3\sqrt{2}\text{Oh}}}. \quad (6.5)$$

This relation includes the viscous effects of the filament, but neglects any influence of an ambient fluid.

(Rayleigh, 1892) presented the dispersion relation for the hollow jet approximation, a limiting case where $\rho_l \ll \rho_a$. (Tomotika, 1935) presents the dispersion relations for the limiting cases where $\eta_l \gg \eta_a$ and $\eta_l \ll \eta_a$ and also the general case for arbitrary viscosities. However, these relations neglect inertial effects. The filament which is researched in this section is a water filament in ambient air. Therefore, the theory for a viscous filament in the absence of an ambient fluid is used.

The water filament in the ambient air is situated in the domain described by the case description in Section 3.2. The fluid properties and case parameters of this filament are given in Table 6.1. These parameters are chosen to approach the length and time scale of an inkjet process.

Table 6.1: Filament and ambient characteristics for the Rayleigh–Plateau case

General:		
$r_0 = 2 \cdot 10^{-5} \text{ m}$	$\delta = 0.01 \cdot r_0$	$\sigma = 7.28 \cdot 10^{-2} \text{ kg/s}^2$
Water:		
$\rho_l = 1000 \text{ kg/m}^3$	$\eta_l = 10^{-3} \text{ kg/ms}$	
Air:		
$\rho_a = 1 \text{ kg/m}^3$	$\eta_a = 10^{-4} \text{ kg/ms}$	

The important length scales in the problem are the interface thickness and the filament radius. The capillary time scale for this problem is:

$$\tau_{\text{cap}} = \sqrt{\frac{\rho_l r_0^3}{\sigma}} = \sqrt{\frac{1000 \text{ kg/m}^3 (2 \cdot 10^{-5} \text{ m})^3}{7.28 \cdot 10^{-2} \text{ kg/s}^2}} = 1.05 \cdot 10^{-5} \text{ s}. \quad (6.6)$$

The Cahn–Hilliard time scale will be an independent variable for the different simulations. The Oh for this simulation is:

$$\text{Oh} = \frac{\eta_l}{\sqrt{\rho_l r_0 \sigma}} = \frac{10^{-3} \text{ kg/ms}}{\sqrt{1000 \text{ kg/m}^3 \cdot 2 \cdot 10^{-5} \text{ m} \cdot 7.28 \cdot 10^{-2} \text{ kg/s}^2}} = 2.62 \cdot 10^{-2}. \quad (6.7)$$

Therefore, this filament is in the intermediate viscosity regime. If this filament was finite it would break up due to complex oscillations, capillary wave breakup or end-pinching. However, these breakup modes require the filament to completely contract or have end bulbs. Even if the filament is not in the viscous regime, the breakup mode will be Raleigh breakup in case of the infinitely long filament.

Although the filament is in the intermediate viscosity regime, the approach to determine the wave number for the largest disturbance growth rate for viscous filaments will be used. This is the closest representation of the situation. The wave number corresponding to the fastest growth is:

$$\kappa_{\text{max}} = \frac{1}{\sqrt{2 + 3\sqrt{2}\text{Oh}}} = \frac{1}{\sqrt{2 + 3\sqrt{2} \cdot 2.62 \cdot 10^{-2}}} = 0.688. \quad (6.8)$$

This is almost equal to the wave number of the Rayleigh mode because this filament is relatively inviscid compared to the finite filaments which experience Rayleigh breakup. The wave length of the most amplified disturbance becomes:

$$\lambda_{\text{max}} = \frac{2\pi r_0}{\kappa_{\text{max}}} = 1.83 \cdot 10^{-4} \text{ m}. \quad (6.9)$$

Using symmetry boundary conditions, it is possible to only model half of a disturbance wave which will represent the complete filament.

The filament will break if the amplitude of the disturbance is equal to the radius of the filament, $\tilde{R} = r_0$. For the linear approximation, this results in the following expression for the breakup time:

$$t_b = t_0 + \frac{1}{\omega_{\text{max}} (\text{Oh})} \log\left(\frac{r_0}{\delta}\right) = 0 \text{ s} + \frac{1}{3.2 \cdot 10^5 \text{ s}^{-1}} \log(100) = 1.44 \cdot 10^{-4} \text{ s}. \quad (6.10)$$

It is important to note that this theoretical breakup time follows from a linear approximation which also neglects the inertial and viscous influence of the ambient fluid.

6.2 Numerical experiment

The numerical experiments for the Rayleigh-Plateau instability case will cover a range of interface thicknesses and mobilities. This results in a set of Cahn–Hilliard timescales. These model parameters are chosen such that the Cahn–Hilliard timescale is equal or smaller to the capillary timescale of this problem. This ensures that the interface can equilibrate. The range of interface thickness and mobilities and the according Cahn–Hilliard timescale, are shown in Table 6.2. The interface thickness is scaled by factors of 2 and therefore the mobility is scaled by factors of 8 to make sure that there are similar values for the Cahn–Hilliard timescale. Only one simulation with the thinnest interface is performed due to time restrictions.

Table 6.2: Cahn–Hilliard timescale, τ_{CH} [s], for the Rayleigh–Plateau instability simulations

ϵ [m]	m [$\text{m}^3\text{s}/\text{kg}$]	10^{-12}	$8 \cdot 10^{-12}$	$6.4 \cdot 10^{-11}$	$5.12 \cdot 10^{-10}$	$4.096 \cdot 10^{-9}$
$0.5 \cdot 10^{-6}$		$1.72 \cdot 10^{-6}$ [9]				
10^{-6}		$1.37 \cdot 10^{-5}$ [5]	$1.72 \cdot 10^{-6}$ [6]	$2.15 \cdot 10^{-7}$ [7]	$2.68 \cdot 10^{-8}$ [8]	
$2 \cdot 10^{-6}$			$1.37 \cdot 10^{-5}$ [1]	$1.72 \cdot 10^{-6}$ [2]	$2.15 \cdot 10^{-7}$ [3]	$2.68 \cdot 10^{-8}$ [4]

The fluid characteristics for these simulations are defined in Table 6.1, the model parameters are defined in Table 6.2 and the remaining parameters regarding the domain and the numerical method are shown in Table 6.3. Simulations [1] up to and including [8] have a uniform mesh without refinements to reduce the computation time. Simulation [9] uses two refinement steps which are both continuation steps. The increase of the mobility by the ϵ -continuation is altered to $m_L = 2^{3(K-L)} \cdot m$, such that the τ_{CH} is constant during the refinements.

Exploratory simulations showed that this case is more robust than the filament contraction case. This can be caused by a higher Oh, the smaller length scale or the different dynamics. This resulted in inaccuracies due to large time step size. This is a result from a time step which is limited by robustness instead of accuracy. The phase field showed undershoot below $\phi = -1$ and overshoot above $\phi = 1$. Simulations with a smaller time step size showed a reduced undershoot and a slightly reduced overshoot.

To limit these errors using the time step repetition method as explained in Section 4.7, the maximum amount of Newton-iterations was reduced for simulations [1] through [8] and the convergence threshold of the residual was lowered as well. Another condition for the acceptance of a solution was formulated. The time step size is halved if this condition is not met. The phase field of a solution on the finest mesh is required to be $\phi > -1 - \beta$, where $\beta = 5 \cdot 10^{-3}$ for simulations [1] through [8] and $\beta = 3 \cdot 10^{-2}$ for simulation [9]. However, for simulation [9] just before breakup the time step size reduced to the order of 10^{-10} s due to phase field undershoot. Therefore, it was concluded that the undershoot in this specific simulation is not a temporal discretization error. To complete this simulation the maximum time step size for $t > 0.17140625$ ms was reduced to $\Delta t_{\max,2} = 3.90625 \cdot 10^{-8}$ s. This corresponds to a time step which is halved 6 times with respect to the original time step.

Simulations [4] and [8], which are the simulations with the smallest τ_{CH} , showed the high velocity flow phenomena which were also observed at the side of the contracting filament in Section 5.1.1. The phenomena were observed in the oscillating droplet, right after the moment of breakup. The solution procedure was not disrupted by this phenomenon.

Table 6.3: Rayleigh–Plateau simulation parameters

Domain:		
Radius = $6 \cdot 10^{-5}$ m	Height = $9.13 \cdot 10^{-5}$ m	
Simulations [1] to [4]:		
$\Delta t_{\max} = 2.5 \cdot 10^{-6}$ s	Radial elements: 24	Axial elements: 49
Simulations [5] to [8]:		
$\Delta t_{\max} = 2.5 \cdot 10^{-6}$ s	Radial elements: 48	Axial elements: 97
Simulation [9]:		
$\Delta t_{\max,1} = 2.5 \cdot 10^{-6}$ s	$\Delta t_{\max,2} = 3.90625 \cdot 10^{-8}$ s	
Radial elements: 12	Axial elements: 25	
$L_{\max} = 2$	$K = 2$	$e_{\text{red}} = 97\%$

The results will be used to compare the breakup time and the shape at breakup. The breakup time is an indication for the speed of the dynamics and the breakup shape provides information on topological changes and small length scale phenomena. The results are compared to the results of two sharp interface models, specifically, McDroplet arbitrary Eulerian-Lagrangian model (Hazel, Heil, Schafer, & Bungartz, 2005; Li et al., 2020) and a Basilisk volume of fluid model (De Vita et al., n.d.). For the diffuse interface models, breakup is defined as the intersection of the $\phi = 0$ contour line with z -axis and for the sharp interface it is the intersection of the interface with the z -axis. The shape of breakup is the shape of the filament in the last time step before breakup, where the shape of the diffuse interface is given by the same $\phi = 0$ contour line. The moment of breakup is a linear interpolation in time of the last solution before breakup and the first solution after breakup.

The breakup shapes for different Cahn–Hilliard timescale and interfaces thickness are presented in Figure 6.1. The Cahn–Hilliard timescale is indicated by the color of the line and Figure 6.1a and 6.1b show the results for $\epsilon = 2 \cdot 10^{-6}$ m and $\epsilon = 10^{-6}$ m, respectively.

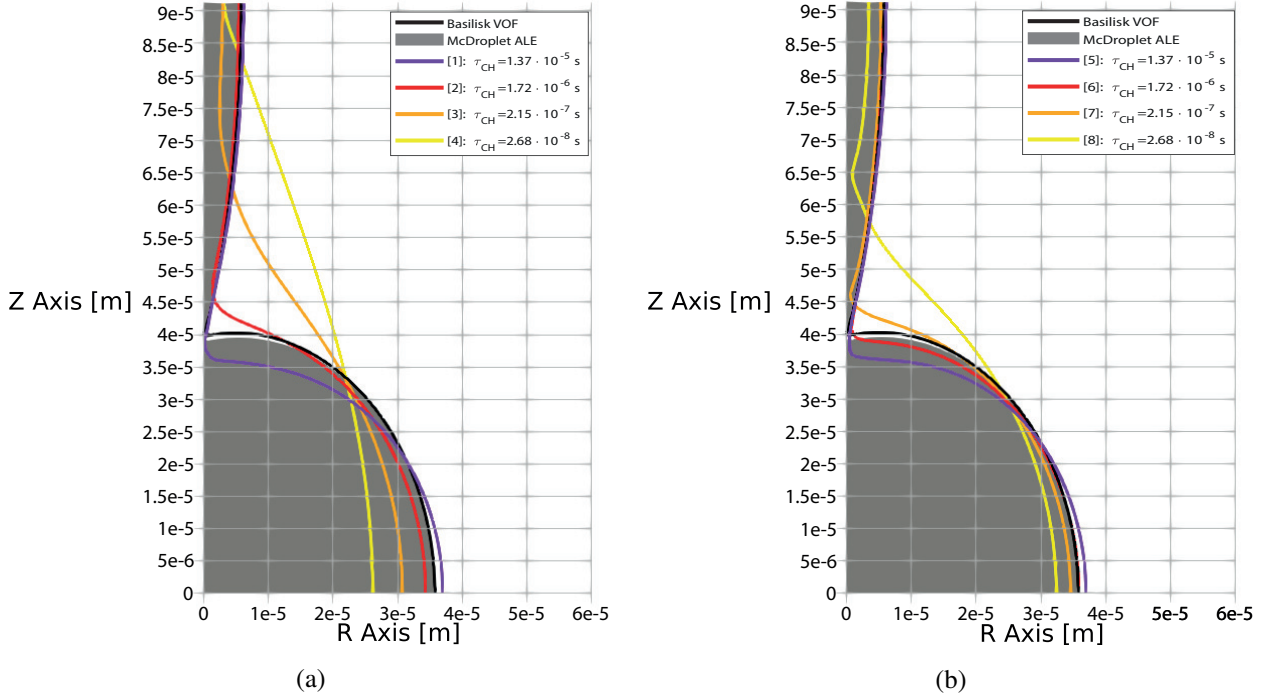


Figure 6.1: Plot of the interface shape at breakup for different Cahn–Hilliard timescale and interface thickness, for (a) $\epsilon = 2 \cdot 10^{-6}$ m and (b) $\epsilon = 10^{-6}$ m. The interface of the diffuse interface model is represented by the $\phi = 0$ contour line. The sharp interface is shown for Basilisk VOF reference simulation and the complete filament phase is shown for the McDroplet ALE reference simulation.

Figure 6.1 shows that the breakup shapes of the sharp interface reference simulations are essentially identical. The only difference is that the point of breakup is slightly higher for the data of the Basilisk simulation. In general, the breakup shapes of simulations [1], [2], [5], [6], and [7] are similar to the breakup shapes of the two reference simulations. The shape of a large sphere with a small elongated filament is also similar to the shape of the viscous filaments which succumb to Rayleigh breakup as presented in Figure 2.1. The interfaces form a small filament which will form a satellite droplet in the top of the domain and a larger droplet at the bottom of the domain. However, major differences can be found around the point of breakup and these differences are dependent on τ_{CH} and ϵ .

Comparing the results of simulations [1] through [4] in Figure 6.1a, it is shown that the shape of breakup is strongly dependent on the Cahn–Hilliard timescale. The point of breakup moves up for a decreasing τ_{CH} . For simulations [3] and [4] the point of breakup is the upper left corner. Therefore, no satellite droplet is formed. Simulations [5] through [8] show the same dependence on τ_{CH} , however the differences between the simulations are smaller. Simulation [8] forms a satellite droplet, however this droplet mixes with the ambient fluid, the phase mixing phenomenon is explained in Section 5.1.2. The results for the thinner interface appear to be less dependent on the Cahn–Hilliard timescale. From the other perspective, comparing simulations [1] and [5] to simulations [4] and [8], it can be observed that for a constant Cahn–Hilliard timescale the influence of the interface thickness increases with a decreasing τ_{CH} .

The results of simulations [2] and [6] correspond best to the sharp interface results. Figure 6.3 also shows the best correspondence for the breakup time of simulations [2] and [6] in comparison to the reference simulations. Therefore, $\tau_{CH} = 1.72 \cdot 10^{-6}$ s is used for simulation [9] with $\epsilon = 0.5 \cdot 10^{-6}$ m. The result for the breakup shape is shown in Figure 6.2. This figure shows the breakup shape for the 3 different interface thicknesses for $\tau_{CH} = 1.72 \cdot 10^{-6}$ s and the two sharp interface reference simulations.

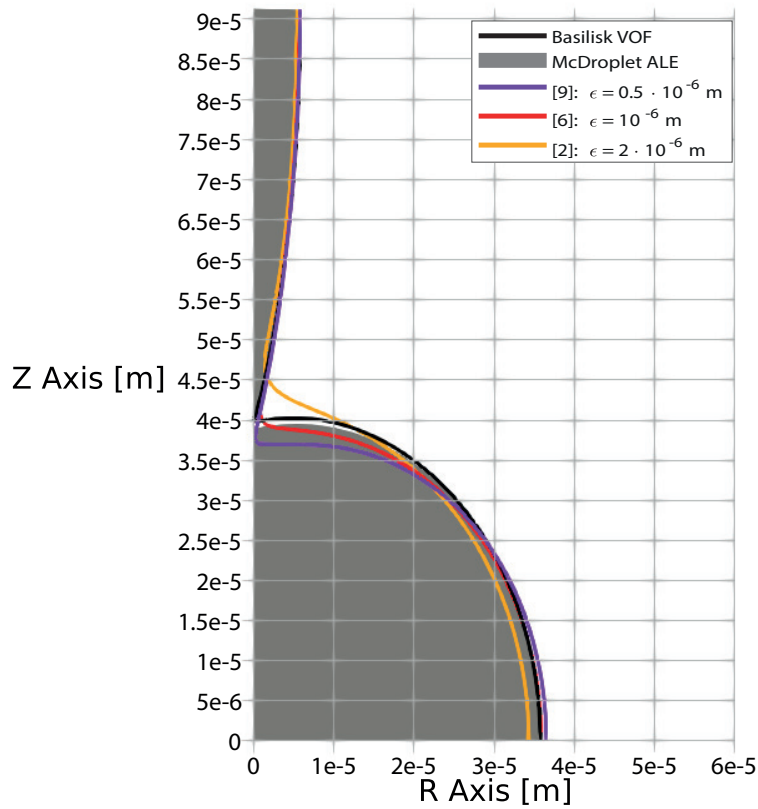


Figure 6.2: Plot of the interface shape at breakup for $\tau_{CH} = 1.72 \cdot 10^{-6}$ s and different interface thickness. The interface of the diffuse interface model is represented by the $\phi = 0$ contour line. The sharp interface is shown for Basilisk VOF reference simulation and the complete filament phase is shown for the McDroplet ALE reference simulation.

Figure 6.2 shows that the breakup shapes depend on the interface thickness. The height of breakup decreases for decreasing interface thickness. The difference between $\epsilon = 2 \cdot 10^{-6}$ m and $\epsilon = 10^{-6}$ m is larger than the difference between $\epsilon = 10^{-6}$ m and $\epsilon = 0.5 \cdot 10^{-6}$ m. This seems to resemble convergence of the results for decreasing interface thickness. However, this is only based on 3 simulations and must be interpreted carefully. The difference between the breakup shapes for $\epsilon = 10^{-6}$ m and $\epsilon = 0.5 \cdot 10^{-6}$ m is significant. The results have not converged for this interface thickness.

The result of simulation [6] with $\epsilon = 10^{-6}$ m corresponds better to reference simulations than the result of simulation [9] with $\epsilon = 0.5 \cdot 10^{-6}$ m. This suggests that the τ_{CH} with the best correspondence to the reference simulations is lower than $\tau_{\text{CH}} = 1.72 \cdot 10^{-6}$ for $\epsilon = 0.5 \cdot 10^{-6}$ m. The results with the best correspondence to the reference simulations for a decreasing interface thickness have a decreasing Cahn–Hilliard timescale.

The second important result of the simulations is the breakup time. Figure 6.3 shows the breakup time as a function of τ_{CH} . This figure also includes the sharp interface simulations and the theoretical breakup time from the derivation in Section 6.1.

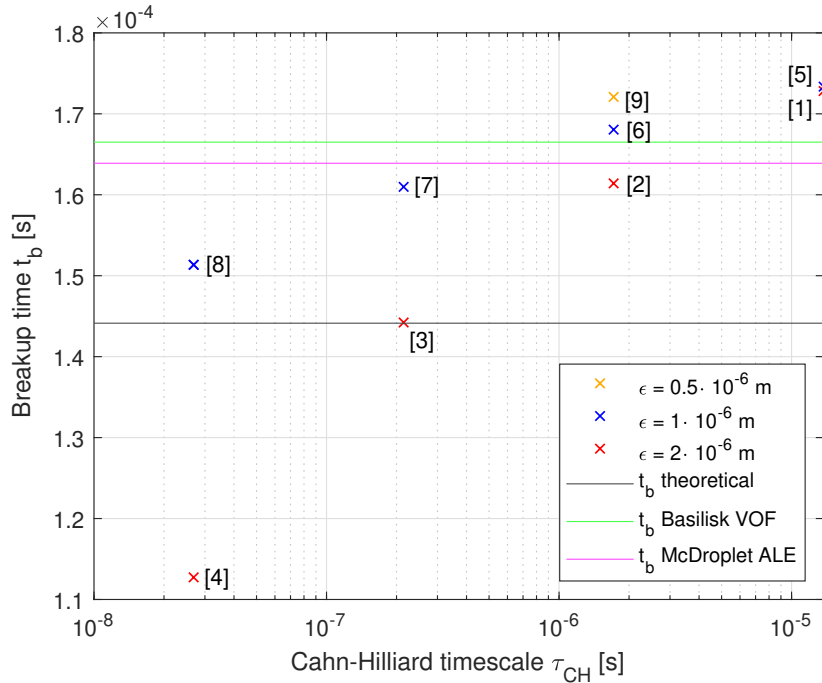


Figure 6.3: Plot of the breakup time as a function of the Cahn–Hilliard timescale. Additionally, this figure contains the breakup time of the reference simulations and the theoretical breakup time, which are both not a function of the Cahn–Hilliard time scale.

Figure 6.3 shows that the breakup time of the reference simulations is not equal. This can be a result of the small initial perturbation, $\delta = 0.01 \cdot r_0 = 2 \cdot 10^{-7}$ m. For the sharp interface reference models, the initial perturbation is only a few elements wide. This can result in inaccuracies for the initial perturbation which can result in a large change of breakup time due to the exponential growth of the perturbation. The theoretical breakup time is a result of the linear approximation and does not take into account any viscous or inertial effects of the ambient fluid (Driessen et al., 2013). Therefore, the theoretical breakup time is not correct, but can be used as a lower limit to the breakup time, since the inertial and viscous effect of the ambient medium will slow down the perturbation growth.

Figure 6.3 shows that results for the breakup time show the same pattern as the results for the breakup shape. The breakup time of the filament decreases with decreasing τ_{CH} . This is expected as a decreasing τ_{CH}

represents faster diffusion. This decrease is larger for larger interface thickness. The breakup time increases with decreasing interface thickness. This increase is larger for smaller τ_{CH} . A change in the model parameters has the most influence on the results for small τ_{CH} and large ϵ .

The breakup shapes of simulations [5] and [9] and simulations [2] and [7] are noticeably similar. Figure 6.3 shows that the breakup time of these cases are similar as well. Also simulation [1] shows a similar form of breakup and breakup time as simulations [5] and [9]. The breakup shapes for these sets of simulations are shown in Figure 6.4. However, the shape of breakup is not only dependent on the time of breakup, since the filaments have different shapes at the same moment in time. This indicates that the form of breakup and the breakup time are interdependent.

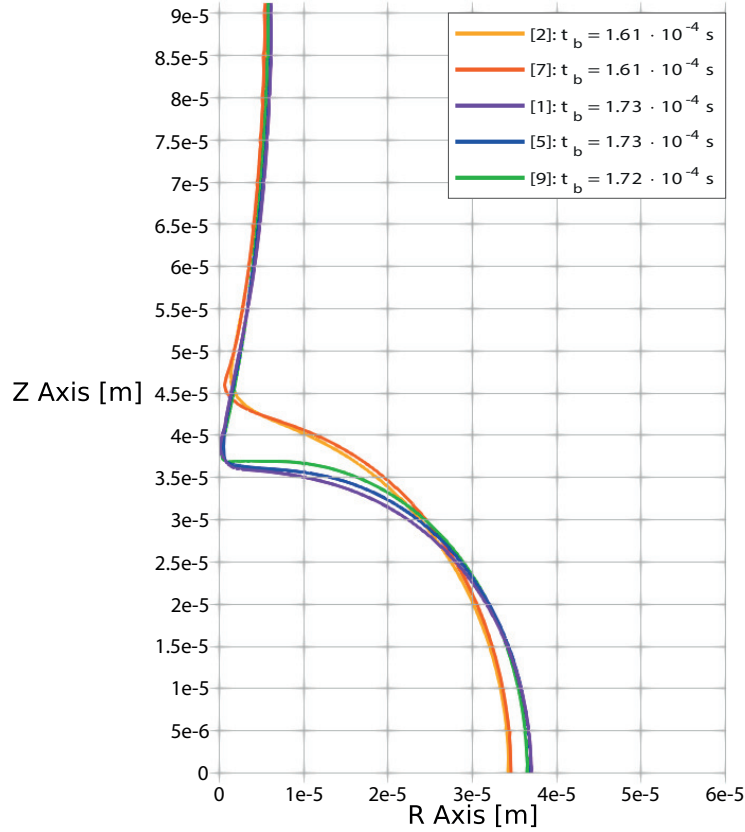


Figure 6.4: Plot of the interface shape at breakup for simulations with equal time of breakup. The interface of the diffuse interface model is represented by the $\phi = 0$ contour line.

For a constant Cahn–Hilliard timescale, the breakup time for a thick interface is smaller than for a thin interface. This is a result of the earlier conversion of interface energy to kinetic energy, as the phase gradient reaches the rotational axis earlier. The breakup time starts to converge for a decreasing interface thickness, as shown by simulations [2], [6], and [9]. The difference in breakup time between simulations [6] and [9] is 39% smaller than the difference between simulations [2] and [6]. However, the change in breakup time between [6] and [9] is still 2.4% of the breakup time of simulation [6].

Although the initial perturbation is only a few elements wide for sharp interface models, it is assumed that the correct breakup time is in between these 2 results. If the results for $\epsilon = 2 \cdot 10^{-6}$ m and $\epsilon = 10^{-6}$ m are interpolated, the lines would intersect the average of the sharp interface models for different τ_{CH} . Therefore, the value of τ_{CH} for which the breakup time corresponds best to the reference simulations is a function of ϵ . The τ_{CH} for best correspondence for breakup time, decreases for a decreasing interface thickness. This is the same relation found for the shape of breakup.

The results converge for decreasing interface thickness. Therefore, there appears to be asymptotic behavior for sufficiently thin interfaces. This asymptotic behavior can be represented by a single line in Figure 6.3 and is only dependent on the Cahn–Hilliard timescale. All results approach this line for sufficiently thin interfaces. For this asymptotic behavior there will be exactly one value for the Cahn–Hilliard timescale which corresponds best to the reference results. Simulations with this value for the Cahn–Hilliard timescale will have the same breakup time and thereby also breakup shape.

6.3 Conclusion

The numerical experiments showed that the simulations for the Rayleigh–Plateau instability case are more robust than the simulations for the filament contraction case. However, this did result in enlarged discretization errors due to the robustness based time step division. The filament breakup simulations are robust for the used range of interface thickness and mobility. As expected, the time step size decreased around the time of breakup. However, the simulations did not experience any robustness problems.

The numerical experiments showed that growth of a Rayleigh–Plateau instability on an infinitely long filament depends sensitively on the model parameters for the interface thickness and the mobility. It was observed that the shape of the filament at breakup and the time of breakup are interdependent; simulations with the same breakup time showed the same breakup shape.

The interface thickness influences the quantitative behavior of the simulation, and if the interface is sufficiently thick also the qualitative behavior. The interface thickness influenced whether or not a satellite droplet was formed after the breakup of the filament. In general, the interface thickness influenced both the shape of breakup, as well as the time of breakup. The interface thickness also influences the maximum velocity at breakup. The thinner interfaces showed higher velocities at the point and moment of breakup. The velocity at the point and moment of breakup is also strongly influenced by the time step size around breakup. This is expected because thinner interfaces and smaller time steps approach the point of singularity caused by breakup more accurately.

The shape of breakup and breakup time are influenced most by changes in τ_{CH} when ϵ is large. Thus, a change in the Cahn–Hilliard timescale is less influential on thin interfaces. The shape of breakup as well as the breakup time converge for decreasing ϵ at constant τ_{CH} . This suggests that the results converge for decreasing interface thickness. However, this conclusion must be interpreted with care since it is drawn from a small amount of data. The results for the simulated interface thicknesses do not converge to the results of the reference simulations based on sharp interface models. This can however be caused by ϵ not being sufficiently small or an incorrect value for τ_{CH} .

Both the shape at breakup and the breakup time change for different interface thickness and Cahn–Hilliard timescale. Decreasing the Cahn–Hilliard time scale decreases the breakup time. Therefore, increasing the mobility for a constant interface thickness speeds up the dynamics. The results for both the shape of breakup as well as the breakup time show that a change in interface thickness or Cahn–Hilliard timescale has the most influence for small Cahn–Hilliard timescales and large interface thickness. Increasing the interface thickness also decreases the breakup time.

If the results converge for decreasing interface thickness, than there is asymptotic behavior for sufficiently thin interfaces. The influence of the model parameters for this asymptotic behavior is completely governed by the Cahn–Hilliard timescale. There will be one optimal value for which the results correspond best to reference simulations. However, performing the simulations for this study is outside the time-frame of this research. Within the simulated cases, the optimal value for the Cahn–Hilliard timescale for best correspondence to the reference simulations, is a function of the interface thickness. Therefore, it is not yet possible to pinpoint the optimal value for the Cahn–Hilliard timescale for the asymptotic behavior.

7 Conclusion and Recommendation

In this section conclusions are formulated with respect to the goal of this research and the research questions are answered. Afterward, recommendations for future work are given and model improvements are suggested.

7.1 Conclusion

This research is performed to answer the main question: what is the influence of the model parameters, namely the interface thickness parameter ϵ and the mobility parameter m , on the filament dynamics? It was expected that the results converge to a sharp interface limit for sufficiently thin interfaces: do the results for decreasing interface thickness converge to a sharp interface limit? Do these results correspond to those of a sharp interface model? However, computational expense often limits the interface thickness and it is interesting to investigate the influence of this: what is the influence of the diffuse interface on small length scale phenomena? This research is done by numerical experiments. Therefore, we investigate whether the numerical implementation can simulate the filament dynamics in a robust manner.

The numerical experiments showed that the simulations for the more viscous filament in the Rayleigh-Plateau instability case were more robust than the simulations for the filament contraction case. This is indicated by the higher Oh of the infinitely long filament. The singularity at the point and moment of breakup does not impose any difficulties for the solution process. Therefore, it can be concluded that the numerical implementation of the NSCH model can simulate filament dynamics in a robust manner. The robustness is however dependent on the specific case.

The two numerical test cases showed several small length scale phenomena. The most evident is the interface itself. The Cahn–Hilliard timescale shows that the diffusion process, which is for example needed for interface equilibration, is dependent on the mobility parameter and the interface thickness. Other small length scale phenomena are the necking at breakup and the satellite droplet originating from breakup. The satellite droplet was not always created for a large interface thickness, while it disappeared for high mobility due to diffusive phase mixing. For a case with a sufficiently thin interface and low mobility, the satellite droplet was created and displayed oscillations due to deformation. Thus, small length scale phenomena are represented best with a small interface thickness. The phase mixing can be prevented by decreasing the interface thickness. This confirms that thin interfaces are most favorable for small length scale phenomena.

The numerical results show convergence for decreasing interface thickness, as shown by the Rayleigh-Plateau instability case. However, this is based on a small amount of data and the breakup shape and breakup time were not fully converged within the tested parameter regime. The results were compared to two sharp interface reference simulations. Certain combinations of the model parameters produced results similar to the reference simulations. However, within the tested parameter regime there was no convergence to the reference simulations.

The main research targeted the influence of the model parameters on the filament dynamics. Conclusions will be drawn on the influence of the interface thickness, the mobility and the two combined.

As already discussed, the interface thickness is the limiting factor for small length scale phenomena. For example, a thin interface is needed for the creation and preservation of a satellite droplet. The interface thickness also influences the breakup shape and breakup time, such that decreasing the interface thickness increases the breakup time. This influence converges for decreasing interface thickness.

The mobility parameter has a complex influence on the filament dynamics. First of all, it speeds up the diffusive processes. Phase mixing quickens and the breakup time in the Rayleigh-Plateau instability case decreases for increasing mobility. For high values of the mobility the phase mixing decreased a filament significantly in size. Increasing the mobility also decreases the diffuse Cahn–Hilliard timescale, which is the

governing timescale for the equilibration of the interface. Low values of the mobility resulted in difficulties for equilibration in and around the interface. This limits the mobility from below.

If the results converge for decreasing interface thickness, then there is asymptotic behavior for sufficiently thin interfaces. The influence of the model parameters for this asymptotic behavior is completely governed by the Cahn–Hilliard timescale. There will be one optimal value for which the results correspond best to reference simulations.

High velocity phenomena occurred for simulations with high mobility. This, for now, limits the mobility from above. It was investigated if these phenomena are a result of temporal or numerical discretization. The time steps were decreased by the robustness based time step division. However, this did not inhibit this phenomenon. Decreasing the element size did not prevent this phenomenon from occurring.

The mobility and interface thickness have influence on the impact of changes in the other model parameter. The results for both the shape of breakup as well as the breakup time show that a change in interface thickness or Cahn–Hilliard timescale has the most influence for small Cahn–Hilliard timescales and large interface thickness. However, the parameter regime for the Rayleigh–Plateau instability case needs to be expanded to be able to completely understand the influence of the mobility parameter and the interface thickness.

7.2 Recommendation

The first part of the recommendation consists of improvements to the numerical model. Specifically, to the refinements of the spatial and temporal discretization.

An important limiting factor to the numerical experiments is the computation time. Especially for simulations that use refinements. The SEMR method uses two solutions to estimate the elements with the largest error contribution. A residual based error estimation uses only one solution to estimate the error contribution of elements (Melenk & Wohlmuth, 2001). To reduce the computation time of the refinement procedure and thereby the simulation, it is advised to implement the residual based error estimation in the numerical model.

The second improvement is an accuracy based addition to the time step refinement. The current time step refinement is only based on the robustness of the model. This creates the possibility that a robust model uses large time steps which result in temporal discretization errors, as shown in the Rayleigh breakup case. It was needed to implement a threshold for the phase field. This threshold was altered several times because the time step size decreased drastically. Specifically, in cases with varying timescales it is needed to have an adaptive time step size. For robust models, this only works if the time step refinements is accuracy based. Therefore, the time step refinement procedure needs additional accuracy based conditions.

The following recommendation concerns future work. This advise is based on observations and results from the numerical experiments.

As already mentioned, the conclusion on convergence for decreasing interface thickness is based on a small amount of experiments. It is advised to continue the study for a larger parameter regime; thinner interfaces and more values for the Cahn–Hilliard timescale within the range used for this research. The most important goal is to find the asymptotic behavior for sufficiently thin interfaces. From this result it should be possible to find a value for the Cahn–Hilliard timescale to which the results are similar to the reference simulations. This is needed to complete the systematic study of the model parameters.

The second research proposition elaborates on the systematic study of the model parameters. If this study is completed, the influence is only known for one specific case. It is needed to figure out to what extent this knowledge applies to other cases. For example, other filaments with different Oh that succumb to a different breakup mode. In general it is needed to study other applications of this model to find the general applicability.

The third proposal is researching the high velocity flow phenomena which occur for high mobility values. Are the phenomena part of the model solution or a discretization error? The time step size was reduced during the simulation and an additional simulation was performed with a finer mesh. However, this did not influence the high velocities. The phenomena occurred for simulations where the Cahn–Hilliard timescale is decreased significantly while the time step size is not decreased. Does the time step size need to be scaled with respect to the Cahn–Hilliard timescale? These high velocity flow phenomena need to be prevented to be able to simulate Cahn–Hilliard timescales which are lower than the range used in this research.

References

- Abels, H., Garcke, H., & Grün, G. (2012). Thermodynamically consistent, frame indifferent diffuse interface models for incompressible two-phase flows with different densities. *Mathematical Models and Methods in Applied Sciences*, 22(3). doi: 10.1142/S0218202511500138
- Anthony, C. R., Kamat, P. M., Harris, M. T., & Basaran, O. A. (2019). Dynamics of contracting filaments. *Physical Review Fluids*, 4(9), 93601. Retrieved from <https://doi.org/10.1103/PhysRevFluids.4.093601> doi: 10.1103/PhysRevFluids.4.093601
- De Vita, F., Fullana, J.-M., Kirstetter, G., Lagrée, P.-Y., Lane, E., Lopez-Herrera, J., ... Van Hooft, A. (n.d.). *Basilisk*. Retrieved from <http://basilisk.fr/>
- Driessen, T., Jeurissen, R., Wijshoff, H., Toschi, F., & Lohse, D. (2013). Stability of viscous long liquid filaments. *Physics of Fluids*, 25(6). doi: 10.1063/1.4811849
- Eggers, J., & Villermaux, E. (2008). Physics of liquid jets. *Reports on Progress in Physics*, 71(3). doi: 10.1088/0034-4885/71/3/036601
- Hazel, A. L., Heil, M., Schafer, M., & Bungartz, H.-J. (2005). *omph-lib – An Object-Oriented Multi-Physics Finite-Element Library*. Springer Nature. Retrieved from [https://www.research.manchester.ac.uk/portal/en/publications/omphlib--an-objectoriented-multiphysics-finiteelement-library\(1369664e-5bf6-4b28-8bcc-035da157f5c6\)/export.html](https://www.research.manchester.ac.uk/portal/en/publications/omphlib--an-objectoriented-multiphysics-finiteelement-library(1369664e-5bf6-4b28-8bcc-035da157f5c6)/export.html)
- Layton, W. (2008). *Introduction to the Numerical Analysis of Incompressible Viscous Flows*. doi: 10.1137/1.9780898718904
- Li, Y., Diddens, C., Segers, T., Wijshoff, H., Versluis, M., & Lohse, D. (2020, 7). Evaporating droplets on oil-wetted surfaces: Suppression of the coffee-stain effect. *Proceedings of the National Academy of Sciences of the United States of America*, 117(29), 16756–16763. doi: 10.1073/pnas.2006153117
- Melenk, J. M., & Wohlmuth, B. I. (2001). *On residual-based a posteriori error estimation in hp-FEM* (Vol. 15; Tech. Rep.).
- Notz, P. K., & Basaran, O. A. (2004). Dynamics and breakup of a contracting liquid filament. *Journal of Fluid Mechanics*, 512, 223–256. doi: 10.1017/S0022112004009759
- Notz, P. K., Chen, A. U., & Basaran, O. A. (2001). Satellite drops: Unexpected dynamics and change of scaling during pinch-off. *Physics of Fluids*, 13(3), 549–551. doi: 10.1063/1.1343906
- Plateau, J. (1873). *Statique expérimentale et théorique des liquides soumis aux seules forces moléculaires*. Ghent: Gauthier-Villars.
- Rayleigh, L. (1892, 8). XIX. On the instability of cylindrical fluid surfaces. *The London, Edinburgh, and Dublin Philosophical Magazine and Journal of Science*, 34(207), 177–180. Retrieved from <https://www.tandfonline.com/doi/abs/10.1080/14786449208620304> doi: 10.1080/14786449208620304
- Schulkes, R. M. (1996). The contraction of liquid filaments. *Journal of Fluid Mechanics*, 309, 277–300. doi: 10.1017/S0022112096001632
- Simsek, G., & van Brummelen, H. (2017). *Numerical Methods for Diffuse Interface Models of Binary Flows* (No. 2017). Retrieved from <http://arxiv.org/abs/1603.06475>
- Sun, Y., & Beckermann, C. (2007, 1). Sharp interface tracking using the phase-field equation. *Journal of Computational Physics*, 220(2), 626–653. doi: 10.1016/j.jcp.2006.05.025
- Teigen, K., & Munkejord, S. (2009, 4). Sharp-interface simulations of drop deformation in electric fields. *IEEE Transactions on Dielectrics and Electrical Insulation*, 16(2), 475–482. doi: 10.1109/TDEI.2009.4815181
- Tomotika, S. (1935). On the Instability of a Cylindrical Thread of a Viscous Liquid Surrounded by Another Viscous Fluid. *Proceedings of the Royal Society of London. Series A, Mathematical and Physical Sciences*, 150, 322–337. Retrieved from https://www.jstor.org/stable/96387?origin=ads&seq=14#metadata_info_tab_contents
- Van Brummelen, E. H., Demont, T. H., & van Zwieten, G. J. (2020). An adaptive isogeometric analysis approach to elasto-capillary fluid-solid interaction. *International Journal for Numerical Methods in Engineering*(March), 1–22. doi: 10.1002/nme.6388

- Van der Waals, J. (1893). *THE THERMODYNAMIC THEORY OF CAPILLARITY UNDER THE HYPOTHESIS OF A CONTINUOUS VARIATION OF DENSITY* (Tech. Rep.).
- Van Zwieten, G., Van Zwieten, J., Verhoosel, C., Fonn, E., Van Opstal, T., & Hoitinga, W. (2020). *Nutils (Version 6.1)*. Retrieved from <http://doi.org/10.5281/zenodo.3949893>
- Wijshoff, H. (2010, 6). *The dynamics of the piezo inkjet printhead operation* (Vol. 491) (No. 4-5). North-Holland. doi: 10.1016/j.physrep.2010.03.003
- Yang, X., Feng, J. J., Liu, C., & Shen, J. (2006). Numerical simulations of jet pinching-off and drop formation using an energetic variational phase-field method. *Journal of Computational Physics*, 218(1), 417–428. doi: 10.1016/j.jcp.2006.02.021

A Model derivation

This appendix contains additional detail to the derivation of the model presented in Section 3.1

A.1 Mass balance

The mass balance as shown in Equation 3.4 will be derived from a general mass balance. The general mass balance for species i is:

$$\frac{\partial \tilde{\rho}_i}{\partial t} + \nabla \cdot (\tilde{\rho}_i \mathbf{u}_i) = \gamma_i, \quad (\text{A.1})$$

where $\tilde{\rho}_i$ is the partial mass density, \mathbf{u}_i is the velocity and γ_i is the volumetric mass source term.

Assuming no supply or consumption of mass for any species by for example a chemical reaction, the mass balance simplifies to:

$$\frac{\partial \tilde{\rho}_i}{\partial t} + \nabla \cdot (\tilde{\rho}_i \mathbf{u}_i) = 0. \quad (\text{A.2})$$

The partial mass density $\tilde{\rho}_i$ can be expressed as a multiplication of the constant species density ρ_i and the volume fraction ϕ_i . All species densities are assumed constant, which results in incompressible constituent. This is used to further simplify the equation into:

$$\rho_i \left(\frac{\partial \phi_i}{\partial t} + \nabla \cdot (\phi_i \mathbf{u}_i) \right) = 0, \quad (\text{A.3})$$

and further into:

$$\frac{\partial \phi_i}{\partial t} + \nabla \cdot (\phi_i \mathbf{u}_i) = 0. \quad (\text{A.4})$$

The mass balance of the complete systems is found by a summation of all individual species (Simsek & van Brummelen, 2017). This results in the system mass balance:

$$\sum_{i=1}^{n_{\text{species}}} \left(\frac{\partial \phi_i}{\partial t} + \nabla \cdot (\phi_i \mathbf{u}_i) \right) = 0, \quad (\text{A.5})$$

which can be rewritten to:

$$\frac{\partial}{\partial t} \left(\sum_{i=1}^{n_{\text{species}}} \phi_i \right) + \nabla \cdot \left(\sum_{i=1}^{n_{\text{species}}} \phi_i \mathbf{u}_i \right) = 0. \quad (\text{A.6})$$

The summation of the volume fractions ϕ_i is always equal to 1 under the incompressibility assumption. $\mathbf{u} := \sum_{i=1}^{n_{\text{species}}} \phi_i \mathbf{u}_i$ is the volume averaged velocity field. This results in:

$$\frac{\partial}{\partial t} (1) + \nabla \cdot (\mathbf{u}) = 0, \quad (\text{A.7})$$

which is simplified to:

$$\nabla \cdot \mathbf{u} = 0. \quad (\text{A.8})$$

This is the solenoidal volume averaged velocity field which is based on incompressible fluids.

A.2 Momentum balance

The same derivation will be done for the momentum balance in Equation 3.4. The general momentum balance for fluid i is

$$\frac{\partial (\tilde{\rho}_i \mathbf{u}_i)}{\partial t} + \nabla \cdot (\tilde{\rho}_i \mathbf{u}_i \otimes \mathbf{u}_i) = \nabla \cdot \mathbf{T}_i + \tilde{\rho}_i \mathbf{b}_i + \boldsymbol{\pi}_i + \mathbf{u}_i \gamma_i, \quad (\text{A.9})$$

where \mathbf{T}_i is a stress tensor, \mathbf{b}_i are the external body forces, $\boldsymbol{\pi}_i$ is the momentum supplied by other fluids and $\mathbf{u}_i \gamma_i$ results from the volumetric mass source term.

The mixture momentum balance results from a summation over all mixture components (Simsek & van Brummelen, 2017):

$$\sum_{i=1}^{n_{\text{species}}} \frac{\partial(\tilde{\rho}_i \mathbf{u}_i)}{\partial t} + \sum_{i=1}^{n_{\text{species}}} \nabla \cdot (\tilde{\rho}_i \mathbf{u}_i \otimes \mathbf{u}_i) = \sum_{i=1}^{n_{\text{species}}} (\nabla \cdot \mathbf{T}_i + \tilde{\rho}_i \mathbf{b}_i + \boldsymbol{\pi}_i + \mathbf{u}_i \gamma_i). \quad (\text{A.10})$$

The total exchange of momentum between the species is zero, $\sum_{i=1}^{n_{\text{species}}} (\boldsymbol{\pi}_i + \mathbf{u}_i \gamma_i) = 0$ (Simsek & van Brummelen, 2017). Assuming no gravitational influence, the fluid stress consists from a viscous component, $\boldsymbol{\tau}$, a capillary component, $\boldsymbol{\zeta}$, and an isotropic component $p\mathbf{I}$ (Van Brummelen et al., 2020). This reduces the momentum balance to:

$$\sum_{i=1}^{n_{\text{species}}} \frac{\partial(\tilde{\rho}_i \mathbf{u}_i)}{\partial t} + \sum_{i=1}^{n_{\text{species}}} \nabla \cdot (\tilde{\rho}_i \mathbf{u}_i \otimes \mathbf{u}_i) = \nabla \cdot \boldsymbol{\tau} + \nabla \cdot \boldsymbol{\zeta} - \nabla p. \quad (\text{A.11})$$

The partial time-derivative in Equation A.11 can be simplified as

$$\sum_{i=1}^{n_{\text{species}}} \frac{\partial(\tilde{\rho}_i \mathbf{u}_i)}{\partial t} = \sum_{i=1}^{n_{\text{species}}} \frac{\partial(\tilde{\rho}_i (\mathbf{u} + \mathbf{w}_i))}{\partial t} = \frac{\partial(\rho \mathbf{u} + \mathbf{J})}{\partial t} = \frac{\partial \rho \mathbf{u}}{\partial t} + \frac{\partial \mathbf{J}}{\partial t}, \quad (\text{A.12})$$

where \mathbf{J} is a mass flux relative to the flow direction:

$$\mathbf{J} := \sum_{i=1}^{n_{\text{species}}} (\rho_i \phi_i \mathbf{w}_i) = \sum_{i=1}^{n_{\text{species}}} (\tilde{\rho}_i \mathbf{w}_i). \quad (\text{A.13})$$

\mathbf{w}_i is the diffusion velocity of component i for the volume averaged velocity field. Specifically, $\mathbf{u}_i = \mathbf{u} + \mathbf{w}_i$, the component velocity is equal to the sum of the volume averaged velocity field and the diffusion velocity of the same component. The summation of the divergence of the flow of momentum for all species can be elaborated as:

$$\begin{aligned} \sum_{i=1}^{n_{\text{species}}} \nabla \cdot (\tilde{\rho}_i \mathbf{u}_i \otimes \mathbf{u}_i) &= \sum_{i=1}^{n_{\text{species}}} \nabla \cdot (\tilde{\rho}_i (\mathbf{w}_i + \mathbf{u}) \otimes (\mathbf{w}_i + \mathbf{u})) \\ &= \sum_{i=1}^{n_{\text{species}}} \nabla \cdot (\tilde{\rho}_i \mathbf{u} \otimes \mathbf{u}) + \sum_{i=1}^{n_{\text{species}}} \nabla \cdot (\tilde{\rho}_i \mathbf{w}_i \otimes \mathbf{u}) \\ &\quad + \sum_{i=1}^{n_{\text{species}}} \nabla \cdot (\mathbf{u} \otimes \tilde{\rho}_i \mathbf{w}_i) + \sum_{i=1}^{n_{\text{species}}} \nabla \cdot (\tilde{\rho}_i \mathbf{w}_i \otimes \mathbf{w}_i) \\ &= \nabla \cdot (\rho \mathbf{u} \otimes \mathbf{u}) + \nabla \cdot (\mathbf{J} \otimes \mathbf{u}) + \\ &\quad \nabla \cdot (\mathbf{u} \otimes \mathbf{J}) + \sum_{i=1}^{n_{\text{species}}} \nabla \cdot (\tilde{\rho}_i \mathbf{w}_i \otimes \mathbf{w}_i). \end{aligned} \quad (\text{A.14})$$

Implementing both of these elaborations in the mixture momentum balance results in:

$$\frac{\partial \rho \mathbf{u}}{\partial t} + \frac{\partial \mathbf{J}}{\partial t} + \nabla \cdot (\rho \mathbf{u} \otimes \mathbf{u}) + \nabla \cdot (\mathbf{J} \otimes \mathbf{u}) + \nabla \cdot (\mathbf{u} \otimes \mathbf{J}) + \sum_{i=1}^{n_{\text{species}}} \nabla \cdot (\tilde{\rho}_i \mathbf{w}_i \otimes \mathbf{w}_i) = \nabla \cdot \boldsymbol{\tau} + \nabla \cdot \boldsymbol{\zeta} - \nabla p, \quad (\text{A.15})$$

which is reordered to:

$$\frac{\partial \rho \mathbf{u}}{\partial t} + \nabla \cdot (\rho \mathbf{u} \otimes \mathbf{u}) + \nabla \cdot (\mathbf{u} \otimes \mathbf{J}) + \frac{\partial \mathbf{J}}{\partial t} + \nabla \cdot (\mathbf{J} \otimes \mathbf{u}) = \nabla \cdot \boldsymbol{\tau} + \nabla \cdot \boldsymbol{\zeta} - \nabla p - \sum_{i=1}^{n_{\text{species}}} \nabla \cdot (\tilde{\rho}_i \mathbf{w}_i \otimes \mathbf{w}_i). \quad (\text{A.16})$$

Equation A.16 can be rewritten using the following identity, $\nabla \cdot (\mathbf{p} \otimes \mathbf{q}) = (\nabla \cdot \mathbf{q})\mathbf{p} + \mathbf{q} \cdot \nabla \mathbf{p}$ (Simsek & van Brummelen, 2017):

$$\begin{aligned} \frac{\partial \rho \mathbf{u}}{\partial t} + \nabla \cdot (\rho \mathbf{u} \otimes \mathbf{u}) + \nabla \cdot (\mathbf{u} \otimes \mathbf{J}) + \frac{\partial \mathbf{J}}{\partial t} + \mathbf{u} \cdot \nabla \mathbf{J} + (\nabla \cdot \mathbf{u}) \mathbf{J} = \\ \nabla \cdot \boldsymbol{\tau} + \nabla \cdot \boldsymbol{\zeta} - \nabla p - \sum_{i=1}^{n_{\text{species}}} \nabla \cdot (\tilde{\rho}_i \mathbf{w}_i \otimes \mathbf{w}_i). \end{aligned} \quad (\text{A.17})$$

This contains the material derivative for the mass flux. Implementing the mass balance from Equation A.8, results in:

$$\frac{\partial \rho \mathbf{u}}{\partial t} + \nabla \cdot (\rho \mathbf{u} \otimes \mathbf{u}) + \nabla \cdot (\mathbf{u} \otimes \mathbf{J}) + \frac{D\mathbf{J}}{Dt} = \nabla \cdot \boldsymbol{\tau} + \nabla \cdot \boldsymbol{\zeta} - \nabla p - \sum_{i=1}^{n_{\text{species}}} \nabla \cdot (\tilde{\rho}_i \mathbf{w}_i \otimes \mathbf{w}_i). \quad (\text{A.18})$$

The material derivative of the mass flux is assumed to be zero (Abels et al., 2012; Simsek & van Brummelen, 2017). Therefore the mixture momentum balance reduces to:

$$\frac{\partial \rho \mathbf{u}}{\partial t} + \nabla \cdot (\rho \mathbf{u} \otimes \mathbf{u}) + \nabla \cdot (\mathbf{u} \otimes \mathbf{J}) = \nabla \cdot \boldsymbol{\tau} + \nabla \cdot \boldsymbol{\zeta} - \nabla p - \sum_{i=1}^{n_{\text{species}}} \nabla \cdot (\tilde{\rho}_i \mathbf{w}_i \otimes \mathbf{w}_i). \quad (\text{A.19})$$

The total exchange of momentum by diffusing species in the mixture is zero due to intrinsic conservation of momentum. The final expression for the momentum becomes: A.20.

$$\frac{\partial \rho \mathbf{u}}{\partial t} + \nabla \cdot (\rho \mathbf{u} \otimes \mathbf{u}) + \nabla \cdot (\mathbf{u} \otimes \mathbf{J}) = \nabla \cdot \boldsymbol{\tau} + \nabla \cdot \boldsymbol{\zeta} - \nabla p. \quad (\text{A.20})$$

A.3 Solution space

Solutions to the NSCH model applied to the slender jet approach for filament contraction are bound by the trial and test spaces. The quantities of interest are in the trial space and the corresponding weighing functions, as defined in Appendix A.4, are in the test space. The trial and test spaces of the problem are the same because Dirichlet components of the boundary conditions are all homogeneous.

$$\begin{aligned} U &= \{ \mathbf{u} : \Omega \rightarrow \mathbb{R}^3 \mid \mathbf{u} \in \mathbf{H}^1(\Omega) \mid \mathbf{u}_{\mathbf{n}} = 0 \text{ on } \Gamma_{\text{Ambient}} \ \& \ \Gamma_{\text{Symmetry plane}} \} \\ P &= \{ p : \Omega \rightarrow \mathbb{R} \mid p \in L^2(\Omega) \} \\ \Phi &= \{ \phi : \Omega \rightarrow \mathbb{R} \mid \phi \in H^1(\Omega) \} \\ M &= \{ \mu : \Omega \rightarrow \mathbb{R} \mid \mu \in H^1(\Omega) \} \end{aligned} \quad (\text{A.21})$$

The spatial discretization uses basis functions N , which are polynomial basis functions for which the orders are defined in Section 4.2. The finite approximations of the trial and test functions are defined as a summation over the basis functions multiplied by the nodal values:

$$\begin{aligned} \tilde{\mathbf{u}}(\mathbf{x}, t) &= \sum_{k=1}^{n_u} \mathbf{u}_k(t) N_k^u(\mathbf{x}), & \tilde{\mathbf{y}}(\mathbf{x}, t) &= \sum_{k=1}^{n_u} \mathbf{y}_k(t) N_k^u(\mathbf{x}), \\ \tilde{p}(\mathbf{x}, t) &= \sum_{k=1}^{n_p} p_k(t) N_k^p(\mathbf{x}), & \tilde{q}(\mathbf{x}, t) &= \sum_{k=1}^{n_p} q_k(t) N_k^p(\mathbf{x}), \\ \tilde{\phi}(\mathbf{x}, t) &= \sum_{k=1}^{n_\phi} \phi_k(t) N_k^\phi(\mathbf{x}), & \tilde{\lambda}(\mathbf{x}, t) &= \sum_{k=1}^{n_\phi} \lambda_k(t) N_k^\phi(\mathbf{x}), \\ \tilde{\mu}(\mathbf{x}, t) &= \sum_{k=1}^{n_\mu} \mu_k(t) N_k^\mu(\mathbf{x}), & \tilde{w}(\mathbf{x}, t) &= \sum_{k=1}^{n_\mu} w_k(t) N_k^\mu(\mathbf{x}). \end{aligned} \quad (\text{A.22})$$

A.4 Weak formulation

Solutions to the NSCH model are contained within the combined trial space,

$\mathcal{S} = \{\mathbf{u} \in \mathbf{U}, p \in P, \phi \in \Phi, \mu \in M\}$. The combined test space is defined as $\mathcal{V} := (\mathbf{y}, q, \lambda, w) \in \mathcal{S}$ and contains the weighing functions needed to construct the weighted residual formulation.

A.4.1 Mass balance weak formulation

The mass balance is given as:

$$\operatorname{div} \mathbf{u} = 0. \quad (\text{A.23})$$

Multiplying by the weighing function q and integrating over the domain results in the weighted residual formulation:

$$\int_{\Omega} q (\nabla \cdot \mathbf{u}) d\Omega = 0. \quad (\text{A.24})$$

Applying the spatial discretization results in:

$$\int_{\Omega} \tilde{q} (\nabla \cdot \tilde{\mathbf{u}}) d\Omega = 0. \quad (\text{A.25})$$

Implementing the definition for the discrete test function from Equation (A.22) and reordering the equation results in:

$$\sum_{k=1}^{n_p} q_k(t) \int_{\Omega} N_k^p(\mathbf{x}) (\nabla \cdot \tilde{\mathbf{u}}) d\Omega = 0. \quad (\text{A.26})$$

This equation must hold for all test functions and thereby for all values of $q_k(t)$. Therefore, it possible to simplify the equation to the spatially discretized residual formulation:

$$\int_{\Omega} N^p (\nabla \cdot \tilde{\mathbf{u}}) d\Omega = 0. \quad (\text{A.27})$$

Here, $N^p = \sum_{k=1}^{n_p} N_k^p$ is the summation of all basis functions for the pressure. Note that the indication of the dependency on the spatial coordinates are dropped for clarity reasons.

A.4.2 Momentum balance weak formulation

The momentum balance is given as:

$$\frac{\partial(\rho\mathbf{u})}{\partial t} + \nabla \cdot (\rho\mathbf{u} \otimes \mathbf{u}) + \nabla \cdot (\mathbf{u} \otimes \mathbf{J}) + \nabla p - \nabla \cdot \boldsymbol{\tau} - \nabla \cdot \boldsymbol{\zeta} = 0, \quad (\text{A.28})$$

which can be simplified to:

$$\frac{\partial(\rho\mathbf{u})}{\partial t} + \nabla \cdot (\rho\mathbf{u} \otimes \mathbf{u}) + \nabla \cdot (\mathbf{u} \otimes \mathbf{J}) + \nabla \cdot \mathbf{T} = 0. \quad (\text{A.29})$$

Where $\mathbf{T} = p\mathbf{I} - \boldsymbol{\tau} - \boldsymbol{\zeta}$ is the stress tensor. This tensor is symmetric because the pressure component, viscous stress tensor and the capillary component are all symmetric. The viscous stress and capillary component are defined in Equations 3.7 and 3.9, respectively.

Multiplying by the weighing function \mathbf{y} and integrating over the domain results in the weighted residual formulation:

$$\frac{d}{dt} \int_{\Omega} (\rho\mathbf{y} \cdot \mathbf{u}) d\Omega + \int_{\Omega} \mathbf{y} \cdot \nabla \cdot (\rho\mathbf{u} \otimes \mathbf{u}) d\Omega + \int_{\Omega} \mathbf{y} \cdot \nabla \cdot (\mathbf{u} \otimes \mathbf{J}) d\Omega + \int_{\Omega} \mathbf{y} \cdot (\nabla \cdot \mathbf{T}) d\Omega = 0. \quad (\text{A.30})$$

Applying the partial integration:

$$\mathbf{y} \cdot (\nabla \cdot \mathbf{T}) = \nabla \cdot (\mathbf{T} \cdot \mathbf{y}) - \mathbf{T}^T : \nabla \mathbf{y}, \quad (\text{A.31})$$

and Gauss's divergence theorem, results in the weak formulation of the momentum balance:

$$\begin{aligned} \frac{d}{dt} \int_{\Omega} (\rho \mathbf{y} \cdot \mathbf{u}) d\Omega + \int_{\Omega} \mathbf{y} \cdot \nabla \cdot (\rho \mathbf{u} \otimes \mathbf{u}) d\Omega + \int_{\Omega} \mathbf{y} \cdot \nabla \cdot (\mathbf{u} \otimes \mathbf{J}) d\Omega - \int_{\Omega} \mathbf{T}^T : \nabla \mathbf{y} d\Omega \\ = - \int_{\Gamma} (\mathbf{T} \cdot \mathbf{y}) \cdot \mathbf{n} d\Gamma. \end{aligned} \quad (\text{A.32})$$

Applying the symmetry of the traction tensor results in:

$$\begin{aligned} \frac{d}{dt} \int_{\Omega} (\rho \mathbf{y} \cdot \mathbf{u}) d\Omega + \int_{\Omega} \mathbf{y} \cdot \nabla \cdot (\rho \mathbf{u} \otimes \mathbf{u}) d\Omega + \int_{\Omega} \mathbf{y} \cdot \nabla \cdot (\mathbf{u} \otimes \mathbf{J}) d\Omega - \int_{\Omega} \mathbf{T} : \nabla \mathbf{y} d\Omega \\ = - \int_{\Gamma} \mathbf{T}_n \cdot \mathbf{y} d\Gamma, \end{aligned} \quad (\text{A.33})$$

where the right hand side can be reduced as follows:

$$\int_{\Gamma} \mathbf{T}_n \cdot \mathbf{y} d\Gamma = \int_{\Gamma} \mathbf{T}_n^n \cdot \mathbf{y}_n d\Gamma + \int_{\Gamma} \mathbf{T}_n^t \cdot \mathbf{y}_t = \int_{\Gamma} \mathbf{T}_n^n \cdot \mathbf{0} d\Gamma + \int_{\Gamma} \mathbf{0} \cdot \mathbf{y}_t d\Gamma = 0. \quad (\text{A.34})$$

The simplification starts by a division in a tangential and normal direction, using the perpendicularity of these direction together in combination with the inner product. The normal component of the test function, \mathbf{y}_n , is equal to the zero-vector as defined by the test space, because there is a Dirichlet boundary condition on the velocity. The tangential component of the stress on the boundary is zero due to the free slip condition. This results in the weak formulation for the momentum balance:

$$\frac{d}{dt} \int_{\Omega} (\rho \mathbf{y} \cdot \mathbf{u}) d\Omega + \int_{\Omega} \mathbf{y} \cdot \nabla \cdot (\rho \mathbf{u} \otimes \mathbf{u}) d\Omega + \int_{\Omega} \mathbf{y} \cdot \nabla \cdot (\mathbf{u} \otimes \mathbf{J}) d\Omega - \int_{\Omega} \mathbf{T} : \nabla \mathbf{y} d\Omega = 0. \quad (\text{A.35})$$

Applying the spatial discretization results in:

$$\frac{d}{dt} \int_{\Omega} (\rho \tilde{\mathbf{y}} \cdot \tilde{\mathbf{u}}) d\Omega + \int_{\Omega} \tilde{\mathbf{y}} \cdot \nabla \cdot (\rho \tilde{\mathbf{u}} \otimes \tilde{\mathbf{u}}) d\Omega + \int_{\Omega} \tilde{\mathbf{y}} \cdot \nabla \cdot (\tilde{\mathbf{u}} \otimes \tilde{\mathbf{J}}) d\Omega - \int_{\Omega} \tilde{\mathbf{T}} : \nabla \tilde{\mathbf{y}} d\Omega = 0. \quad (\text{A.36})$$

Implementing the definition for the discrete test function from Equation (A.22) and reordering the equation results in:

$$\begin{aligned} \sum_{k=1}^{n_u} \mathbf{y}_k(t) \left(\frac{d}{dt} \int_{\Omega} (\rho N^u \cdot \tilde{\mathbf{u}}) d\Omega + \int_{\Omega} N^u \cdot \nabla \cdot (\rho \tilde{\mathbf{u}} \otimes \tilde{\mathbf{u}}) d\Omega \right. \\ \left. + \int_{\Omega} N^u \cdot \nabla \cdot (\tilde{\mathbf{u}} \otimes \tilde{\mathbf{J}}) d\Omega - \int_{\Omega} \tilde{\mathbf{T}} : \nabla N^u d\Omega \right) = 0. \end{aligned} \quad (\text{A.37})$$

This equation must hold for all test functions and thereby for all values of $\mathbf{y}_k(t)$. Therefore, it possible to simplify the equation to the spatially discretized residual formulation:

$$\frac{d}{dt} \int_{\Omega} (\rho N^u \cdot \tilde{\mathbf{u}}) d\Omega + \int_{\Omega} N^u \cdot \nabla \cdot (\rho \tilde{\mathbf{u}} \otimes \tilde{\mathbf{u}}) d\Omega + \int_{\Omega} N^u \cdot \nabla \cdot (\tilde{\mathbf{u}} \otimes \tilde{\mathbf{J}}) d\Omega - \int_{\Omega} \tilde{\mathbf{T}} : \nabla N^u d\Omega = 0. \quad (\text{A.38})$$

Here, $N^u = \sum_{k=1}^{n_u} N_k^u$ is the summation of all basis functions for the velocity.

A.4.3 Chemical potential weak formulation

The strong formulation of the governing equation for the chemical potential is:

$$\frac{\partial \phi}{\partial t} + \nabla \cdot (\phi \mathbf{u} - m \nabla \mu) = 0. \quad (\text{A.39})$$

Multiplying this equation by the weighing function w and integrating over the domain results in the weighted residual formulation:

$$\frac{d}{dt} \int_{\Omega} w \phi d\Omega + \int_{\Omega} w \nabla \cdot (\phi \mathbf{u} - m \nabla \mu) d\Omega = 0. \quad (\text{A.40})$$

In which the terms within the integral can be separated:

$$\frac{d}{dt} \int_{\Omega} w\phi d\Omega + \int_{\Omega} w\nabla \cdot (\phi\mathbf{u}) d\Omega - \int_{\Omega} w\nabla \cdot (m\nabla\mu) d\Omega = 0. \quad (\text{A.41})$$

Applying the partial integrations:

$$\begin{aligned} w\nabla \cdot (\phi\mathbf{u}) &= w\nabla\phi \cdot \mathbf{u} + w\phi\nabla \cdot \mathbf{u}, \\ -w\nabla \cdot (m\nabla\mu) &= \nabla w \cdot m\nabla\mu - \nabla \cdot (wm\nabla\mu), \end{aligned} \quad (\text{A.42})$$

together with a divergence free flow field, results in:

$$\frac{d}{dt} \int_{\Omega} w\phi d\Omega + \int_{\Omega} w\nabla\phi \cdot \mathbf{u} d\Omega + \int_{\Omega} (\nabla w \cdot m\nabla\mu - \nabla \cdot (wm\nabla\mu)) d\Omega = 0. \quad (\text{A.43})$$

Finally applying Gauss's divergence theorem results in the weak formulation:

$$\frac{d}{dt} \int_{\Omega} w\phi d\Omega + \int_{\Omega} w\nabla\phi \cdot \mathbf{u} d\Omega + \int_{\Omega} \nabla w \cdot m\nabla\mu d\Omega = \int_{\Gamma} (wm\nabla\mu) \cdot \mathbf{n} d\Gamma. \quad (\text{A.44})$$

The boundary conditions of the outer boundaries as defined in Section 3.2 can be implemented on the right hand side of Equation A.44. The boundary integral only evaluates the outer boundaries and not the axisymmetric axis. Therefore the complete boundary integral can be evaluated in the following way:

$$\int_{\Gamma} (wm\nabla\mu) \cdot \mathbf{n} d\Gamma = \int_{\Gamma} (wm\partial_n\mu) d\Gamma = 0. \quad (\text{A.45})$$

The normal derivative of the chemical potential is zero on all boundaries for both the filament contraction case as well as the Rayleigh-Plateau instability case.

Applying the spatial discretization results in:

$$\frac{d}{dt} \int_{\Omega} \tilde{w}\tilde{\phi} d\Omega + \int_{\Omega} \tilde{w}\nabla\tilde{\phi} \cdot \tilde{\mathbf{u}} d\Omega + \int_{\Omega} \nabla\tilde{w} \cdot m\nabla\tilde{\mu} d\Omega = 0. \quad (\text{A.46})$$

Implementing the definition for the discrete test function from Equation A.22 and reordering the equation results in:

$$\sum_{k=1}^{n_{\mu}} w_k(t) \left(\frac{d}{dt} \int_{\Omega} N_k^{\mu} \tilde{\phi} d\Omega + \int_{\Omega} N_k^{\mu} \nabla\tilde{\phi} \cdot \tilde{\mathbf{u}} d\Omega + \int_{\Omega} \nabla N_k^{\mu} \cdot m\nabla\tilde{\mu} d\Omega \right) = 0. \quad (\text{A.47})$$

This equation must hold for all test functions and thereby for all values of $w_k(t)$. Therefore it is possible to simplify the equation to the spatially discretized residual formulation:

$$\frac{d}{dt} \int_{\Omega} N^{\mu} \tilde{\phi} d\Omega + \int_{\Omega} N^{\mu} \nabla\tilde{\phi} \cdot \tilde{\mathbf{u}} d\Omega + \int_{\Omega} \nabla N^{\mu} \cdot m\nabla\tilde{\mu} d\Omega = 0. \quad (\text{A.48})$$

Here, $N^{\mu} = \sum_{k=1}^{n_{\mu}} N_k^{\mu}$ is the summation of all basis functions for the chemical potential.

A.4.4 Phase field weak formulation

The governing equation for the phase field is given as:

$$\mu + \epsilon\sigma\Delta\phi - \frac{\sigma}{\epsilon}\Psi' = 0. \quad (\text{A.49})$$

Multiplying by weighing function λ and integrating over the domain results in:

$$\int_{\Omega} \lambda\mu d\Omega + \int_{\Omega} \lambda(\epsilon\sigma\Delta\phi) d\Omega - \int_{\Omega} \lambda\frac{\sigma}{\epsilon}\Psi' d\Omega = 0. \quad (\text{A.50})$$

Applying the partial integration:

$$\lambda \Delta \phi = \nabla \cdot (\lambda \nabla \phi) - \nabla \lambda \cdot \nabla \phi, \quad (\text{A.51})$$

and Gauss's divergence theorem results in the weak formulation:

$$\int_{\Omega} \lambda \mu d\Omega - \int_{\Omega} (\epsilon \sigma \nabla \lambda \cdot \nabla \phi) d\Omega - \int_{\Omega} \lambda \frac{\sigma}{\epsilon} \Psi' d\Omega = - \int_{\Gamma} (\epsilon \sigma \lambda \nabla \phi) \cdot \mathbf{n} d\Gamma. \quad (\text{A.52})$$

Using the boundary conditions from Subsection 3.2, the right hand side can be reduced as follows:

$$- \int_{\Gamma} (\epsilon \sigma \lambda \nabla \phi) \cdot \mathbf{n} d\Gamma = - \int_{\Gamma} (\epsilon \sigma \lambda \partial_{\mathbf{n}} \phi) d\Gamma = 0. \quad (\text{A.53})$$

Applying the spatial discretization results in:

$$\int_{\Omega} \tilde{\lambda} \tilde{\mu} d\Omega - \int_{\Omega} (\epsilon \sigma \nabla \tilde{\lambda} \cdot \nabla \tilde{\phi}) d\Omega - \int_{\Omega} \tilde{\lambda} \frac{\sigma}{\epsilon} \tilde{\Psi}' d\Omega = 0. \quad (\text{A.54})$$

Implementing the definition for the discrete test function from (A.22) and reordering the equation results in:

$$\sum_{k=1}^{n_{\phi}} \lambda_k(t) \left(\int_{\Omega} N_k^{\phi} \tilde{\mu} d\Omega - \int_{\Omega} (\epsilon \sigma \nabla N_k^{\phi} \cdot \nabla \tilde{\phi}) d\Omega - \int_{\Omega} N_k^{\phi} \frac{\sigma}{\epsilon} \tilde{\Psi}' d\Omega \right) = 0. \quad (\text{A.55})$$

This equation must hold for all test functions and thereby for all values of $\lambda_k(t)$. Therefore it is possible to simplify the equation to the spatially discretized residual formulation:

$$\int_{\Omega} N^{\phi} \tilde{\mu} d\Omega - \int_{\Omega} (\epsilon \sigma \nabla N^{\phi} \cdot \nabla \tilde{\phi}) d\Omega - \int_{\Omega} N^{\phi} \frac{\sigma}{\epsilon} \tilde{\Psi}' d\Omega = 0. \quad (\text{A.56})$$

Here, $N^{\phi} = \sum_{k=1}^{n_{\phi}} N_k^{\phi}(\mathbf{x})$ is the summation of all basis function for the phase field.

A.5 Temporal discretization and model implementation

After formulating the spatial discretization, the next step is applying the time discretization schemes and formulating the model implementation. The implementation in Nutils uses the Einstein notation, therefore, all equations need to be converted into this notation. The following sections elaborate on the time discretized residual formulation. This is used to calculate the solution on time step $t + 1$ and the solution on time step t is already calculated.

A.5.1 Temporal discretization mass balance

The spatial discretized residual form of the mass balance, as shown in Equation (A.27), is converted to Einstein notation and discretized in time. This results in the following equation:

$$\int_{\Omega} N^p d_{-i}(v_{-i}^{t+1}) d\Omega = 0. \quad (\text{A.57})$$

This expression is similar for both the Backward Euler scheme and the Crank–Nicolson scheme.

A.5.2 Temporal discretization momentum balance

The residual form of the momentum balance, as shown in Equation (A.38), is converted to Einstein notation and discretized in time afterward. After the conversion to Einstein notation the formulation is changed to a skew symmetric formulation (Layton, 2008). This formulation prevents energy production in the model due to a inexact divergence free field in the Taylor–Hood approximation (Van Brummelen et al., 2020). The Einstein notation is as follows:

$$\int_{\Omega} N^u \cdot \nabla \cdot (\rho \tilde{\mathbf{u}} \otimes \tilde{\mathbf{u}}) d\Omega = \int_{\Omega} N^u d_{-j}(\rho w_{-j} u_{-i}) d\Omega. \quad (\text{A.58})$$

Note that one of the velocity variables is substituted by w_{-j} . Applying the product rule two times results in:

$$\begin{aligned}
&= \int_{\Omega} d_{-j}(w_{-j} N^{\mathbf{u}} \rho u_{-i}) d\Omega - \int_{\Omega} w_{-j} \rho u_{-i} d_{-j}(N^{\mathbf{u}}) d\Omega = \\
&= \int_{\Omega} d_{-j}(w_{-j} N^{\mathbf{u}} \rho u_{-i}) d\Omega - \int_{\Omega} u_{-i} d_{-j}(w_{-j} \rho N^{\mathbf{u}}) d\Omega + \int_{\Omega} u_{-i} N^{\mathbf{u}} d_{-j}(w_{-j} \rho) d\Omega.
\end{aligned} \tag{A.59}$$

Again, applying the product rule to both the second and third term results in:

$$\begin{aligned}
&= \int_{\Omega} d_{-j}(w_{-j} N^{\mathbf{u}} \rho u_{-i}) d\Omega - \int_{\Omega} d_{-j}(w_{-j} \rho N^{\mathbf{u}} u_{-i}) d\Omega + \int_{\Omega} w_{-j} \rho N^{\mathbf{u}} d_{-j}(u_{-i}) d\Omega \\
&+ \int_{\Omega} u_{-i} N^{\mathbf{u}} \rho d_{-j}(w_{-j}) d\Omega + \int_{\Omega} u_{-i} N^{\mathbf{u}} w_{-j} d_{-j}(\rho) d\Omega.
\end{aligned} \tag{A.60}$$

Two terms cancel and implementing the divergence free velocity field, $d_{-j} w_{-j} = 0$ results in:

$$= \int_{\Omega} w_{-j} \rho N^{\mathbf{u}} d_{-j}(u_{-i}) d\Omega + \int_{\Omega} u_{-i} N^{\mathbf{u}} w_{-j} d_{-j}(\rho) d\Omega. \tag{A.61}$$

Finally, this term is a combination of half of the first part of Equation (A.59) and half of Equation (A.61):

$$\begin{aligned}
&\int_{\Omega} N^{\mathbf{u}} d_{-j}(\rho w_{-j} u_{-i}) d\Omega = \frac{1}{2} \int_{\Omega} d_{-j}(w_{-j} N^{\mathbf{u}} \rho u_{-i}) d\Omega - \frac{1}{2} \int_{\Omega} w_{-j} \rho u_{-i} d_{-j}(N^{\mathbf{u}}) d\Omega \\
&+ \frac{1}{2} \int_{\Omega} w_{-j} \rho N^{\mathbf{u}} d_{-j}(u_{-i}) d\Omega + \frac{1}{2} \int_{\Omega} u_{-i} N^{\mathbf{u}} w_{-j} d_{-j}(\rho) d\Omega
\end{aligned} \tag{A.62}$$

Using this elaboration of the second term of the residual form it possible to define the time discretized equations. Note that u_{-j} is substituted for w_{-j} . The fully implicit equation for the momentum balance for the Backward Euler time discretization scheme becomes:

$$\begin{aligned}
&\int_{\Omega} y_{-i} \frac{\rho^{t+1} v_{-i}^{t+1} - \rho^t v_{-i}^t}{\Delta t} d\Omega + \frac{1}{2} \int_{\Omega} d_{-j}(u_{-j}^{t+1} N^{\mathbf{u}} \rho^{t+1} u_{-i}^{t+1}) d\Omega \\
&- \frac{1}{2} \int_{\Omega} u_{-j}^{t+1} \rho^{t+1} u_{-i}^{t+1} d_{-j}(N^{\mathbf{u}}) d\Omega + \frac{1}{2} \int_{\Omega} u_{-j}^{t+1} \rho^{t+1} N^{\mathbf{u}} d_{-j}(u_{-i}^{t+1}) d\Omega \\
&+ \frac{1}{2} \int_{\Omega} u_{-i}^{t+1} N^{\mathbf{u}} u_{-j}^{t+1} d_{-j}(\rho^{t+1}) d\Omega + \int_{\Omega} N^{\mathbf{u}} d_j(u_{-j}^{t+1} J_{-i}^{t+1}) d\Omega \\
&- \int_{\Omega} d_{-j}(N^{\mathbf{u}}) T_{-i} j^{t+1} d\Omega = 0.
\end{aligned} \tag{A.63}$$

The Crank–Nicolson scheme is a semi-implicit scheme. Therefore, the time discretized equation is dependent on the current solution and the next solution. The time discretized equation for the momentum balance for the Crank–Nicolson scheme is:

$$\begin{aligned}
&\int_{\Omega} y_{-i} \frac{\rho^{t+1} v_{-i}^{t+1} - \rho^t v_{-i}^t}{\Delta t} d\Omega + \frac{1}{2} \left(\frac{1}{2} \int_{\Omega} d_{-j}(u_{-j}^{t+1} N^{\mathbf{u}} \rho^{t+1} u_{-i}^{t+1}) d\Omega \right. \\
&- \frac{1}{2} \int_{\Omega} u_{-j}^{t+1} \rho^{t+1} u_{-i}^{t+1} d_{-j}(N^{\mathbf{u}}) d\Omega + \frac{1}{2} \int_{\Omega} u_{-j}^{t+1} \rho^{t+1} N^{\mathbf{u}} d_{-j}(u_{-i}^{t+1}) d\Omega \\
&+ \frac{1}{2} \int_{\Omega} u_{-i}^{t+1} N^{\mathbf{u}} u_{-j}^{t+1} d_{-j}(\rho^{t+1}) d\Omega + \int_{\Omega} N^{\mathbf{u}} d_j(u_{-j}^{t+1} J_{-i}^{t+1}) d\Omega \\
&- \left. \int_{\Omega} d_{-j}(N^{\mathbf{u}}) T_{-i} j^{t+1} d\Omega \right) + \frac{1}{2} \left(\frac{1}{2} \int_{\Omega} d_{-j}(u_{-j}^t N^{\mathbf{u}} \rho^t u_{-i}^t) d\Omega \right. \\
&- \frac{1}{2} \int_{\Omega} u_{-j}^t \rho^t u_{-i}^t d_{-j}(N^{\mathbf{u}}) d\Omega + \frac{1}{2} \int_{\Omega} u_{-j}^t \rho^t N^{\mathbf{u}} d_{-j}(u_{-i}^t) d\Omega \\
&+ \frac{1}{2} \int_{\Omega} u_{-i}^t N^{\mathbf{u}} u_{-j}^t d_{-j}(\rho^t) d\Omega + \int_{\Omega} N^{\mathbf{u}} d_j(u_{-j}^t J_{-i}^t) d\Omega \\
&- \left. \int_{\Omega} d_{-j}(N^{\mathbf{u}}) T_{-i} j^t d\Omega \right) = 0.
\end{aligned} \tag{A.64}$$

A.5.3 Temporal discretization chemical potential

The residual form of the weak formulation for the chemical potential is given in Equation (A.48). This equation is converted into Einstein notation and discretized in time. For the Backward Euler scheme this becomes:

$$\int_{\Omega} \frac{N^{\mu} (\phi^{t+1} - \phi^t)}{\Delta t} d\Omega + \int_{\Omega} N^{\mu} d_{\cdot i}(\phi^{t+1}) u_i^{t+1} d\Omega + \int_{\Omega} d_{\cdot i}(N^{\mu}) m d_{\cdot i}(\mu^{t+1}) d\Omega = 0, \quad (\text{A.65})$$

and for the Crank–Nicolson scheme this becomes:

$$\begin{aligned} & \int_{\Omega} \frac{N^{\mu} (\phi^{t+1} - \phi^t)}{\Delta t} d\Omega + \frac{1}{2} \left(\int_{\Omega} N^{\mu} d_{\cdot i}(\phi^{t+1}) u_i^{t+1} d\Omega + \int_{\Omega} d_{\cdot i}(N^{\mu}) m d_{\cdot i}(\mu^{t+1}) d\Omega \right) \\ & + \frac{1}{2} \left(\int_{\Omega} N^{\mu} d_{\cdot i}(\phi^t) u_i^t d\Omega + \int_{\Omega} d_{\cdot i}(N^{\mu}) m d_{\cdot i}(\mu^t) d\Omega \right) = 0. \end{aligned} \quad (\text{A.66})$$

A.5.4 Temporal discretization phase field

The residual form of the weak formulation for the phase field is given in Equation (A.56). This equation can be used to substituted the chemical potential in the equation for the chemical potential. To not differ from the semi-implicit scheme, the time discretized for both schemes is defined as:

$$\int_{\Omega} N^{\phi} \mu^{t+1} d\Omega - \int_{\Omega} d_{\cdot i}(N^{\phi}) \sigma \epsilon d_{\cdot i}(\mu^{t+1}) d\Omega - \int_{\Omega} N^{\phi} \frac{\sigma}{\epsilon} \Psi' d\Omega = 0. \quad (\text{A.67})$$

Here, Ψ' is a function of ϕ^{t+1} .

B Interface expansion simulations

This appendix contains information on the domain, boundary conditions and initial conditions of the interface expansion simulations. Afterward, some additional results are presented.

B.1 Simulation domain

The domains of the interface expansion problems are different from the filament contraction problem. This section elaborates on the domain and boundary conditions of this problem.

The interface expansion problem with the straight boundary has a 2 dimensional domain with 2 different types of boundaries, as shown in Figure B.1. The upper and lower boundary are symmetry boundary conditions, similar to the symmetry planes described in Section 3.2. There is no dependency on the height for either the boundary conditions or the initial conditions. Thus, this problem is effectively a one dimensional problem. The left and right boundary assume a fully developed flow with a free flow condition. Therefore, the stress on the interface is zero and the normal derivatives of the phase field and chemical potential are also zero.

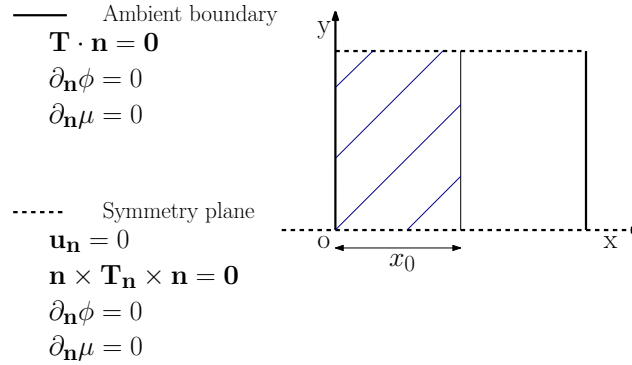


Figure B.1: Domain and boundary conditions for the interface expansion simulation with a straight interface. The drawn interface is the $\phi = 0$ contour line.

The fluids are initially at rest and the interface is a quarter of the equilibrium width. The interface is located in the middle of the domain. The initial conditions are defined as:

$$\begin{aligned} \mathbf{u}(\mathbf{x}, 0) &= \mathbf{0}, \\ \phi(\mathbf{x}, 0) &= \tanh\left(\frac{x_0 - x}{\sqrt{2}\epsilon_0}\right). \end{aligned} \quad (\text{B.1})$$

Where the characteristics correspond to Table 5.3.

The interface expansion problem with the curved interface has only one boundary, the ambient boundary. This boundary is assumed to be far enough from the interface that the flow is developed. Therefore the normal derivatives of the phase field and chemical potential are zero. There is no outflow over the boundary and there is a free slip condition. The model is axisymmetric and uses the numerical implementation as defined in Section 4.1, however without the height coordinate. This problem is effectively a one dimensional problem because of the axisymmetry. Figure B.2 shows these boundary conditions and the domain.

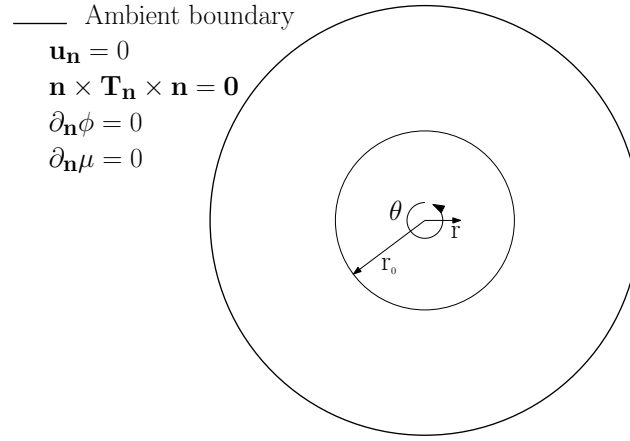


Figure B.2: Domain and boundary conditions for the interface expansion simulation with a curved interface. The drawn interface is the $\phi = 0$ contour line.

The fluids are initially at rest and the interface is a quarter of the equilibrium width. The initial conditions are defined as:

$$\begin{aligned} \mathbf{u}(\mathbf{x}, 0) &= \mathbf{0}, \\ \phi(\mathbf{x}, 0) &= \tanh\left(\frac{r_0 - r}{\sqrt{2}\epsilon_0}\right). \end{aligned} \quad (\text{B.2})$$

Where the characteristics correspond to Table 5.3.

B.2 Curved interface

Figure B.3 shows the velocity field for the curved interface. These results show the same details as the velocity field of the straight interface. There are velocity fluctuations around the interface and also further into the lighter and less viscous phase, which is situated at larger radii than the interface radius. The velocity fluctuations increase in magnitude with decreasing mobility.

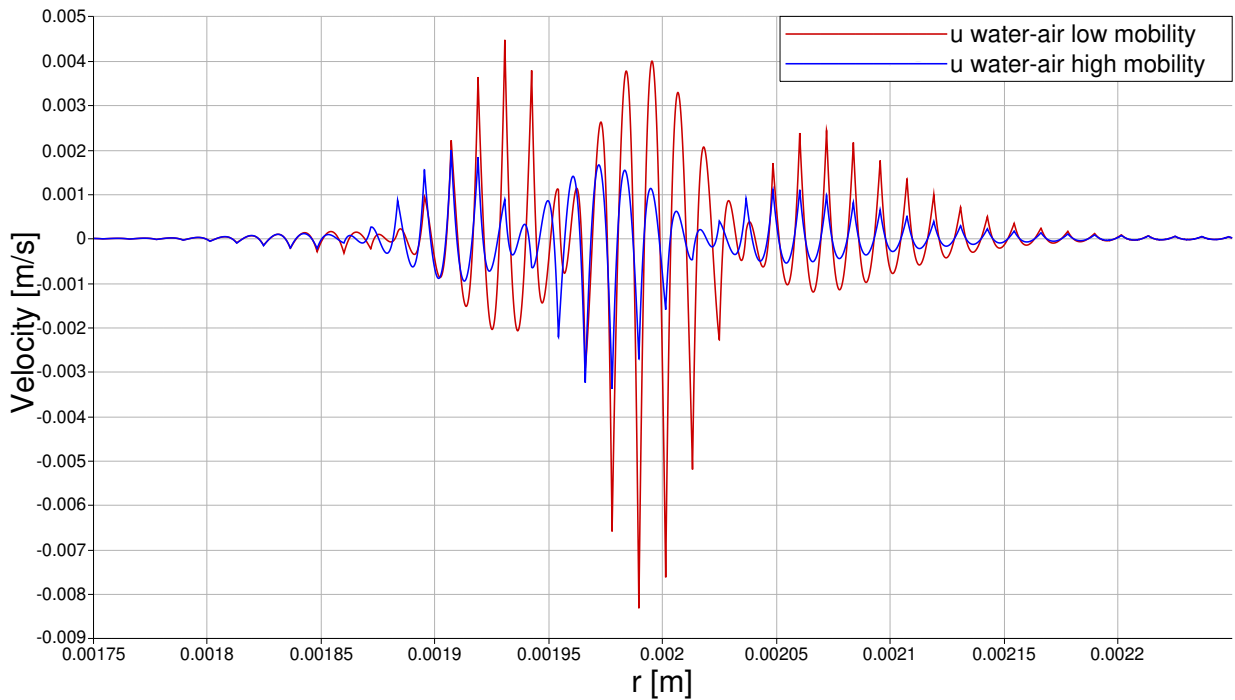


Figure B.3: Velocity field for the curved water-air interface for 2 different mobilities. For the high mobility at $t = 0.125$ ms and the low mobility at $t = 1.25$ ms. The interface is situated around $r = 0.00196$ m.

The phase fields for the curved interface are identical at the same dimensionless time, $t^* = t/\tau_{CH}$, as explained in Section 5.2.5. This confirms that the Cahn–Hilliard timescale is also the governing timescale for interface expansion of a curved interface.

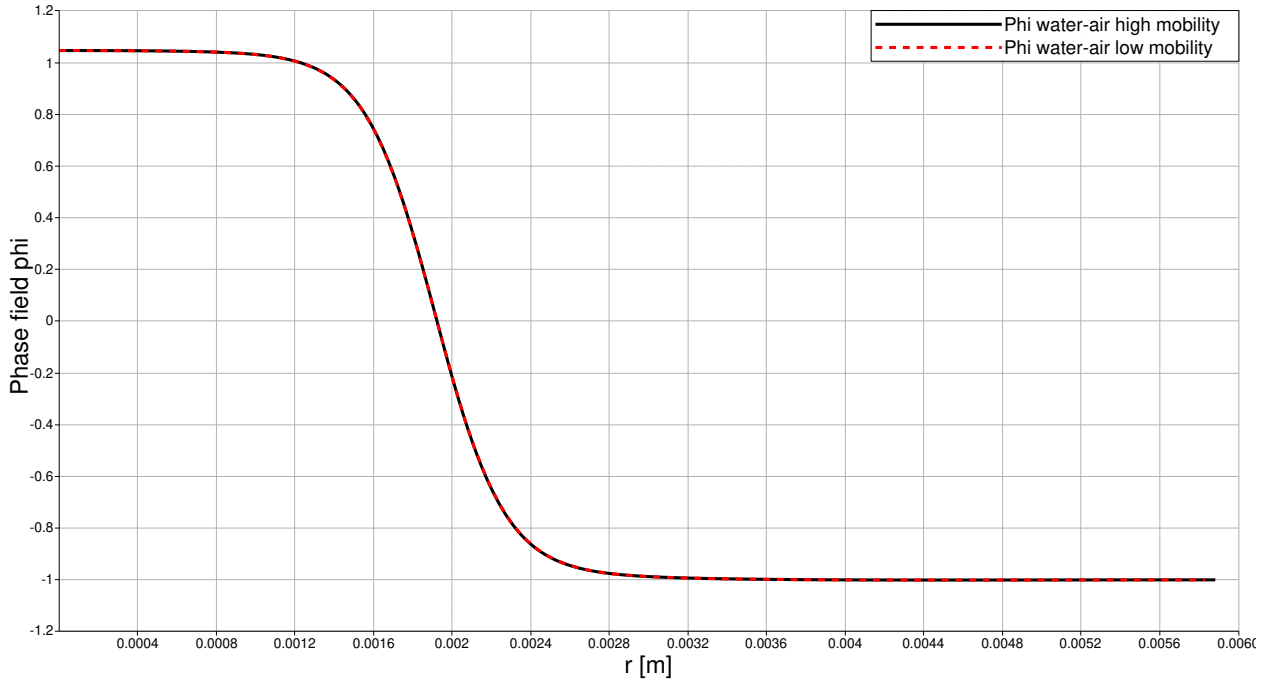


Figure B.4: Phase field for the curved interface for 2 different mobilities. For the high mobility at $t = 3.625$ ms and for the low mobility at $t = 36.25$ ms

B.3 Coarse mesh interface

Figure B.5 shows velocity field and phase field on a 2D simulation with a coarse grid. This figure shows a large velocity fluctuation while the phase field is smooth. The largest velocity fluctuation is found in the air phase far away from the interface. This figure also shows the larger distance between the velocity peaks in comparison to Figures 5.8 and 5.10.

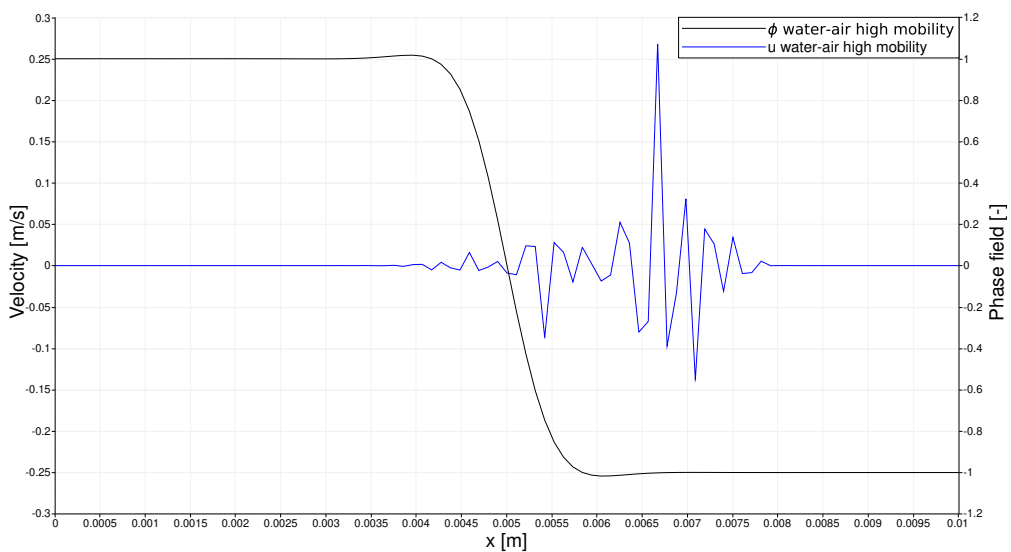


Figure B.5: Velocity field and phase field for a straight water-air interface and the high mobility at $t = 1.25$ ms. The results are from a simulation with third order base function and the coarsest mesh as indicated in Figure 5.7

Declaration concerning the TU/e Code of Scientific Conduct for the Master's thesis

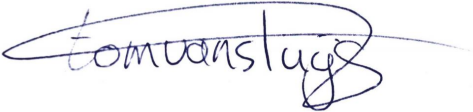
I have read the TU/e Code of Scientific Conduct¹.

I hereby declare that my Master's thesis has been carried out in accordance with the rules of the TU/e Code of Scientific Conduct

Date 07-04-2021
.....

Name Thomas Benjamin van Sluijs
.....

ID-number 1017606
.....

Signature

.....

Submit the signed declaration to the student administration of your department.

¹ See: <https://www.tue.nl/en/our-university/about-the-university/organization/integrity/scientific-integrity/>

The Netherlands Code of Conduct for Scientific Integrity, endorsed by 6 umbrella organizations, including the VSNU, can be found here also. More information about scientific integrity is published on the websites of TU/e and VSNU